SAPIENZA
UNIVERSITÀ DI ROMA

ENGINEERING FACULTY

Final Thesis in Mechanical Engineering

Measurements of forces on motorcycle sport model on wind tunnel

Supervisor:
Giovanni Paolo Romano

Graduand:
Jaime Nasarre

Co-Supervisor:
Antonio Lecuona Neumann

Academic Year 2008 – 2009

Resumen

- **Objetivo del proyecto**

Obtención experimental en el túnel de viento de la universidad La Sapienza de Roma de las fuerzas y momentos aerodinámicos:

Resistencia
Sustentación
Fuerza lateral
Momento de guiñada
Momento de cabecero
Momento de vuelco

- **Objeto de estudio**

La experimentación se ha llevado a cabo sobre un modelo a escala 1:10 de la motocicleta deportiva Yamaha M1.

- **Procedimiento**

Las fuerzas son registradas a través de una balanza dinamométrica. Ésta a su vez, envía los datos registrados a un ordenador a través del sistema de adquisición y son tratados por un programa realizado en LabVIEW 7.1 que directamente muestra los resultados de fuerzas y momentos.

Una parte muy importante del proyecto es pues, la calibración de dicha balanza dinamométrica, que en el momento del estudio, se hallaba estropeada una célula de carga, teniendo que realizar dos campañas de medidas diferentes para la obtención de las fuerzas y momentos aerodinámicos.

Además, se ha detectado un mal comportamiento de la balanza debido al excesivo rozamiento entre el fondo de la balanza y el plato móvil por lo que se ha prestado gran atención a minimizar la fricción utilizando unas pequeñas esferas metálicas.

- **Conclusiones**

Debido a la complejidad del montaje, los resultados experimentales no se ajustan perfectamente a los esperados. Además, se ha observado que la fijación y el plato móvil de la balanza, al no ser diseñados específicamente para la moto, no es tan rígida como debería ser.

Introducción.

El siguiente trabajo presenta un análisis del comportamiento de un modelo a escala 1:10 de una motocicleta deportiva, en concreto, la Yamaha M1.

El estudio se ha llevado a cabo en las instalaciones del departamento de mecánica y aeronáutica de la universidad La Sapienza de Roma, en el cual se haya el túnel de viento donde se han realizado las medidas.

Las fuerzas y momentos aerodinámicos que han sido estudiadas en el túnel de viento son:

- Resistencia
- Fuerza lateral
- Sustentación
- Momento de guiñada
- Momento de cabeceo
- Momento de rodadura o vuelco

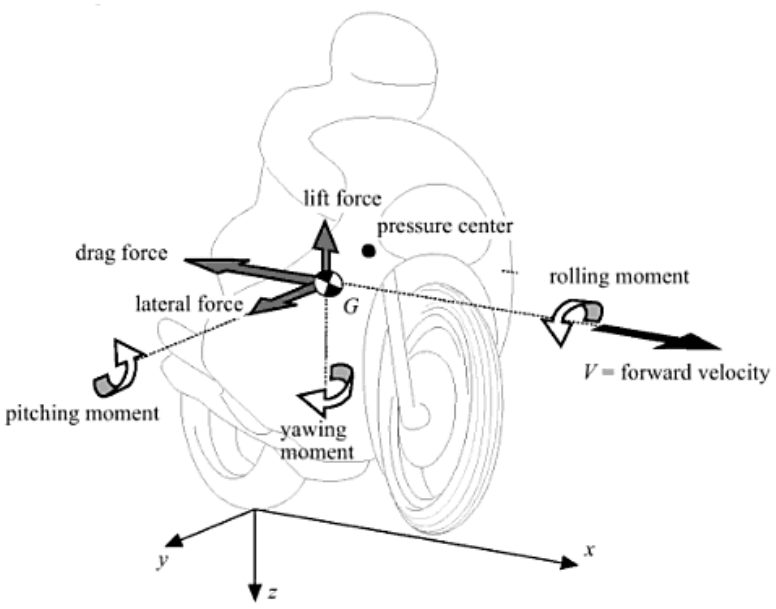

Figura 1. Fuerzas y momentos aerodinámicos en una motocicleta

El primer paso fue la calibración de la balanza dinamométrica con la que se midieron las fuerzas sobre el modelo a escala. Una vez calibrada la balanza, se ha procedido a la

experimentación en el túnel de viento teniendo en cuenta diferentes velocidades de viento entre 0 y 30 m/s a diferentes ángulos de guiñada entre -30º y +30º a intervalos de 10º. También se ha tratado de evaluar el efecto suelo utilizando una cinta móvil que simula el movimiento sobre la carretera. Finalmente sólo se pudo realizar un experimento pues el motor del sistema se sobrecalentaba.

Posteriormente se procede al análisis de los resultados y conclusiones.

Descripción de las diferentes partes del experimento.

Modelo a escala.

Como se ha dicho anteriormente, para la experimentación en el túnel de viento se utilizó un modelo a escala 1:10 de una motocicleta deportiva de la Yamaha M1.

Es importante tener en cuenta que las ruedas del modelo no pueden moverse durante los experimentos pues la fijación impedía dicho movimiento tal y como puede observarse en la figura 2.

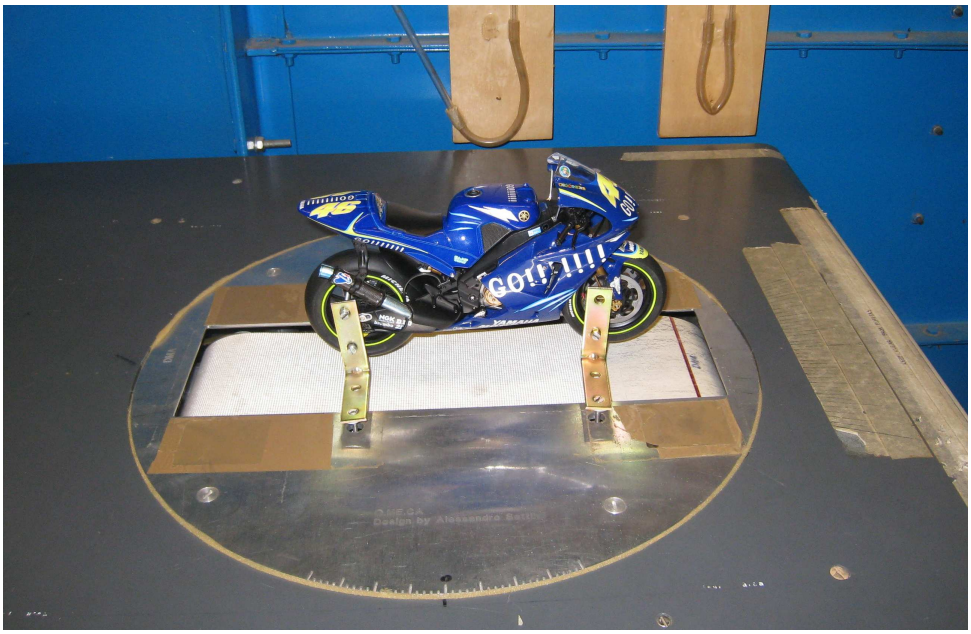

Figura 2. Fijación del modelo

Balanza dinamométrica

Para poder medir las fuerzas que el viento ejerce sobre el modelo a escala, éste se ha fijado a una balanza dinamométrica con 8 células de carga, capaz de medir las seis componentes de la fuerza, las tres fuerzas y los tres momentos mencionados anteriormente.

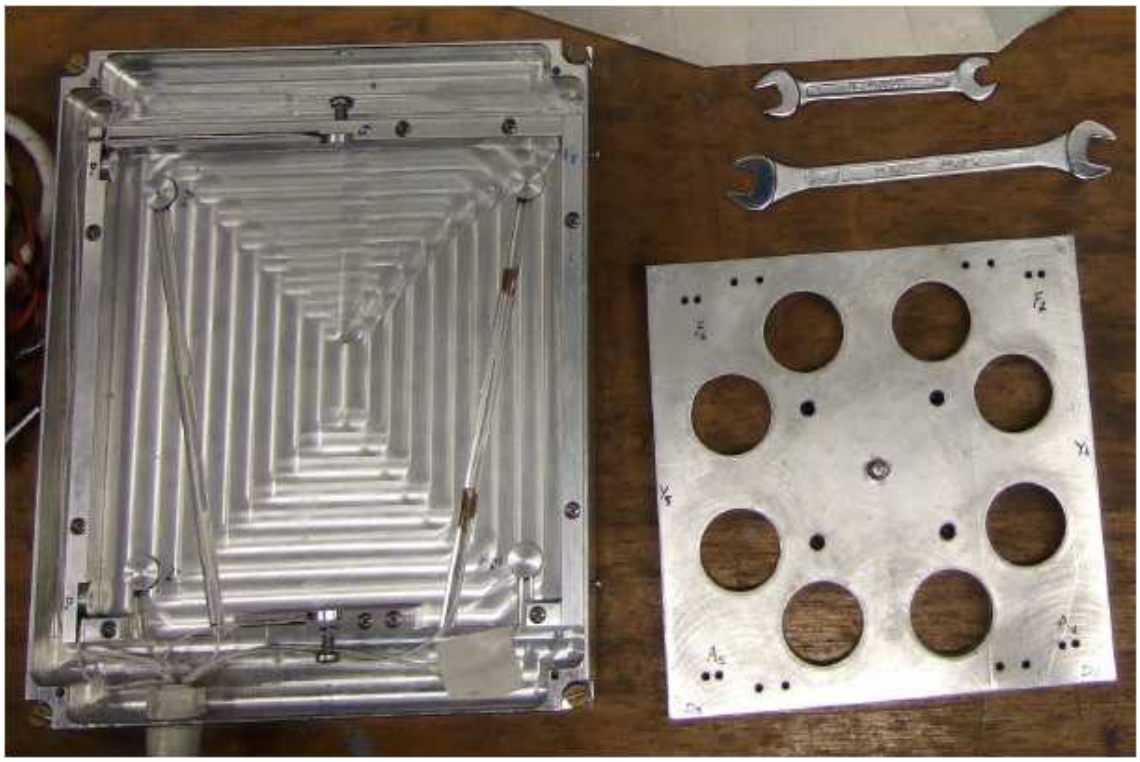

Figura 3. Balanza dinamométrica

Las ocho células están situadas de modo que en la base de la balanza hay cuatro células llamadas Fs, Fd, As y Ad. Cada una de ellas tiene un fondo de escala de 100 N. Con ellas se puede calcular tanto la sustentación como el momento de cabeceo y el momento de vuelco según el eje longitudinal de la moto. Estas células pueden ser precargadas con un tornillo que, enroscando o desenroscando, se ejerce una mayor o menor presión entre la célula y el plato móvil, es decir, se aplica una mayor o menor precarga.

Además, la balanza tiene otras cuatro células en el perímetro del plato móvil que son Ys, Yd, Ds y Dd. En este caso, las células tienen un fondo de escala de 50 N y se utilizan para el cálculo de la fuerza lateral, resistencia y momento de guiñada. Del mismo modo que en el caso de las otras cuatro células, éstas también tienen sus correspondientes tornillos para efectuar la precarga.

Figura 4. Tornillos para precargar las células

El primer paso antes de realizar las medidas, fue la calibración de la balanza dinamométrica. Para ello fue utilizado un programa realizado en LabVIEW 7.1 y unas constantes de calibración obtenidas anteriormente por el alumno Marco Nunez en su proyecto fin de carrera.

Calibración de la balanza dinamométrica.

El primer paso previo a la calibración propiamente dicha, es la nivelación de la balanza, pues al ser un aparato extremadamente sensible, las diferencias de altura de una célula respecto a otra se traduce en una carga mayor en la célula que está más elevada. Como se puede observar en la figura 4 en cada esquina de la balanza hay un tornillo como apoyo, y esto ayuda la correcta nivelación por la posibilidad de elevar o bajar cada esquina de la balanza enroscando o desenroscando el tornillo.

Además, para disminuir la fricción entre el plato móvil y el fondo de la balanza, se elevó 1,3 mm cada célula de carga, pues de este modo, se reduce la zona de contacto al área de contacto entre el plato móvil y las cuatro células. A pesar de ello, se siguió observando un elevado rozamiento entre el plato móvil y el fondo de la balanza.

CELULA	CONSTANTE DE CONVERSIÓN (N/V)
Fs	-10,37
Fd	-12,81
As	-10,68
Ad	-10,32
Ds	-5,232
Dd	-5,256
Ys	-5,672
Yd	-15,83

Tabla 1. Constantes de conversión.

Para proceder a la calibración de la balanza se han utilizado pesas de 0 a 3 kg para las células del fondo del plato y de 0 a 2 kg para las del perímetro. Se va aumentando la carga a incrementos de 0,5 kg y teniéndose que cumplir que la suma de las cargas en las cuatro células sea la carga puesta sobre el plato móvil y que haya un reparto entre las células lo mas distribuido posible. Esto es porque el cálculo de los momentos se hace a partir de las diferencias de las fuerzas registradas en cada célula. Por lo tanto, si por ejemplo las células delanteras tienen una carga residual mayor que las células traseras del fondo del plato debido a un mal reparto de cargas, existirá un error en el cálculo del momento de cabeceo pues se le estaría sumando un momento constante que no debería existir.

En la figura 5 se observa como se trató de conseguir estas dos condiciones pero dada la extrema sensibilidad de la balanza, es muy difícil de conseguir de forma exacta.

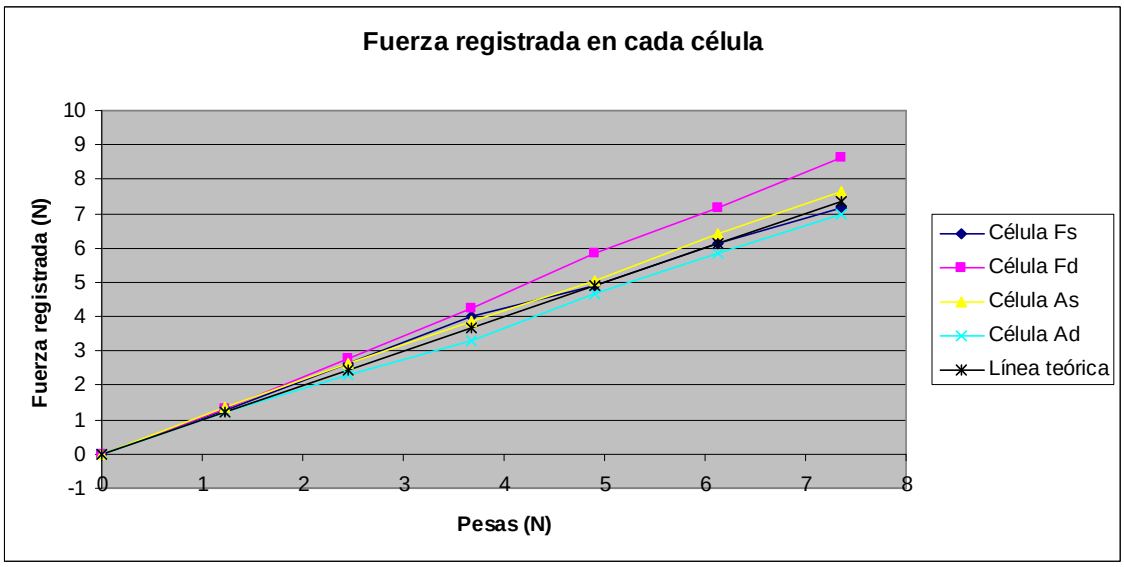

Figura 5. Evolución de cada célula respecto a la carga añadida

Se puede observar cómo la célula Fd mide ligeramente más de lo que debería ser teóricamente, pero el resto son bastante similares a la línea teórica que deberían seguir las células. Además, en la figura 6 se puede observar cómo la sustentación, es decir, la suma de las cargas de las cuatro células es muy similar a la teórica.

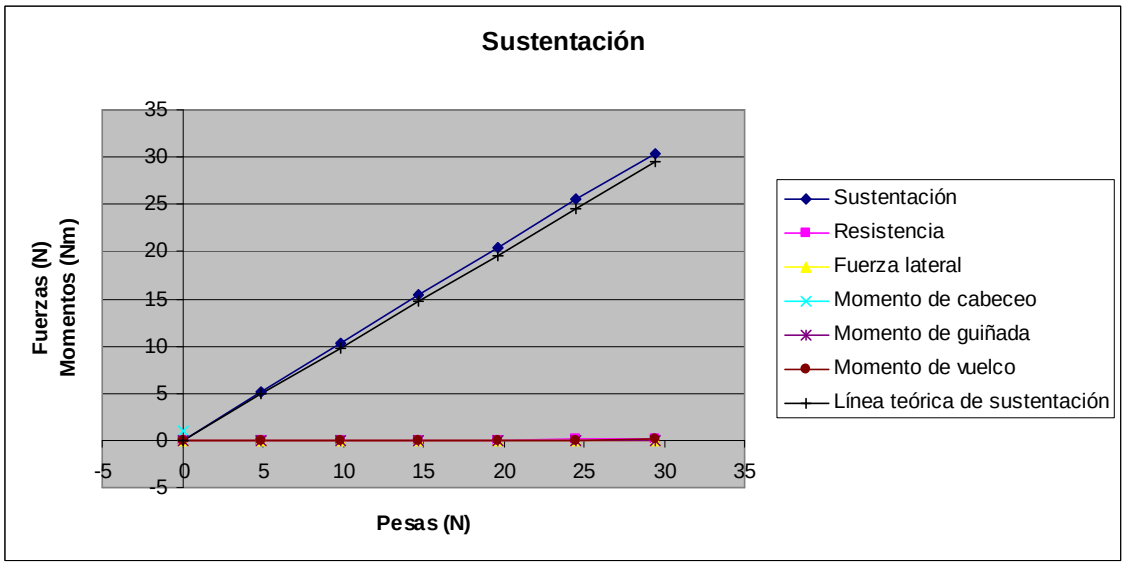

Figura 6. Evolución de las fuerzas y momentos con la carga añadida

Además, teniendo en cuenta que el rango de medidas en el que se moverán las medidas experimentales es menor de 5 N, se puede observar como las medidas son muy similares a las que deberían salir en la realidad.

Para realizar la calibración de las células laterales del perímetro, lo primero que hay que hacer es diseñar un sistema que convierta la fuerza vertical de la gravedad en fuerza horizontal que pueda medir las células. Esto se consigue con una polea, de modo que la pesa pueda colgar y arrastrar al plato hasta las células, tal y como se observa en la figura 7.

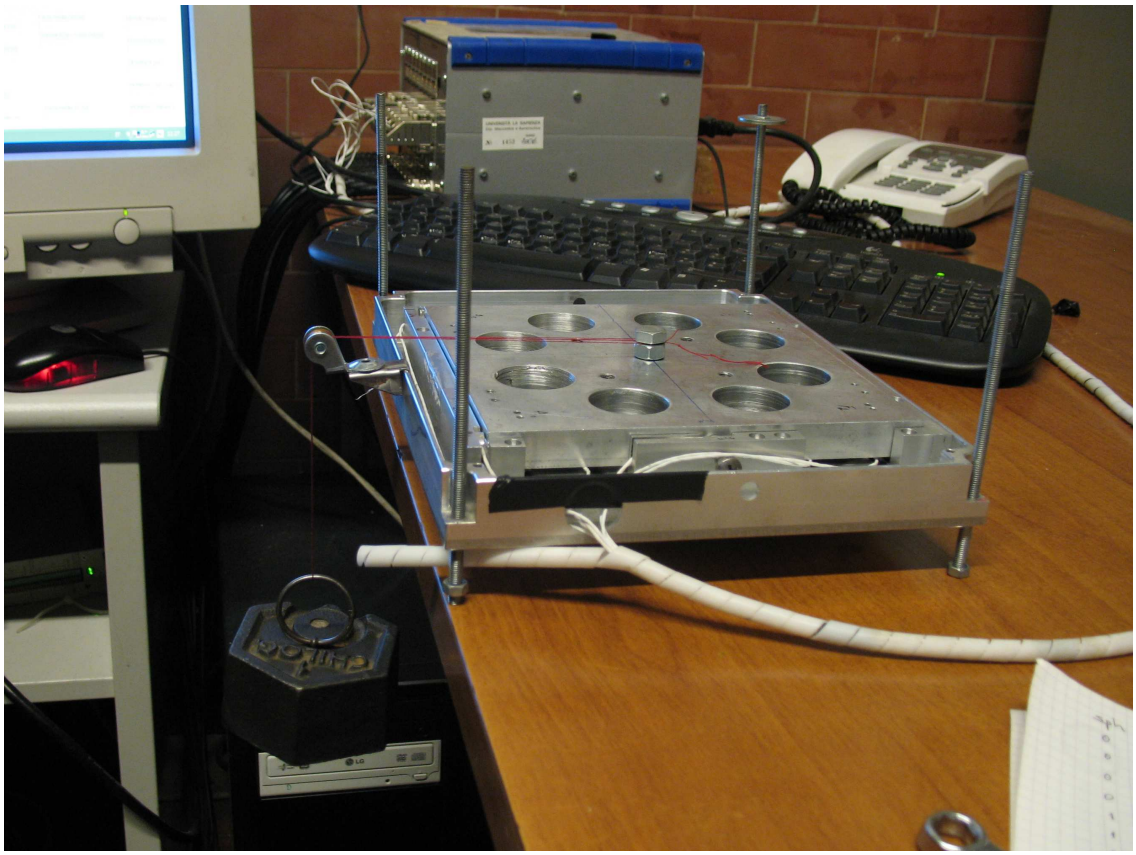

Fig. 7. Polea para calibrar las células del perímetro de la balanza.

Al llegar a este punto surgió un problema durante el proceso de calibración, ya que se observó que las células median menos de lo que deberían medir según las pesas que colgaban de la polea. Al hacer un análisis del problema se llegó a la conclusión de que se debía, en gran medida al rozamiento existente entre el plato móvil y las células del fondo de la balanza, tal y como refleja la figura 8. Esto es, la resistencia registrada era $F - \mu Q$, y no F.

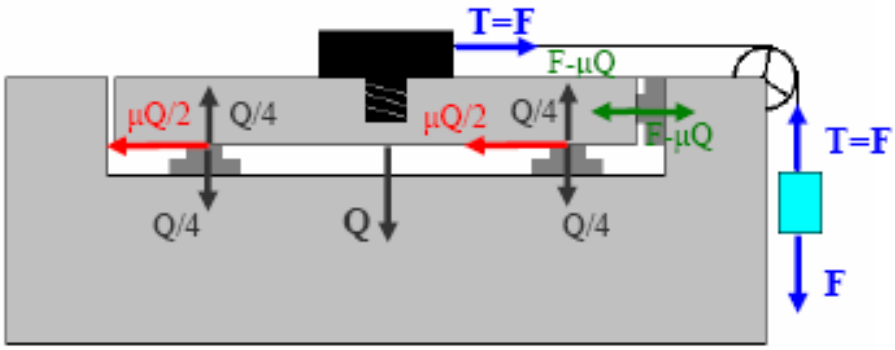

Figura 8. Esquema de fuerzas en la balanza con la polea

Por tanto, la solución que se adoptó fue colocar unas pequeñas bolas o esferas de acero inoxidable entre el plato móvil y el fondo de la balanza para minimizar el rozamiento, ya que el coeficiente de rozamiento de rodadura puede llegar a ser 1/10 veces el coeficiente de rozamiento por deslizamiento.

La aplicación de esta solución al rozamiento supone que cuando las pequeñas bolas están colocadas, el plato móvil de la balanza apoya sobre éstas y por tanto las células del fondo, As, Ad, Fs y Fd no están en contacto con el plato y entonces no medirán nada durante los experimentos. Por tanto, la colocación de las bolas supone que hay que realizar dos campañas de experimentos:

1. Sin esferas y por tanto se tendrá en cuenta las medidas de las células As, Ad, Fs y Fd, pues las otras células arrastrarán en sus medidas un error por el efecto del rozamiento.
2. Con esferas en la que se tendrán en cuenta las medidas de las células Ds, Dd, Ys e Yd.

Además, otro problema que surgió durante el proyecto fué que la célula lateral Ys se hallaba estropeada y por tanto no se podía medir esa componente de fuerza lateral. La solución adoptada, una vez se pensó en la colocación de las esferas, fue intercambiar las células Fd con Ys. De este modo, como durante la campaña de medidas con las esferas puestas, las células del fondo no miden, el intercambio se puede realizar sin afectar a la otra campaña de medidas.

Los resultados finales de la calibración de las células del perímetro con las esferas entre el plato móvil y el fondo de la balanza son:

- Resistencia: células Ds y Dd

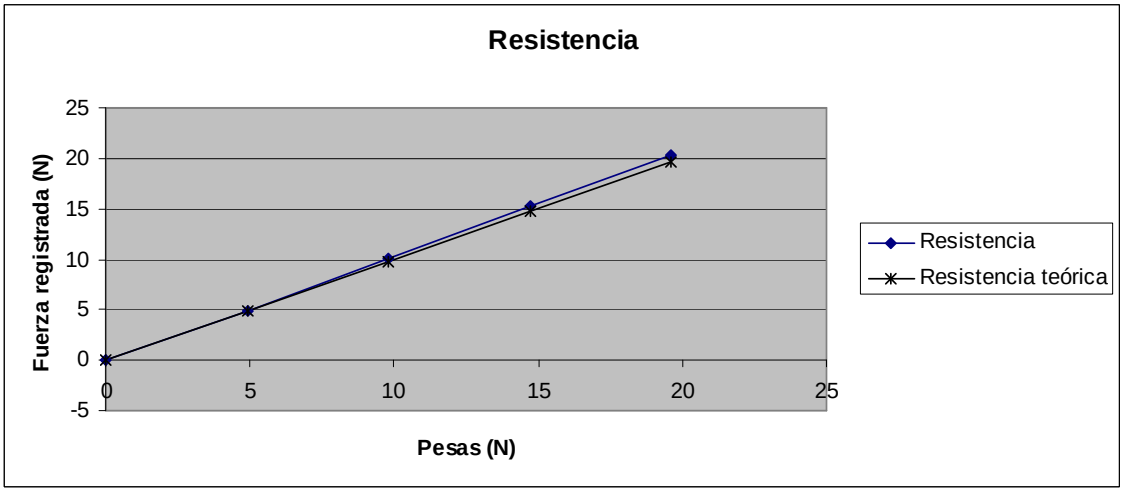

Figura 9. Evolución de la resistencia con la carga añadida a la polea

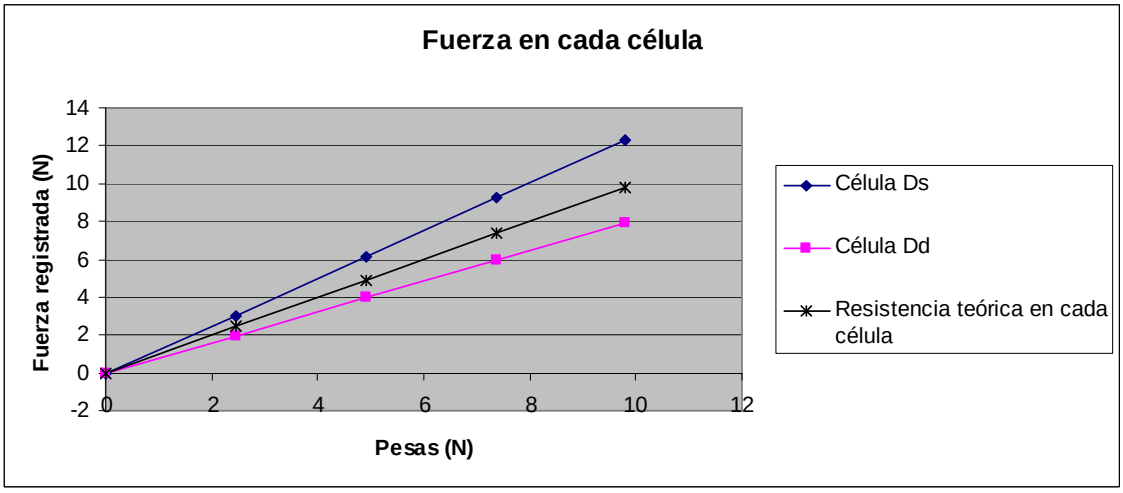

Figura 10. Distribución de la resistencia en las dos células Ds y Dd

- Fuerza lateral: células Ys e Yd

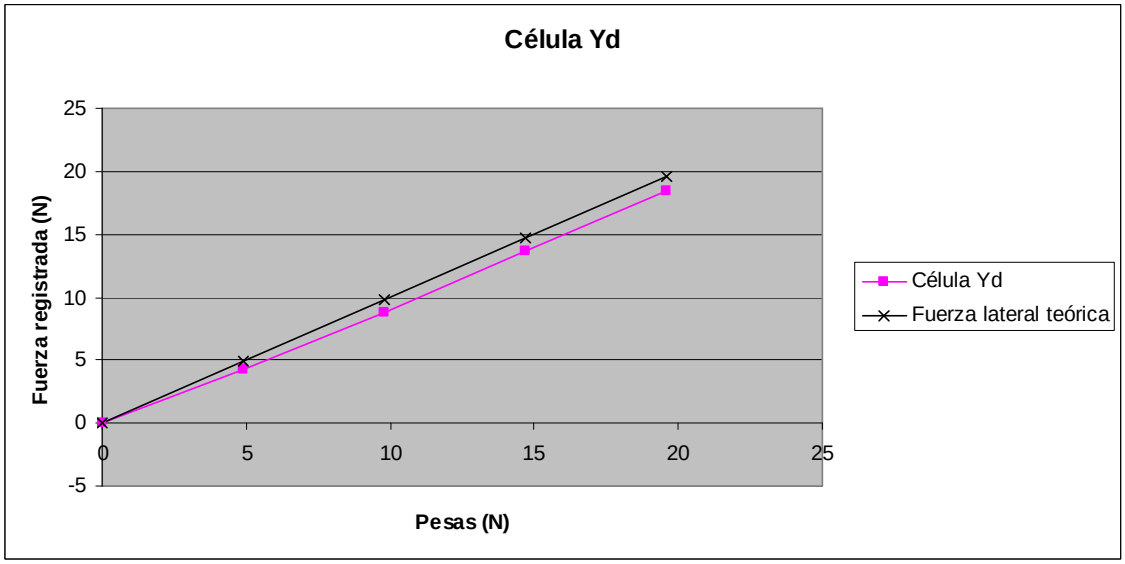

Figura 11. Evolución de la célula Yd con la carga añadida

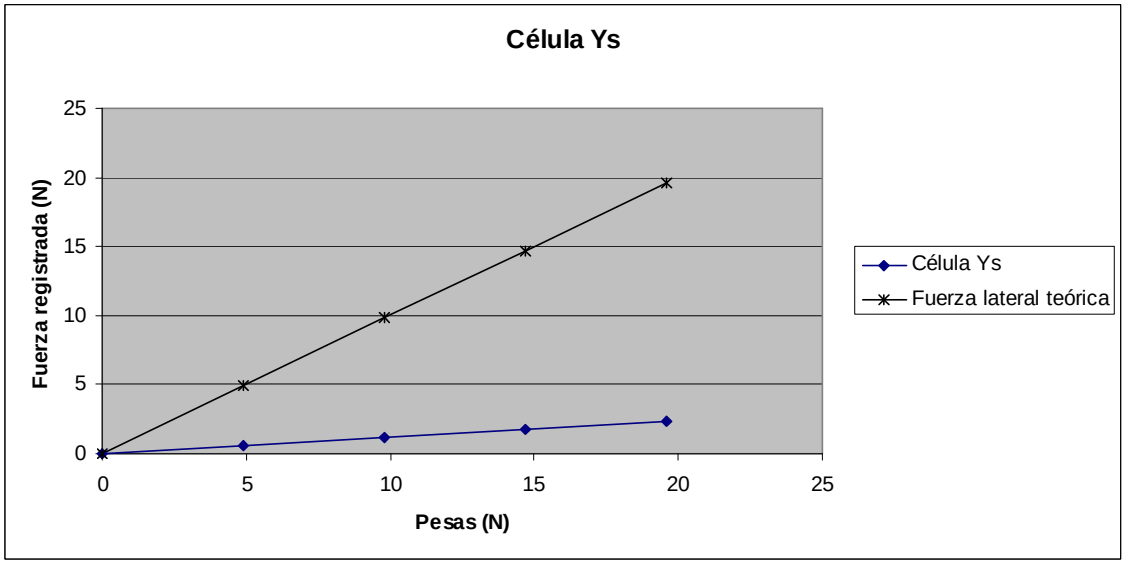

Figura 12. Evolución de la célula Ys con la carga añadida

Se puede observar que en la figura 12 se ha registrado la evolución de la fuerza medida con las pesas puestas sobre la polea, que la célula Ys mide mucho menos de lo que debiera. Esto es debido a que esta gráfica se tomó después de la campaña de medida en el túnel de viento pues no estaba disponible para realizar el estudio. Tal y como se ha explicado antes, ésta célula fue intercambiada por otra en el transcurso de la campaña de medidas en el túnel, y es por esto por lo que mide tan diferente a lo que se esperaba.

Resultados experimentales

En cuanto a los resultados experimentales, se han realizado para diferentes ángulos de guiñada de -30º a +30º a intervalos de 10º. Un caso muy especial se produce a 0º que es en el que toman medidas experimentales en casos de escala a tamaño real y con los que se podrán comparar los coeficientes aerodinámicos adimensionales C_D.

Las medidas serán realizadas desde los 0 m/s con el aire en reposo, hasta aproximadamente 30 m/s a intervalos regulares. Así se podrá observar la evolución de las fuerzas en cada célula para ver si dicha evolución es progresiva o se obtienen datos atípicos. Después, a partir de los datos experimentales se obtendrán los coeficientes adimensionales calculados a través de las siguientes fórmulas para cada ángulo de guiñada y así podremos observar si se tiene simetría. En el caso de la fuerza lateral, esta simetría no se obtendrá debido a que la célula Ys mide mucho menos de lo que debiera.

Fórmulas para los coeficientes adimensionales:

$$C_L = \frac{-L}{\frac{1}{2}\rho U^2 S_{pl}} \qquad C_D = \frac{D}{\frac{1}{2}\rho U^2 S_{fr}} \qquad C_Y = \frac{Y}{\frac{1}{2}\rho U^2 S_{lat}}$$

$$C_{mCabeceo} = \frac{M_{cabeceo}}{\frac{1}{2}\rho U^2 S_{pl} l} \qquad C_{mGuiñada} = \frac{M_{Guiñada}}{\frac{1}{2}\rho U^2 S_{fr} b} \qquad C_{mVuelco} = \frac{M_{Vuelco}}{\frac{1}{2}\rho U^2 S_{lat} b}$$

Donde:

- L: *lift* o sustentación
- D: *drag* o Resistencia
- Y: Fuerza lateral
- ρ: densidad del aire (1.167 kg/m^3 a presión atmosférica 987 bar y una temperature de 20ºC)
- S_{pl}: Superficie en planta de la motocicleta a escala
- S_{fr}: Superficie frontal de la motocicleta

- S_{lat}: Superficie lateral de la motocicleta.
- U: Velocidad del viento en los diferentes experimentos.

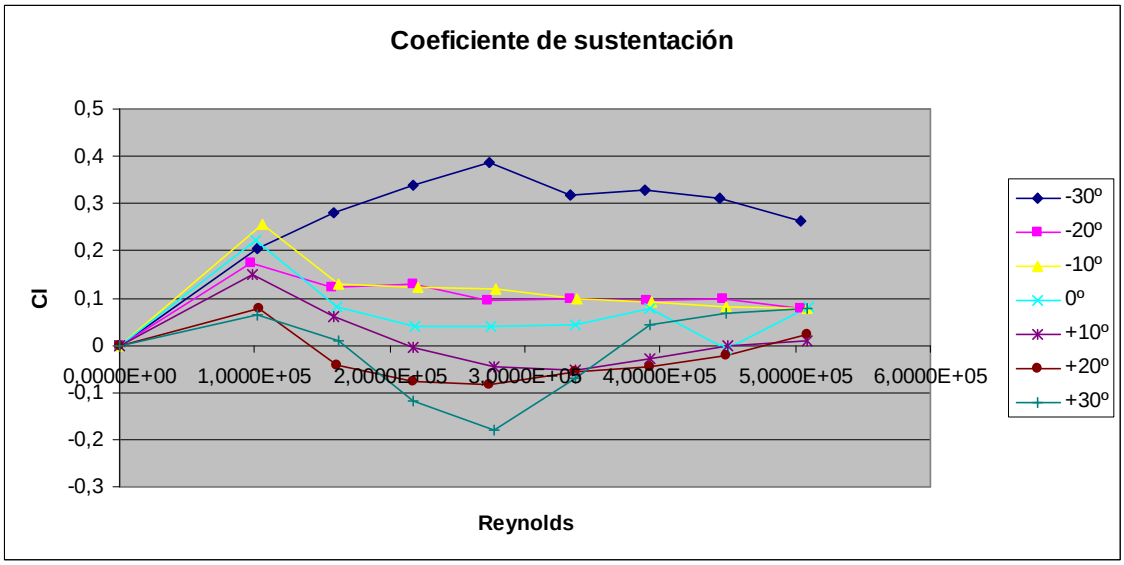

Figura 13. Evolución del coeficiente de sustentación con el número de Reynolds a diferentes ángulos de guiñada

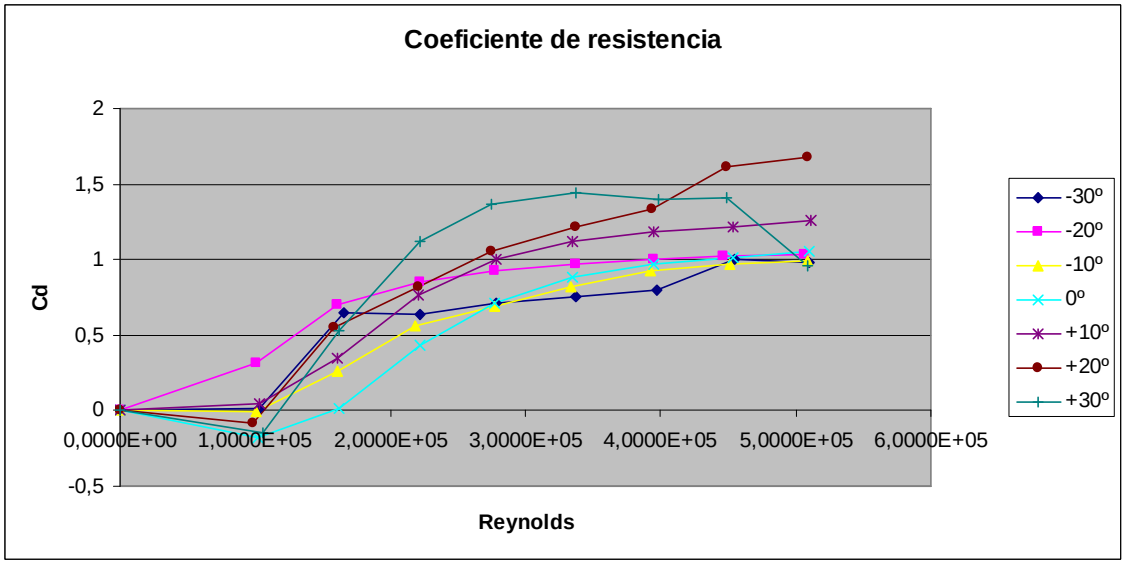

Figura 14. Evolución del coeficiente de resistencia con el número de Reynolds a diferentes ángulos de guiñada

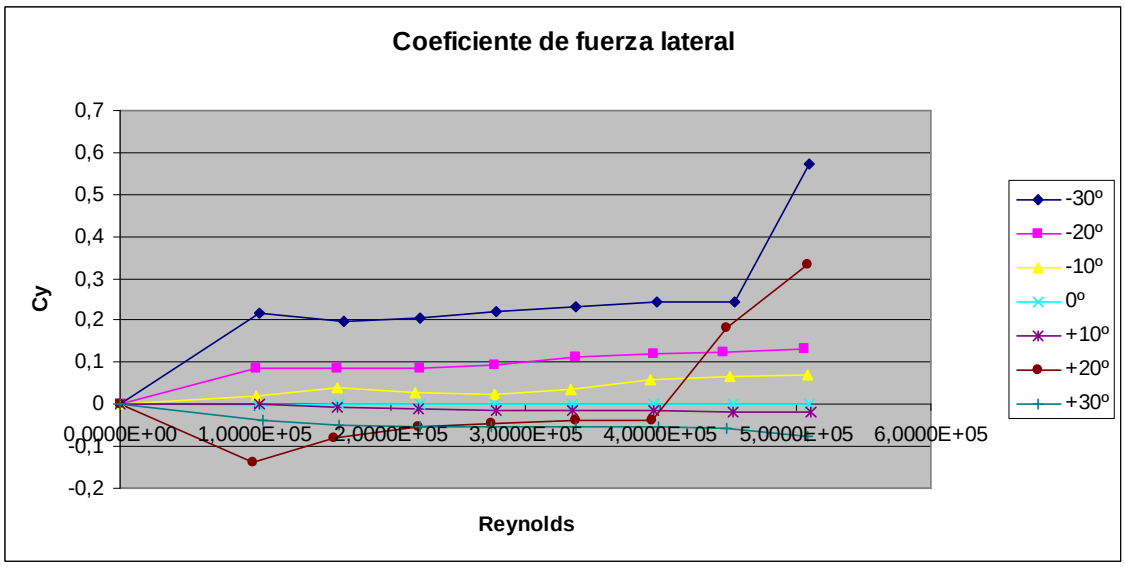

Figura 15. Evolución del coeficiente de fuerza lateral con el número de Reynolds a diferentes ángulos de guiñada

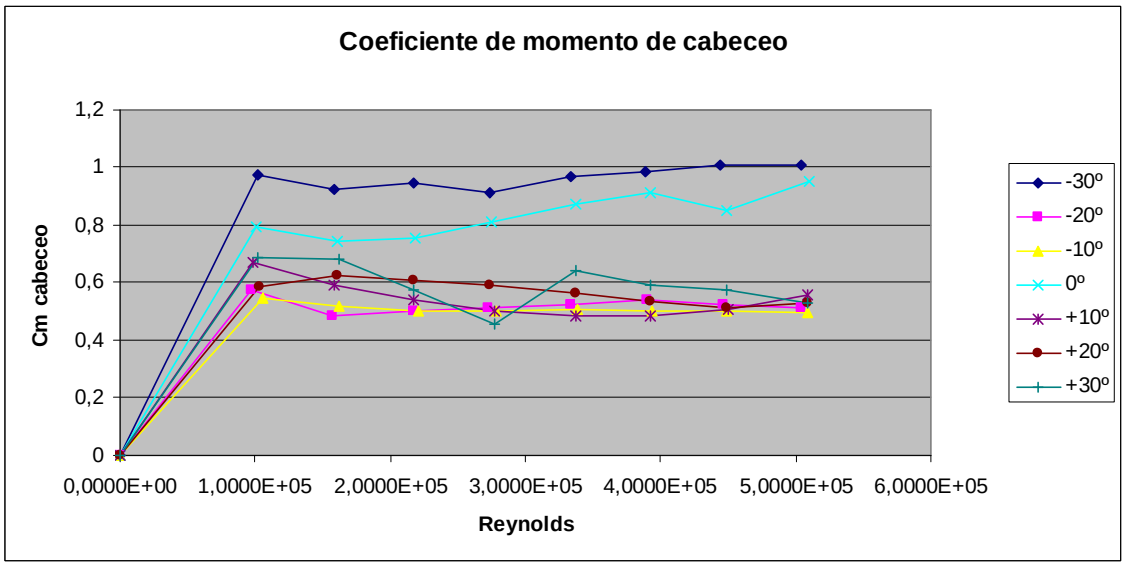

Figura 16. Evolución del coeficiente de momento de cabeceo con el número de Reynolds a diferentes ángulos de guiñada

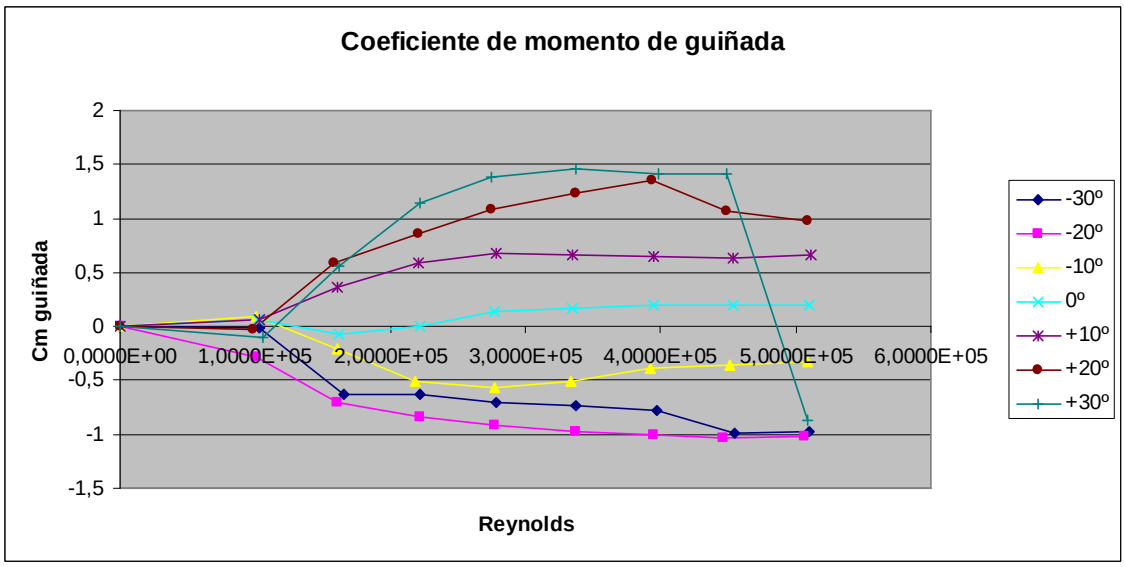

Figura 17. Evolución del coeficiente de momento de guiñada con el número de Reynolds a diferentes ángulos de guiñada

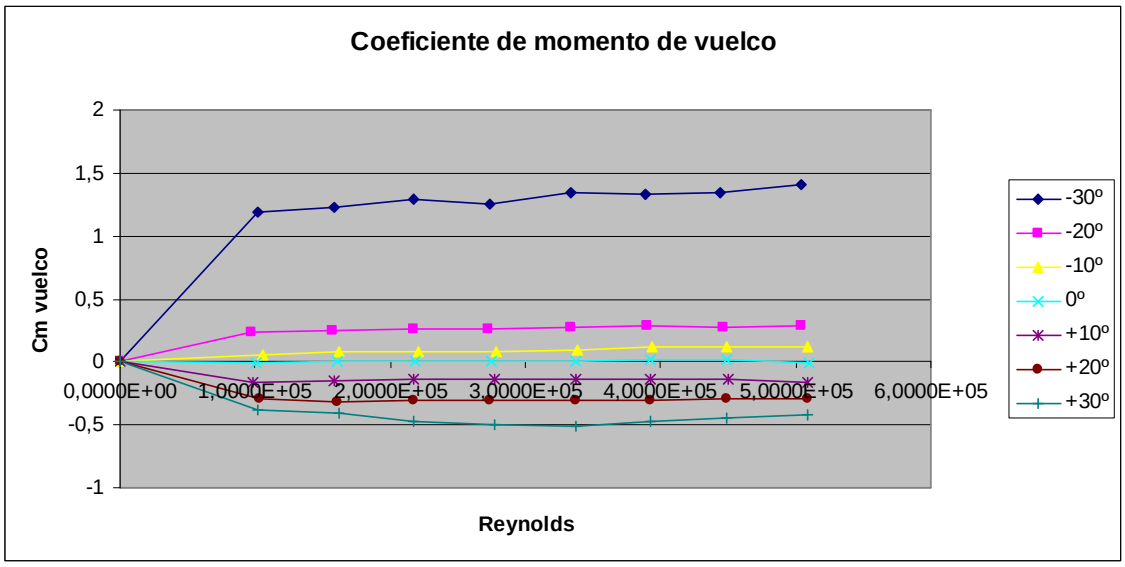

Figura 18. Evolución del coeficiente de momento de vuelco con el número de Reynolds a diferentes ángulos de guiñada.

Como se puede observar en las diferentes gráficas, la simetría que debería existir en las medidas como consecuencia de la simetría de la motocicleta en estudio, no existe de modo estricto. Existe una tendencia hacia la simetría, pero no se observa en las medidas en valor

absoluto. Es decir, el coeficiente adimensional de resistencia a un ángulo de guiñada de -30º debería ser el mismo en valor absoluto al que se obtendría a +30º y sin embargo son claramente diferentes. Pero si que se observa que a medida que va aumentando el ángulo de guiñada, la resistencia va aumentando como fruto de un aumento del área frontal a la dirección del viento.

Otro experimento que se intentó llevar a cabo fue la eliminación de la capa límite para intentar simular el "efecto suelo" existente entre la motocicleta y el suelo durante el movimiento rectilíneo. Este efecto se caracteriza por hacer como un efecto de succión del suelo hacia la moto, produciéndose una sobrecarga que provoca un aumento en la adherencia de los neumáticos.

Este experimento consistía en una cinta que se situaba entre la balanza y la motocicleta y que simulaba la carretera y por tanto el movimiento, haciendo mover esta cinta a través de un pequeño motor eléctrico. El problema es que cuando se querían hacer experimentos a una velocidad mayor a 10 m/s, el motor comenzaba a sobrecalentarse, y debido a ello no se han podido sacar conclusiones de este estudio.

Conclusiones

Las conclusiones que se han obtenido en este proyecto se han dividido en dos partes. Por un lado conclusiones durante el proceso de calibración de la balanza, y por otro lado conclusiones de los resultados de los experimentos en el túnel de viento.

Durante el proceso de calibración:

- La precarga en las células laterales Ds, Dd. Ys e Yd provoca un mal funcionamiento de estas células, que miden menos de lo que deberían.
- Para solucionar el problema de la fricción entre el plato móvil y el fondo de la balanza, se ha decidido introducir cuatro pequeñas esferas metálicas debajo del plato móvil.

- En las células que miden la resistencia, la célula Ds mide mas que la célula Dd. Esto provoca la ausencia de simetría en el momento de guiñada medido en el túnel de viento.
- La célula Ys estaba rota. La solución ha sido intercambiarla con la célula Fs durante los experimentos con las esferas. El intercambio fue hecho después de todo el proceso de calibración, y es por esto por lo que luego, cuando se ha obtenido la evolución de las medidas de la célula Ys se ha observado que se obtienen medidas mucho mas bajas de lo que se debería obtener. Ésta es la causa por la que no se obtiene la simetría en el coeficiente de fuerza lateral.

Durante los experimentos en el túnel de viento:

- Se ha demostrado que la fijación afecta a la medida del coeficiente de resistencia por el incremento de área frontal y porque provoca turbulencias en el paso de los huecos de la fijación.
- La resistencia aumenta con el cuadrado de la velocidad del viento tal y como se esperaba teóricamente.
- Todos los coeficientes adimensionales aumentan con el ángulo de guiñada.
- El sistema de simulación del efecto suelo no está bien diseñado para las velocidades de experimentación que se deseaban hacer. El motor se sobrecalentaba, por lo que debe cambiarse por uno que tenga una potencia mayor.

INDEX

Page

ABSTRACT

This thesis presents a study of the aerodynamical behaviour of a sportive motorcycle in a wind tunnel. This analysis has been performed in the wind tunnel of the Mechanics and Aeronautics department of La Sapienza University of Rome.

The first step has been the development of a reference overview in chapter 1 about the general features of wind tunnels and the typically measurements performed in the particular case of a motorcycle. Chapter 2 describes in great detail the present experimental set-up.

In order to carry out these measurements in the wind tunnel, a dynamometric balance has been used. A very important part on the development of this project is the calibration of this balance in order to get a high reliability on the results. This calibration process is explained in great detail in chapter 3. The main problem that has arisen with the calibration of the balance is the presence of friction, which can be solved using some small spheres in order to minimize this effect, as it is explained in chapter 3.

Finally, chapter 4 includes the measurements performed in the wind tunnel and the analysis and conclusions derived from the results. These measurements have been performed for different speeds of wind from 0 to 30 m/s to check the evolution of the values of the dimensionless aerodynamic coefficients. Moreover, to study the behaviour of the motorcycle on a curve or in the case of lateral wind, the measurements have been performed with different yawing angles from -30º to +30º every 10º. This study of positive and negative angles also allows checking if the results fit the theoretical symmetry of the model, although the final conclusion will be that this symmetry is not achieved exactly due to the complexity of the aerodynamical studies.

CHAPTER 1

REFERENCE OVERVIEW ON WIND TUNNEL MEASUREMENTS FOR MOTORCYCLE MODELS

1.1 REQUIREMENTS FOR THE WIND TUNNEL

In this chapter, the requirements for the wind tunnel will be explained, specifically for performance of measurements on motorcycle models or road vehicles.

The first classification of wind tunnels is in supersonic and subsonic wind tunnels. This classification is based on the Mach number. The Mach number is defined as:

$$Ma = v/c$$

where *v* is the speed of wind and *c* the speed of sound.

If the Mach number is 0,3 or lower, the wind tunnel will be subsonic, and incompressibility air conditions will be present. Otherwise, the wind tunnel will be supersonic.

In the case of motorcycle models, the experiments are developed in subsonic wind tunnels.

Another classification of the wind tunnels is done depending on the opening or closing of the air circuit. The first type is called “Eiffel” and the second one “Prandtl”. In Eiffel type, the air flows in a straight line and there is no air recirculation. In Prandtl type, the air flows around a closed circuit (re-circulating the air) and the test section can be opened or closed.

The interest on the aerodynamic area in sport models is increasing, and in this area, the wind tunnel is a particular important factor in the experiments. The main reason for this increasing focus on wind tunnels is the availability of breakthrough technologies that better simulate on-track conditions, providing new opportunities to enhance performance. There are two areas that are subject of strong current interest:

1. Test section configurations that eliminate wind tunnel interference effects to provide the highest possible aerodynamic simulation fidelity.
2. High speed rolling road systems with integrated force measurement systems that provide high fidelity simulation of ground effects. [1]

There is another area that automobile companies are studying for more discerning customers. This area is the acoustic provoked by the air inside of the vehicles.

In order to do all these studies mentioned before, wind tunnels should have some particular requirements.

The first condition to do the measurements on motorcycle models on wind tunnel is that this wind tunnel should have a floor to simulate the road. This floor can have different additional characteristics that will be explained in this chapter.

To measure all the forces and moments on the motorcycle model, a balance must be positioned under the floor. In the case of measurements on motorcycle models, the fixation of the motorcycle to the ground should be as hard as possible to avoid the movement of the motorcycle due to the air.

Fig 1.1.01 shows a very good example of these characteristics mentioned before. The fixation is neither disturbing the movement of the air nor adding more front area, thus any error is introduced in the measurements.

Fig. 1.1.01. Fixation of the motorcycle. [2]

Another important characteristic for the aerodynamic studio is the simulation of the movement of the motorcycle on the road, called, the ground effect. Fig. 1.1.02 shows different experiments to simulate the ground effect. But not all of them are used in wind tunnels because of the complexity of the set-up. In fact, the most typically developed set-up systems in wind tunnels are “f”, “c”, “a” and “b” configurations, being “f”, which is the moving belt system, the most used configuration because of the low complexity of the set-up and the reliability of the results.

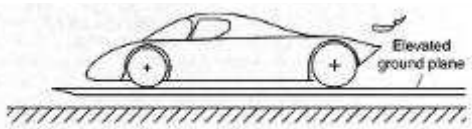

Fig. 1.1.02 a

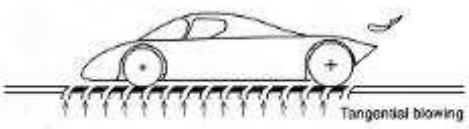

Fig. 1.1.02 d

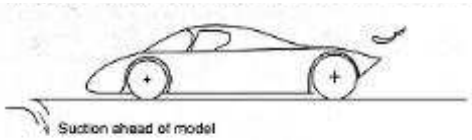

Fig 1.1.02 b

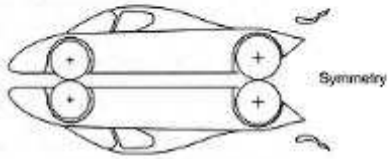

Fig 1.1.02 e

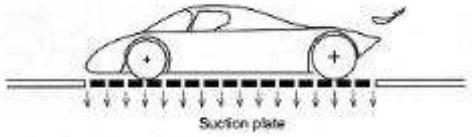

Fig 1.1.02 c

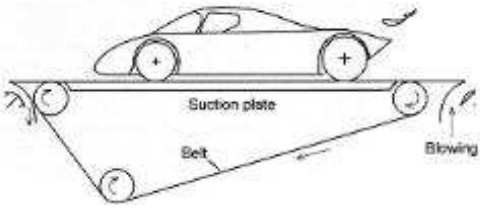

Fig 1.1.02 f

Fig. 1.1.02. Different kind of ground effect simulation. [3]

Figures 1.1.03 to 1.1.05 show different real experiments in which some of these most common configurations are used.

In the moving belt system, in order to simulate the ground effect, the belt should move at the same speed as the wind. The objective of this belt is to eliminate the boundary layer existing between the model and the floor simulating the ground effect. Thus, the experiment and the results will be more realistic.

Fig 1.1.03 shows the moving belt. It can be observed that there is a circle platform which can be turned. The objective of this platform is to change the angle of attack of the experiment to do the measurements of the lateral forces.

Fig. 1.1.03. Moving belt system. Example of “f” configuration. [4]

Pininfarina has a combination between “b” and “f” configurations, in its first large scale wind tunnel as shows Fig. 1.1.04. In 1995 it was replaced by a new system of ground effect simulation called the *T-Belt* [Fig. 1.2.09], which uses a combination of three belts. This system has been in operation since September 1st 2006 in the large scale *Automotive Wind Tunnel* of the Pininfarina Aerodynamic Center. In the next section “Existing facilities” this new platform of the Pininfarina wind tunnel will be seen. [5]

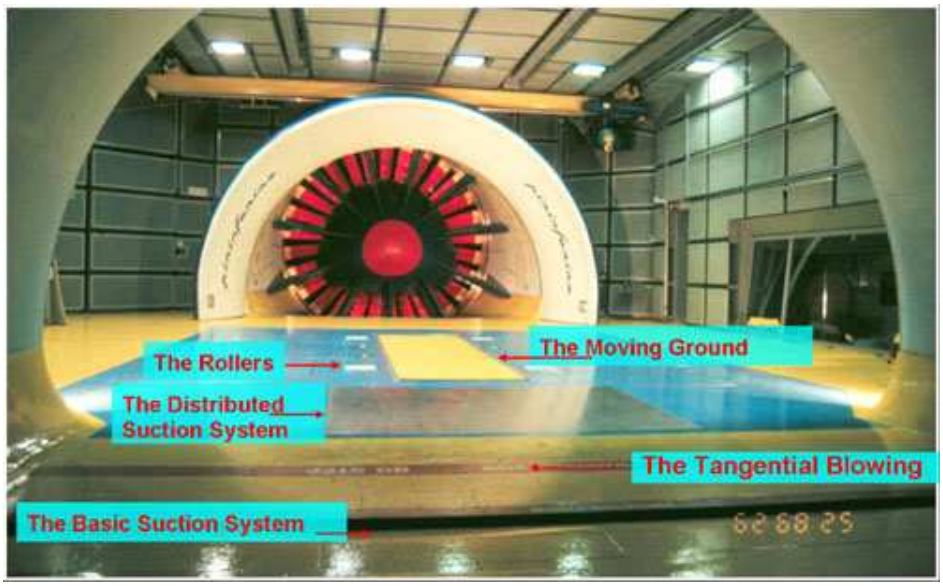

Fig. 1.1.04. First ground effect simulation on Pininfarina wind tunnel. [5]

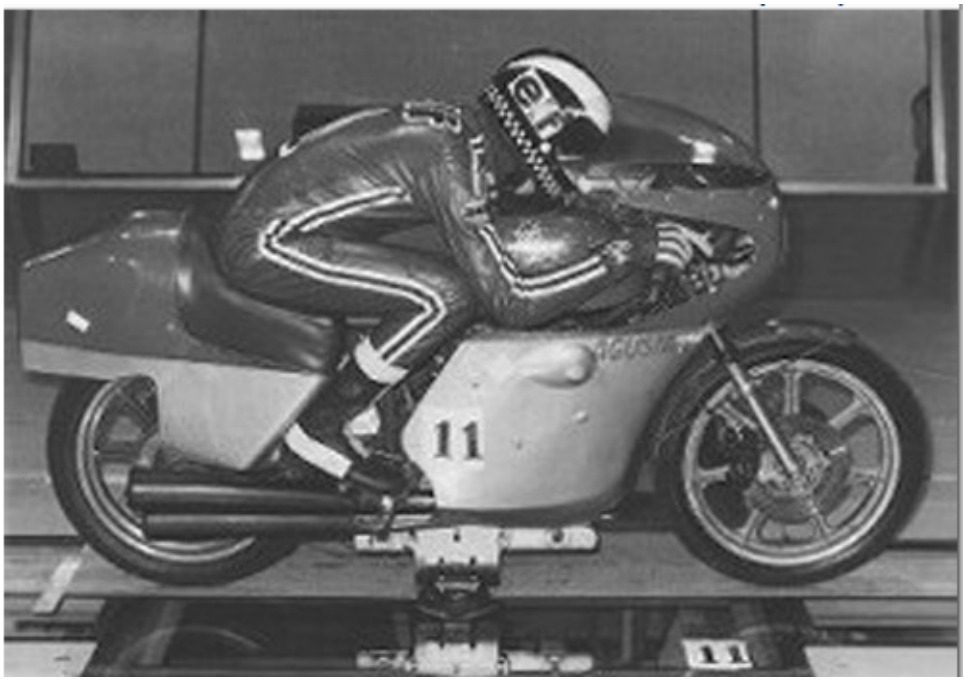

Fig. 1.1.05. Example of “a” configuration on motorcycle. [5]

In the case of closed test section, if the walls are rigid, errors can appear due to the pressure between the model and the walls. Therefore, an additional feature of the wind tunnels, in case of closed test sections, is that the walls may have some degree of elasticity in order to minimize this error.

Contoured wall technology (also called adaptive wind tunnel technology) is the most important recent innovation in the development of low speed wind tunnels and under the right circumstances, virtually eliminates model blockage errors.

Wall interferences are all parasitic effects, induced by the test section walls. The magnitude and kind of interference depends, for instance, on the model size in relation to the test section size (blockage) and the probable lift of the model. The most dominating effects accounting for wall interferences are:

- model blockage
- wake blockage
- boundary layer blockage
- interaction of wall and model boundary layers
- flow displacement by the wind tunnel walls [6]

A model placed in the tunnel presents an added blockage which has the effect of speeding up the flow slightly as the air passes through the gap between the model and the walls (Fig.1.1.06).

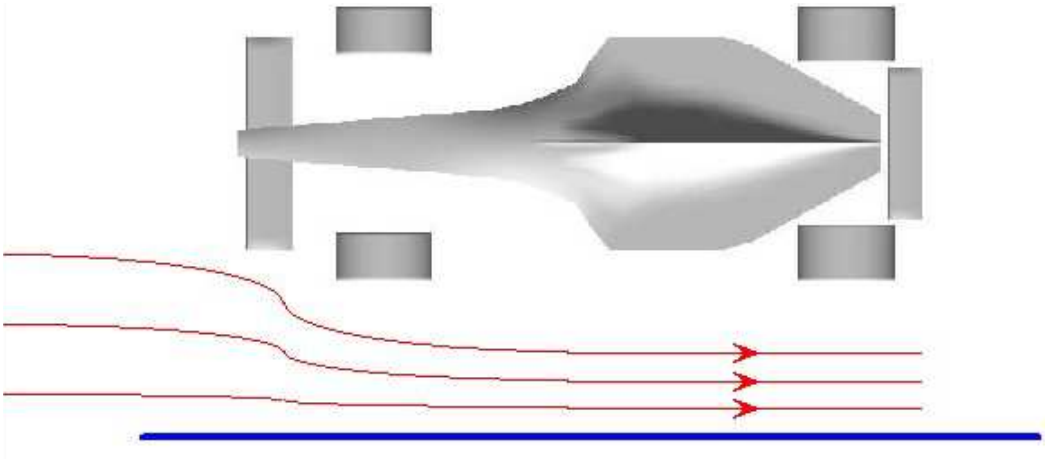

Fig. 1.1.06. Straight walls and air flow lines [7]

For instance, in the Honda wind tunnel the walls are not elastic, but the contoured walls are fixed and optimised for a 50% models. This contoured wall upgrade allows models of up to 50% to be tested with minimal blockage effect errors.

By changing the shape of the walls to follow the streamlines no artificial increase in air flow takes place around the model and the blockage of the model is effectively removed (Fig.1.1.07).

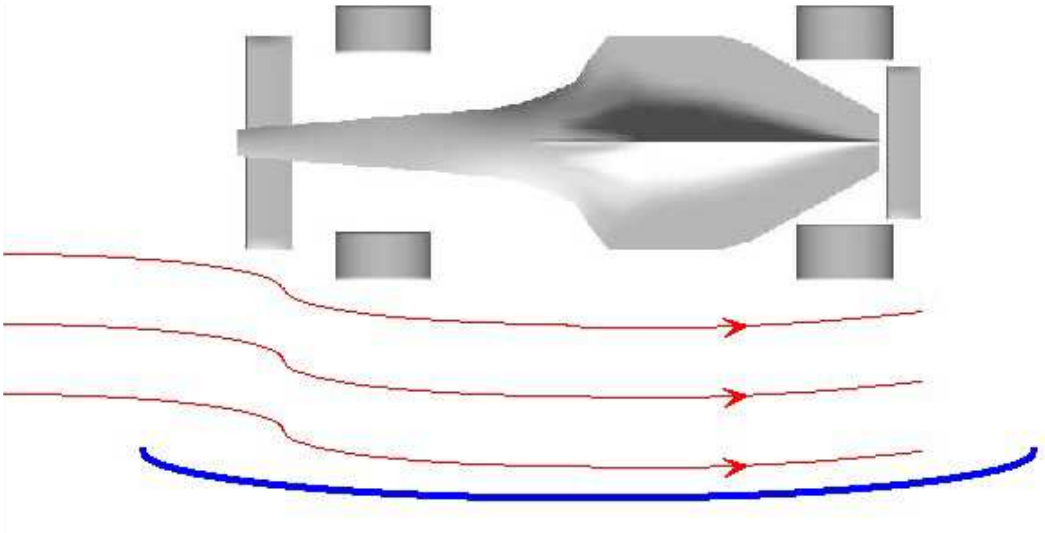

Fig. 1.1.07. Contoured walls and air flow lines. [7]

The Honda tunnel has a reputation for providing very high quality data. Both the software upgrade and the new contoured wall test section enhance this reputation, with the added benefit of allowing 50% Formula 1 and other racing series models to be tested without having to consider what the effect of blockage might be. [7]

Wind tunnels are mainly used for measurement of the aerodynamic performance of a car body. Although, in recent days, attention has been concentrated not only on aerodynamic performance, but also on the measurement of the aerodynamic noise that the car body generates.

In these wind tunnels, it is required to have higher aeroacoustic performance (to decrease noise generated by the wind tunnel itself) in addition to its conventional performance: maximum wind velocity, air stream uniformity, etc.

The characteristics of these kinds of wind tunnels are:

- Aeroacoustic performance: A low background noise level with high velocities. For example, in the Suzuki Motor Corp. wind tunnel, a background noise level of 50 dB(A) or less is achieved at a wind velocity of 100 km/h and in the Pininfarina wind tunnel 68 dB(A) are achieved at the same wind speed.
- Variable width nozzle: It can be varied depending on the vehicle to be tested. When the vehicle under testing is a two-wheeled motorcycle, the width can be reduced to enable testing at higher air velocities. [8]

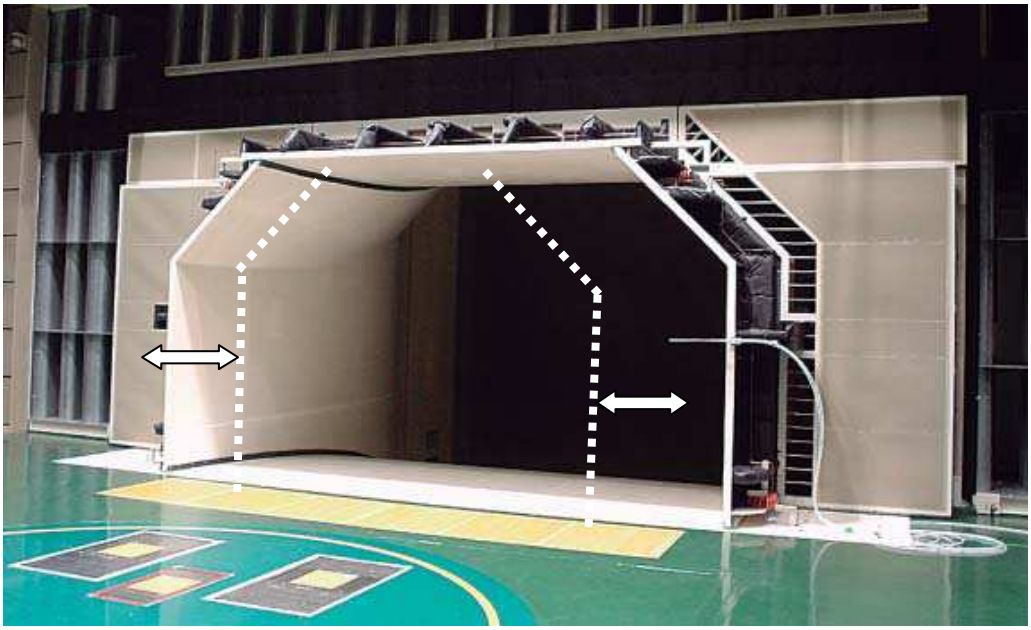

Fig. 1.1.08. The variable width nozzle [8]

In Pininfarina wind tunnel, the wind noise is measured inside and outside of the vehicle. To measure the noise in the inside, the acoustic dummies with microphones that are shown in Fig 1.1.09 are placed into the vehicle.

Fig. 1.1.09. Acoustic dummies for the acoustic study. [5]

In order to measure the noise provoked by the vehicle, there are two microphone arrays (see fig. 1.1.10), placed respectively on the ceiling and on the side wall of the test section. These two arrays localize the noise sources of the upper and lateral parts of the

vehicle. The signals acquired by the microphones are processed with an algorithm that is able to estimate a noise source located in a specific area of the space.

Fig. 1.1.10. Microphone arrays for the acoustic study. [5]

1.2 EXISTING FACILITIES

This section shows different types of wind tunnels used for the performance of experiments on motorcycles. Many of the characteristics mentioned in the previous section “Requirements for the wind tunnels” are present and discussed in the following examples of wind tunnels.

The first example of wind tunnel for motorcycle experiments is located at the National Research Council in Ottawa (Canada). This tunnel has been used to perform an experiment on the motorcycles Suzuki Hayabusa and Kawasaki ZX-12R in order to explain why the first one is faster than the second one. The conclusions derived from this study show that the mains difference between Hayabusa and Kawasaki is the aerodynamic form. This is why the aerodynamic studies on wind tunnels are so important.

The tunnel used was built in 1940 and the dimensions of its test section are 2,7 m. wide and 1,9 m. high, which provides comfortable room for a motorcycle. Wind is generated

with a four-blade fan driven by a 2000 horsepower DC motor, located two and one-half stories below the chamber, which circulates the air continuously in a vertical loop. The fan can generate a wind speed of 500 km/h. The effect of side winds is provided by rotating the motorcycle on a turntable to produce an approaching wind flow from one side or the other. The wheels are stationary, since wheel rotation effects have been found to be small. Each motorcycle was mounted on a balance, set below a turntable and flushed with the floor. The balance is an extremely sensitive measuring device linked to computers in the control room. [9]

Fig. 1.2.01. NRC wind tunnel test section. [10]

Moreover, NRC has developed a high-rate pressure scanning system that is a useful tool for automotive aeroacoustics. Simultaneous measurement of unsteady pressures at many locations on a vehicle's windows, coupled with a knowledge of the structural dynamics and sound transmissibility of the glass, will enable predictions of interior noise levels to be made, as well as identifying the source of unwanted or excessive wind noise.

Technical Specifications

Tunnel Geometry

- Contraction ratio: 9:1
- Test section: 1.9 m x 2.7 m x 5.2 m
- Test-section area:
    - Standard: 5.07 m^2
    - Groundboard: variable height

Tunnel Characteristics

- Fan power: 1490 kW
- Maximum speed: 140 m/s
- Speed uniformity: ± 0.7 %
- Turbulence level: 0.14 %
- Longitudinal static pressure gradient:
    - Standard: negligible
    - Groundboard: 0.0044/m

Auxiliary Systems

- Compressed air: up to 2,000 kPa
    - Dew point (- 40°C): 2.7 kg/s
    - Undried: 5.0 kg/s
- Model supports
    - 3-D steady-state: 3-point and single strut supports
    - 3-D unsteady: sting
    - 2-D steady state: upper air bearing
- Flow traverse rigs: several, automated
- Auxiliary power: 156 kVA, variable frequency
- Acoustic liner: anechoic above 400 Hz

Main Balance

- Measurement accuracy: ± 0.1% to ± 0.05% full scale
- Maximum model weight: 450 kg.
- Lift: ± 6.7 kN
- Drag: ± 2.3 kN
- Side force: ± 4.4 kN
- Pitch: ± 2.7 kN-m
- Yaw: ± 2.7 kN-m
- Roll: ± 2.7 kN-m

Data System and Instrumentation

- A/D channels: 24 & 15 bit @ 100 kHz, custom configurations
- Redundant tunnel condition sensors

- Software: test-specific MatLab code, Labview
- Model/probe control: 16-axes, Aerotech
- Pressure measurements: Scanivalve ZOC™Kulite
- Anemometry: hot-film/hot-wire
- Balances: internal (TASK, NRC, various) and external (cruciform, various)
- Flow visualization: PIV, Acoustic Array, PSP laser light sheet, smoke, surface oil film, fluorescent mini-tuft [10]

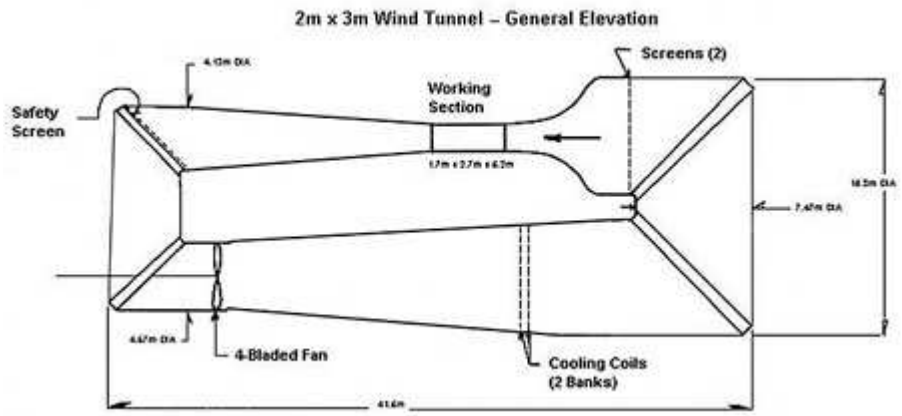

Fig. 1.2.02. NRC 2 x 3 m. wind tunnel. [10]

The Pinifarina wind tunnel is mainly used for testing four wheeled vehicles, although there is also some experiments on motorcycles. The most important evolution on this wind tunnel is that the old belt system has been changed by a new belt system with T shape which is bigger and provides a higher speed. The new system substantially improves the simulation of the ground effect. This new belt system is shown in fig. 1.1.09.

Fig. 1.2.03. The new moving belt system on Pininfarina wind tunnel. [5]

The main characteristics of the new system are:

The overall width of the upstream end of the moving ground has been increased from 1.0 m to 2.5 m, for a length of 1.5 m, by the installation of 3 belts side by side. The central belt is 6.7 m long and the two side belts are 1.5 m long, extending from the front of the central belt to the front wheels.

The longer, 6.7 m central belt provides a good simulation of road motion even for very long cars, having about 1 m of moving ground ahead of the car and 1 m downstream of the car and its wake. It may also be used to test other long scale models such as trains or trucks, where length is the major dimension. The model scale can be increased, improving model detail, and therefore, measurement accuracy.

The maximum velocity of the three belts has been increased to 250 km/h (it was 200 in the old system), to reach the same maximum speed as the wind. This increased test speed is necessary to uncover the aeroacoustic sources that appear at high speed only and are caused by the deformation of body parts. It may be also important for the measurement of the deformation of some add-on aerodynamic parts of racing cars.

The presence of an upstream car, (racing or passenger), with its down-lifting or up-lifting vortices can be easily simulated with the TGS (Turbulence Generation System) and that further improves the simulation of the road condition.

Technical Specifications

Dimensions of the facility

Test Section

- Plenum Length = 13.30 m
- Jet Length = 8.00 m
- Width B = 9.60 m
- Height H = 4.20 m
- Balance reference center X/L = 0.46

Nozzle

- Jet frontal area An = 11 m2 (Semi-circular shape)
- Width Wn = 4.84 m
- Height Hn = 2.82 m
- Contraction ratio = 6.9:1

Drive system

Main Fan:

- DC Motor Power = 1.1 MW
- Fan Diameter = 4.88 m
- Number of Blades = 29

13 Fans:

- DC Motor Power (tot) = 2 MW
- Fan Diameter = 1.8 m
- Number of Blades = 13

Aerodynamic characteristics

- Max Wind Speed Vw = 70 m/s (250 Km/h)
- Velocity uniformity dV / Vw < ± 0.5 %
- Turbulence level = 0.3%

Mean flow angles:

- vertically a = 0.0°
- horizontally a = 0.0°

Max local flow angles:

- vertically a = ± 0.5°
- horizontally a = ± 0.5°

Boundary layer displacement thickness, at the balance centre and V=140 Km/h:

- static floor d* = 11.2 mm
- moving floor d* = -0.1 mm

Aeroacoustic characteristics

Noise Level measured in the Test Section Plenum, out of the jet, at x=balance centre:

- SPL (Aw) = 68 dB(A) at V = 100 Km/h
- SPL (Aw) = 78 dB(A) at V = 140 Km/h [5]

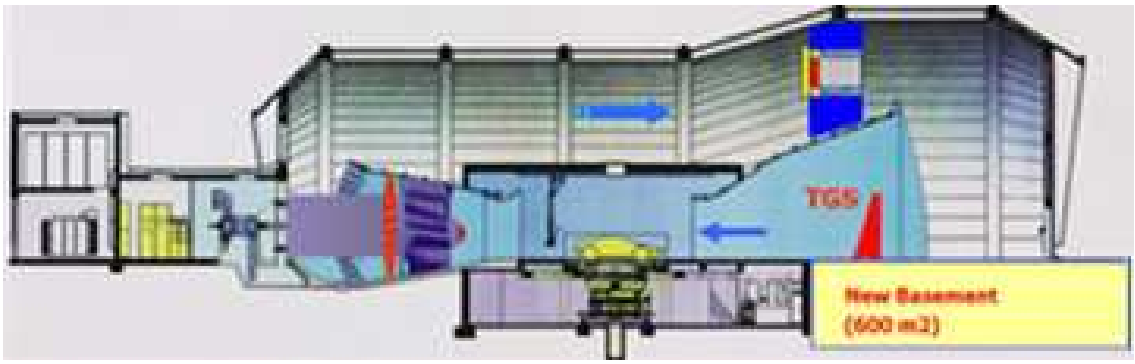

Fig. 1.2.04. Pininfarina wind tunnel. [5]

1.3 TIPICAL MEASUREMENTS PERFORMED

Typical measurements performed on motorcycle models on wind tunnel, besides the acoustic noise mentioned before, are the measurements of drag, lift and lateral forces as well as yawing, pitching and rolling moments.

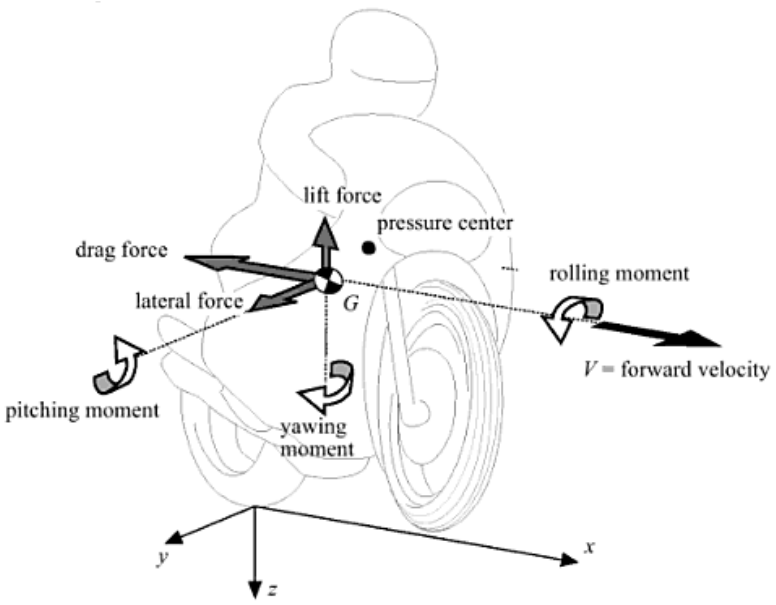

Fig. 1.3.01. Forces and moments on motorcycle. [11]

1.3.1 Drag force.

An object moving through a gas or liquid experiences a force in direction opposite to its motion. This force is called *drag*. Drag is obtained by the next equation.

$$D = \tfrac{1}{2} \rho \cdot C_D \cdot A \cdot v^2$$

where

- ρ represents the density of the air (1.167 kg/m^3 at atmospheric pressure 987 bar and 20ºC temperature).
- C_D represents the drag aerodynamic coefficient.
- A represents the frontal area.
- v represents the motorcycle speed.

The drag force is the addition of three components:

1. Due to a dissipative phenomenon like the friction. Also due to the surface roughness.
2. Due to the form of the vehicle considered.
3. Due to the three-dimensional problems of the boundary.

Some Cd values are:

MOTORCYCLE	**C_DA (m^2)**	**Cd**
Honda RS125 1990	0,193238	0,64
Suzuki Hayabusa	0,313083	0,56108065
Kawasaki ZX-12R	0,340954	0,60239223
Suzuki GSX-R750	0,324231	0,71181339
Suzuki 600 Bandit	0,366037	0,80359385

Table. 1.3.01. C_D values for different motorcycle models.

Usually, the motorcycle's aerodynamic characteristics are represented by the product $C_D \cdot A$. The experimental model is in 1:10 scale, so this product can not be compared to the experimental results due to the difference between the areas. In table 1.3.01 are shown the C_D values in order to compare to the experimental results because this dimensionless coefficient can be compared although the difference between the areas.

1.3.1.1 Friction drag.

The friction drag is due to the viscosity of the fluid. Referencing the Prandtl hypothesis, in a fluid with a high Reynolds number which flows around of an object, the effects due to the viscosity forces are not only present in a zone closed to the object (called boundary layer) in which the adherence condition should be satisfied. That means that the velocity of the fluid in the entire surface should be null.

Fig. 1.3.01 shows this condition of null velocity in the contact zone between the fluid and the object.

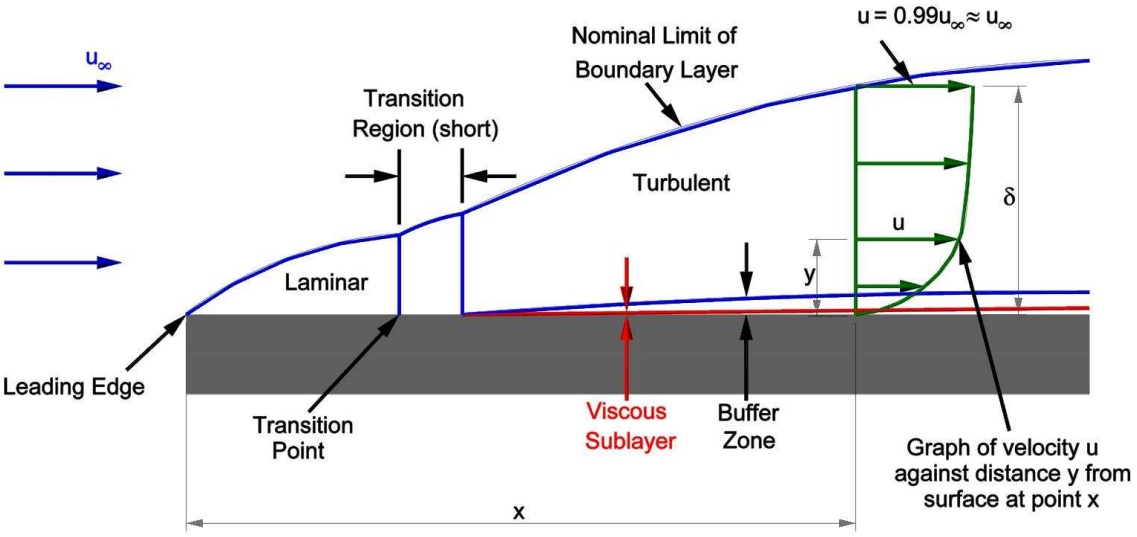

Fig. 1.3.02. Boundary layer. [12]

The friction due to the fluid motion around of an object provokes that part of the fluid kinetic energy changes to heat, and then the object suffers a force with the opposite direction to the fluid velocity. The value of this force will be function of the Reynolds number. In the turbulent boundary layer configuration the interchange of movement quantity in the fluid particles will be higher with the direct consequence of a higher force over the object. The next equation justifies this behaviour and it is also valid for laminar boundary layer configuration.

$$\tau_w = -\mu \left| \frac{\partial u}{\partial y} \right|_{y=0}$$

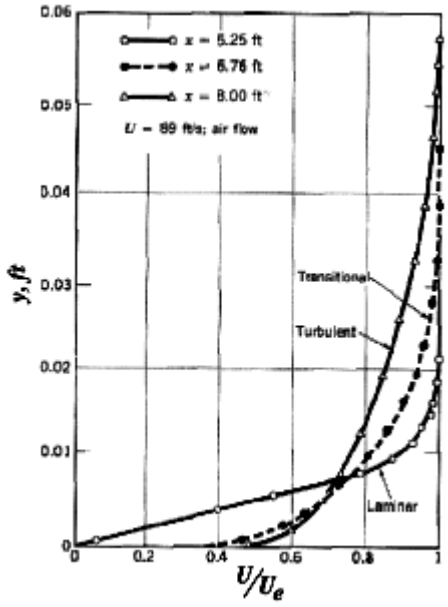

Fig. 1.3.03. Boundary layer height in laminar and turbulent configurations.

In a motorcycle, the boundary layer will be present along the entire surface becoming higher along the surface covered in the motorcycle. Fig. 1.3.03 shows this evolution of the height of the boundary layer.

Fig.1.3.04. Evolution of the boundary layer around the motorcycle. [13]

1.3.1.2. Form drag.

It is also called pressure drag. Form drag is due to the pressure distribution over the body surface. Consequently, the boundary layer is separated due to the pressure gradient or due to the higher variation of the form of the object.

As in the case of the friction drag, the form drag value depends on the boundary layer configuration. If the boundary layer is turbulent, the drag will be higher than in the laminar case. This is why bigger variations of the motorcycle fairing or any other interruption of the surface can provoke the boundary layer separation. Motorcycle is a vehicle characterized by an external surface very discontinuous which provokes local pressure variations that have negative effects over the aerodynamic.

This kind of resistance is very dependent on the shape of the object. In fact, this resistance is predominant in case of non aerodynamic objects, but not in the aerodynamic objects in which this drag component can be negligible.

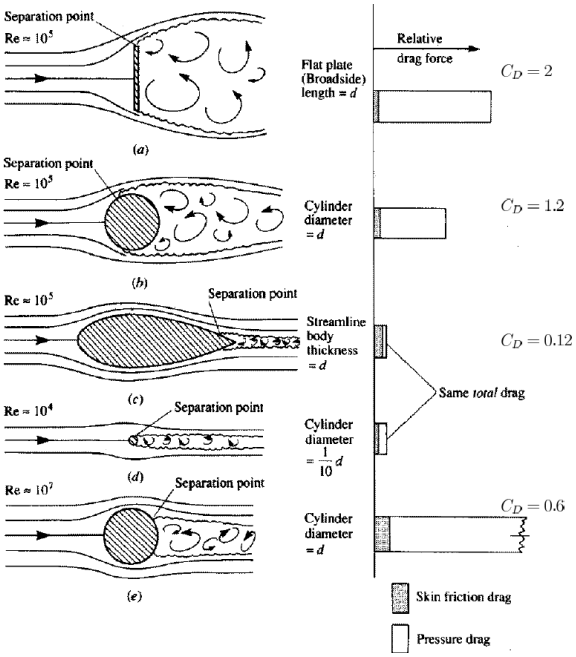

Fig. 1.3.05. Friction drag (grey) and form drag (white) in different objects. [14]

The separation of the boundary layer is produced where the pressure becomes higher in the direction of the motion. In mathematic language, it happens when there is a pressure adverse gradient which is $\frac{\partial p}{\partial x} > 0$.

In a motorcycle, this kind of resistance is the most important component. This is due to the streamline present and, indirectly, because of the viscosity.

1.3.1.3. Induced drag.

Lift-induced drag (also called induced drag) is drag which occurs as the result of the creation of lift on a three-dimensional lifting body, such as the wing or fuselage of an airplane or the spoilers in a vehicle. Induced drag consists of two primary components, including drag due to the creation of vortices (vortex drag) and the presence of additional viscous drag (lift-induced viscous drag). The vortices in the flow-field, present in the wake of a lifting body, derive from the turbulent mixing of air of varying pressure on the upper and lower surfaces of the body, which is a necessary condition for the creation of lift.

Lift generated by a body increases as the lift-induced drag increases. For an aircraft in flight, this means that as the angle of attack, and therefore the lift of the lifting body, increases to the point of stall, so does the lift-induced drag. At the onset of stall, lift is

abruptly decreased as is lift-induced drag, but viscous pressure drag increases due to the formation of turbulent unattached flow on the surface of the body.

1.3.2. Lift force.

Lift is the component of the aerodynamic force which is perpendicular to the oncoming flow direction. Lift force is obtained by the next equation:

$$L = ½ \rho \cdot C_L \cdot A \cdot v^2$$

In automobile field the lift has only a negative effect, because it is a force whose existence provokes loosing of adherence with the direct consequence of lost in the stability.

The automobile designers try to develop their vehicles using a negative lift to win more stability. Thus, the vehicle is fixed to the road and that also provokes a better traction.

In most of the vehicles, the lift is generated by spoilers with negative-lift surfaces, but the sport vehicle models are designed in order to achieve this effect without using the spoilers.

Another system to make the vehicle more stable is generating a Venturi effect between the lower part of the vehicle and the road, in order to achieve more adherence to the road.

Typical values for lift force in motorcycles are between 0.06 and 0.12 m^2. [15]

1.3.3. Lateral force.

In motion, a vehicle can be exposed to some lateral winds, because of a curve in the track or because of exiting a tunnel.

This has an effect which develops a lateral force that is function of the yawing angle. In fact, as the beta angle becomes higher, the lateral force will increase, and the air flow will be separated in the opposite side to which the wind comes from.

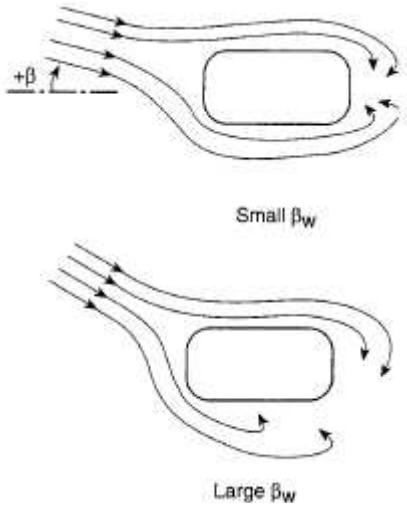

Fig. 1.3.06. Yawing air angle effect. [14]

The lateral force, like in the other aerodynamic forces, will be located at the vehicle pressure centre. The study of this phenomenon is very important in order to ensure the vehicle lateral stability. If the vehicle's pressures centre and the vehicle's barycentre does not coincide at the same point, it will exist a rolling moment and also a yawing moment.

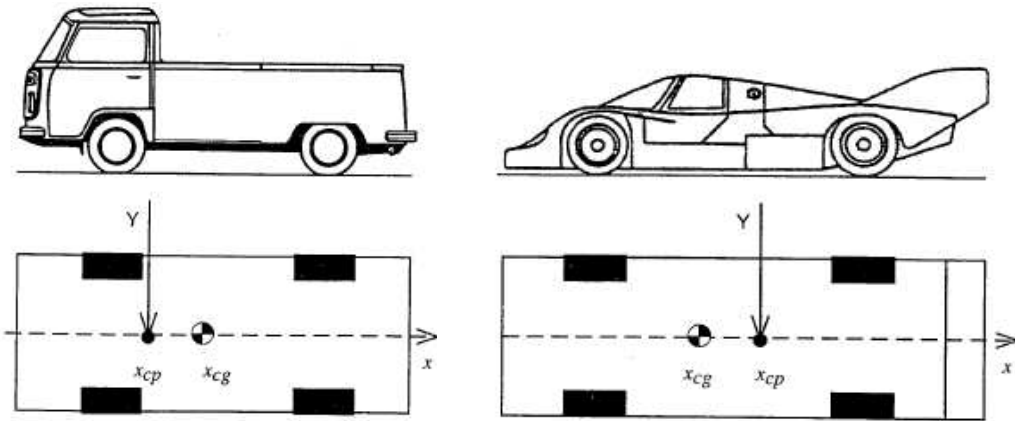

Fig. 1.3.07. Different positions of pressures centre and barycentre on vehicles. [14]

1.3.4. Pitching moment.

The pitching moment is one of the six components which increase more with the velocity of the air. In fact, it is the highest moment measured in the wind tunnel experiments. This moment provokes that the front wheel tends to lift and the rear wheel tends to be more charged. This effect increases with the quadrate of the speed. At very high speeds it can become so important that the front wheel loose the adherence with the consequent effect that the motorcycle cannot be driven. This moment is also function of the vehicle inclination and of the shape of the vehicle.

Notice that in the experiments of this thesis, the measurements have been done without the pilot on the motorcycle. It is a very important detail taking into account that the pilot will transmit a big part of his load to the front wheel.

1.3.5. Yawing moment.

As it is explained in the lateral force, this is an effect that exists in non-symmetrical motion. In the study of the yawing moment is important to know the position of the pressures centre and the distance between this centre and the vehicle's barycentre.

In the case of a hard lateral wind or in a curve, the lateral force will have a not null component in the configurations shown in fig 1.3.07. In the design process, it is important to try to get coincidence of pressures centre and barycentre at the same point.

1.3.6. Rolling moment.

As in the yawing moment, this moment is due to the non-symmetrical air flow around the motorcycle. It is particularly important when the motorcycle is in a curve because of the centrifuge force. The motorcycle will be sloped with respect to a vertical axis so the pressures centre of the vehicle and the barycentre will not be at the same line with respect to the vertical axis.

In this configuration, the rolling moment will be generated by the contribution of the lift and the lateral forces, then depending on the value and directions of these two forces, rolling moment will be higher or lower.

CHAPTER 2

DESCRIPTION OF THE PRESENT EXPERIMENTAL SET-UP

2.1 MOTORCYCLE MODEL.

A motorcycle model of a Yamaha M1 in a 1:10 scale of Tamiya enterprise has been used to perform the wind tunnel experiments.

The basic characteristic of the model is the absence of a pilot, which is very important feature in motorcycle testing in wind tunnel because of the front area introduced by him. It is important to take into account this aspect because of its effect over the load distribution on the wheels. With the presence of a pilot there may be less pitching moment than the measured in this experiment without him.

Table 2.1.01 shows different C_DA values [16] depending on the pilot is prone (aerodynamic position) or sitting. In this table can be observed that the presence of the pilot and his position can provoke high C_DA values.

MOTORCYCLE	RIDER PRONE C_DA (m^2)	RIDER SITTING C_DA (m^2)
Honda VF1000F	0,40	0,46
Aprilia Mille	0,52	0,61
BMW R1100 RT	0,53	0,97
Yamaha R1	0,57	0,62
Kawasaki GPZ 900R	0,36	0,43

Table 2.1.01. C_DA values depending on the pilot's position. [16]

Another important characteristic in this case is that the wheels cannot move because it was necessary to block the wheel's motion with screws to fix the model to the dynamometric balance as shown in fig 2.3.02 in the "platform for motorcycle model" section.

Fig. 2.1.01. Front view of the model.

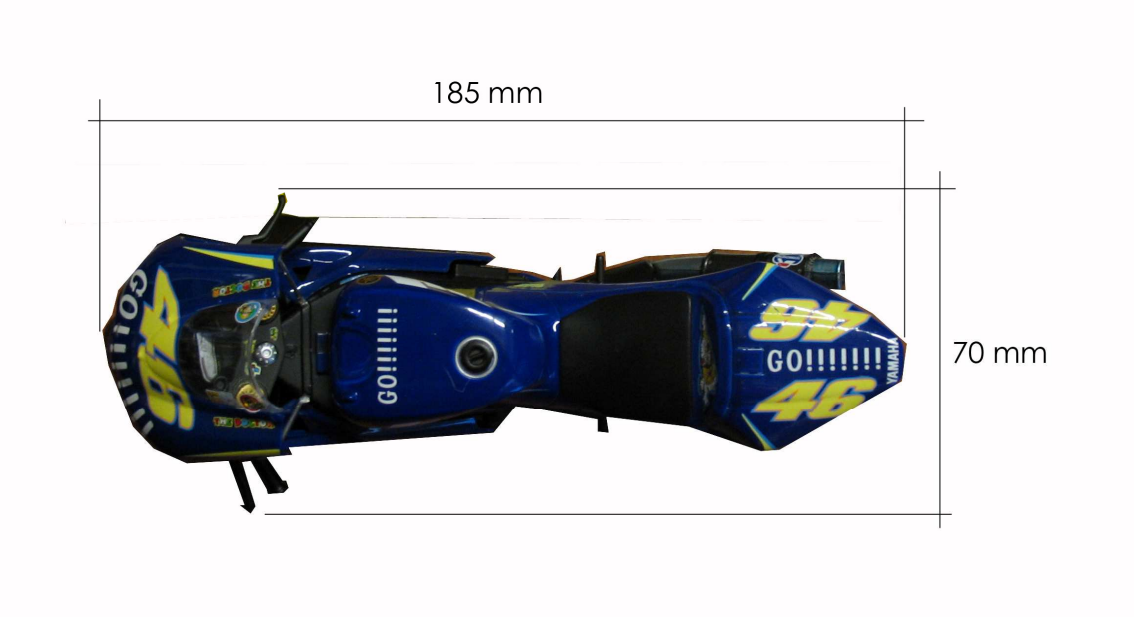

Fig. 2.1.02. Upper view of the model.

2.2 WIND TUNNEL

The experiments of this thesis have been developed in the wind tunnel of the university “Università degli studi La Sapienza di Roma”. This wind tunnel is placed in the aeronautic and mechanics laboratory of the engineering faculty.

This wind tunnel is subsonic and with closed test section, as shown in fig. 2.2.01.

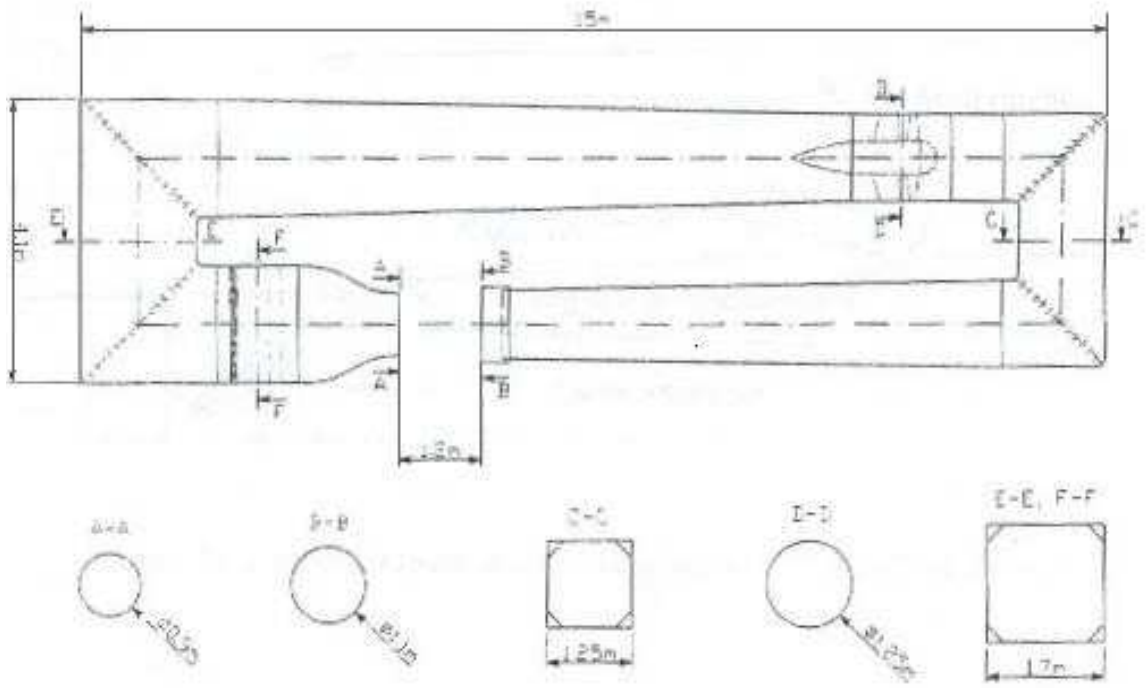

Fig. 2.2.01. Wind tunnel of “la Sapienza” university of Rome. [14]

Its principal characteristics are:

- A test section of 1,2 m length. Between entry and exit air, an area difference of 0,6 m^2 has been calculated. The exit area is 0,9 m^2 and the entry area is 1,5 m^2. This area difference between exit and entry of air in the circuit is because the flow tends to be higher as mentioned in the chapter 1.

- The three-phase asynchronous motor has a maximum power of 50 KW. It is composed of an axial ventilator with 9 fans with variable heating. This wind tunnel provides a maximum speed of 50 m/s.
- Reposed air section with a honeycomb mesh.

- Convergent with ratio A_{entry}/A_{exit} = 4,4 m and 1,5 m long.

- Conic collector necessary to channel the flow into the diffuser and keep the pressure as constant as possible along the central axis
  (Dext = 1.05 m, Dint = 1.21 m).

- The diffuser is 4.95 m. long. It is developed from the exit test section up to the first elbow of the circuit, with a divergence angle of 1.157º. In this part of the circuit, the air tends to slow down in order to restore the static pressure in the lower distance as possible. In this way less power is lost, because the power loss is proportional to the wind speed raised to the cube.

- Elbow with 24 fins to detour the flow. [14]

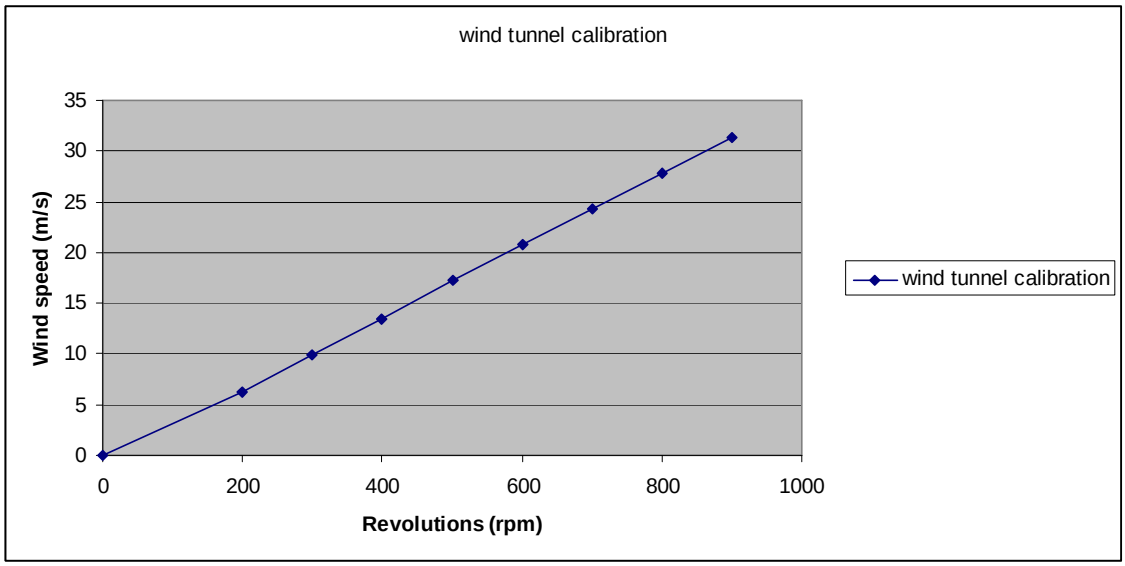

Fig. 2.2.02: Wind tunnel calibration line.

The wind tunnel calibration line has been obtained during the experiments, which makes possible to calculate the necessary revolutions to obtain the desired experimental speed. The wind speed is measured by a pitot-anemometry CTA system which is situated at the wind tunnel test section. The speed of the wind can be considered proportional to the revolutions of the ventilator, when the regulation pressure is at 2.1 bar and the heating of the fans has been fixed.

2.3 PLATFORM FOR MOTORCYCLE MODEL

The platform for the motorcycle model is inside a table as shown in Fig 2.3.01. This table is situated in the wind tunnel test section for the experiments. The platform is like the

platforms commented in the chapter 1, with a circle platform in order to change the angle of attack of the experiments to do measurements with lateral wind.

The experiments have been done with an angle of attack of -30º, -20º, -10º, 0º, +10º, +20º and +30º. The platform and the dynamometric balance are fixed so when the platform is turned to another angle of attack, the dynamometric balance and the moving belt system will be turned the same angle. This is very important because in this way, the cells Ds and Dd will measure the drag in the longitudinal direction and the cells Ys and Yd will measure the drag in the lateral direction. Thus, the calculation of the non-dimensional coefficients like C_L or C_D will be easier.

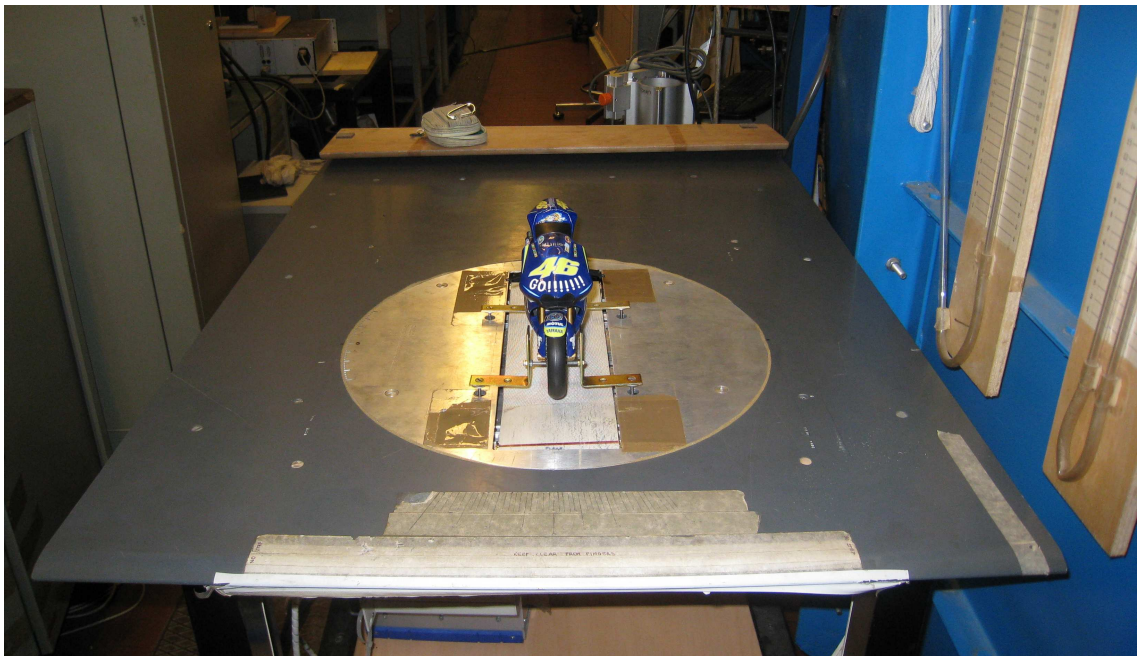

Fig. 2.3.01. Platform for motorcycle model

Fig 2.3.02 shows the fixation used on the motorcycle model. Notice that the wheels can not move so this movement will not be simulated in the experiments. Two squares and two screws, the latter allocated between the spokes of the wheels, have been used to fix each wheel.

In the first experiments it was observed that with high speed of wind, the motorcycle moves a little and that one side is more loaded than the other. The latter it will be explained in chapter 4 “results of the measurements on the motorcycle model”. This movement is

because the fixation is not specifically for motorcycle models. The moving plate of the dynamometric balance and the platform of the wind tunnel are specially designed to fix a car. That is why they have been adapted for this motorcycle model using these holes of the dynamometric balance and of the platform which were not designed for this fixation.

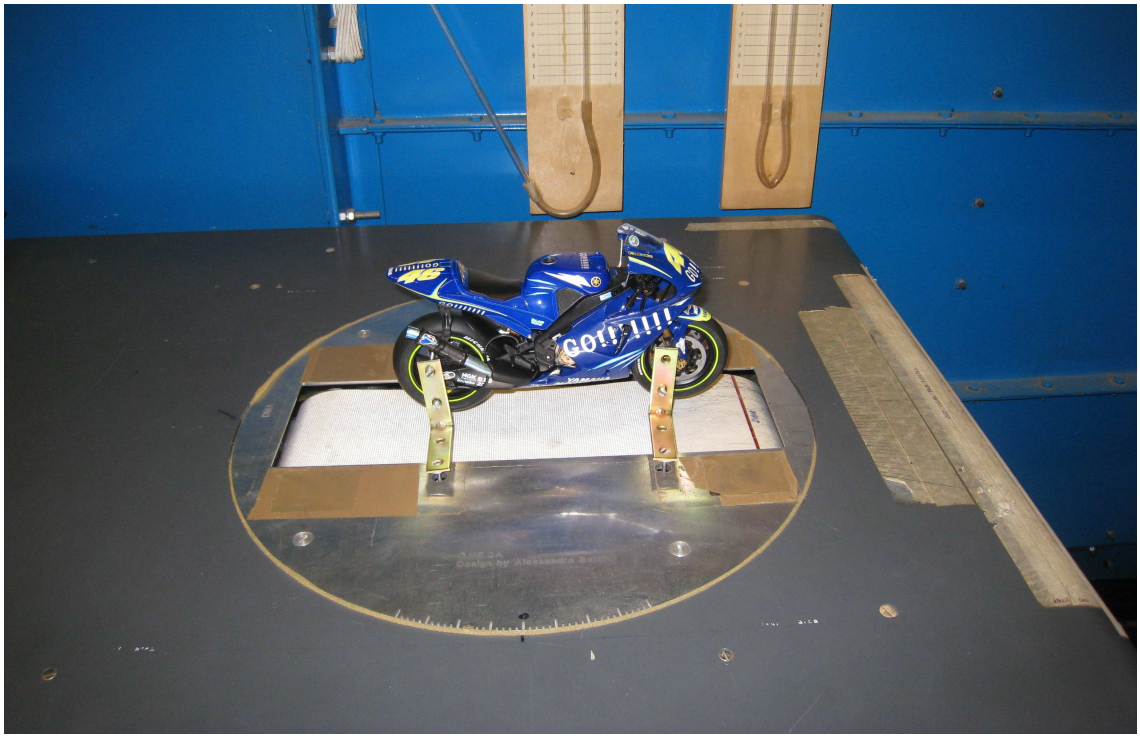

Fig 2.3.02. Fixation of the motorcycle model

Fig. 2.3.03 shows how the motorcycle model is elevated from the platform in order to communicate the forces to the dynamometric balance. If the model was touching the platform, the forces would be transmitted to the table but not to the balance. It can also be observed that the fixation introduces a little front area. This factor will be considered in the analysis of the results.

The boundary layer existing between the motorcycle and the platform is eliminated using the moving belt system to simulate the ground effect.

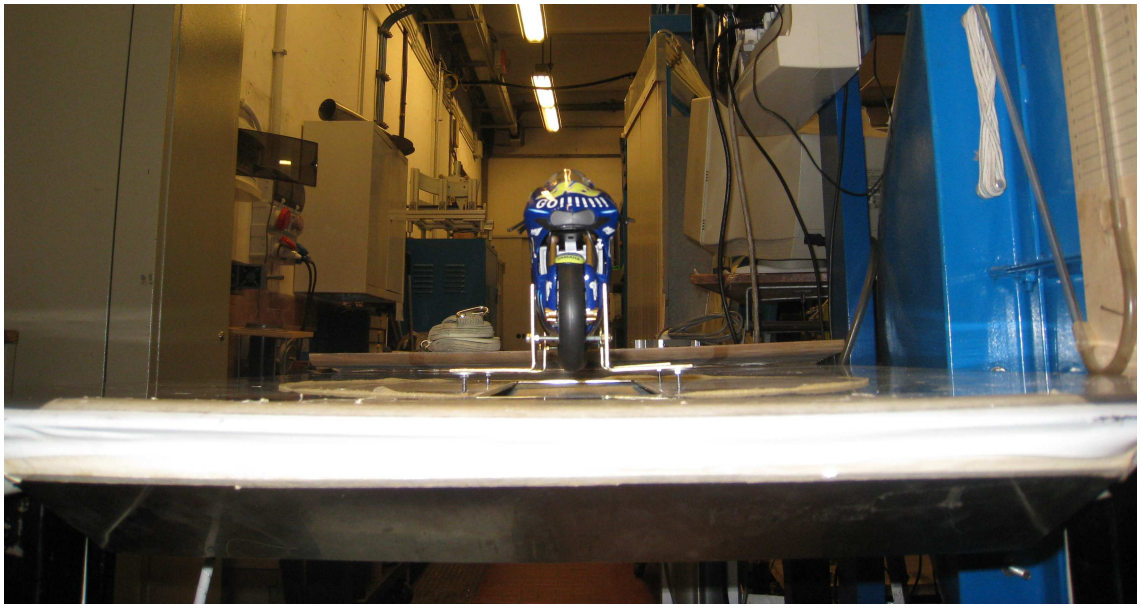

Fig. 2.3.03. Front view of motorcycle fixation

2.4 DYNAMOMETRIC BALANCE

The six component dynamometric balance has 8 cells in order to measure all the components of forces and moments over the motorcycle model. The first 4 cells Fs, Fd, As and Ad, are situated under the moving plate. The measures of these cells are used to calculate lift force and pitching and rolling moment. These cells have 100N of full scale. Also there are another 4 cells allocated at the perimeter of the moving plate. These cells are called Ds, Dd, Ys and Yd, and they are used to calculate the drag and lateral forces and the yaw moment. These cells have 50N of full scale. [17]

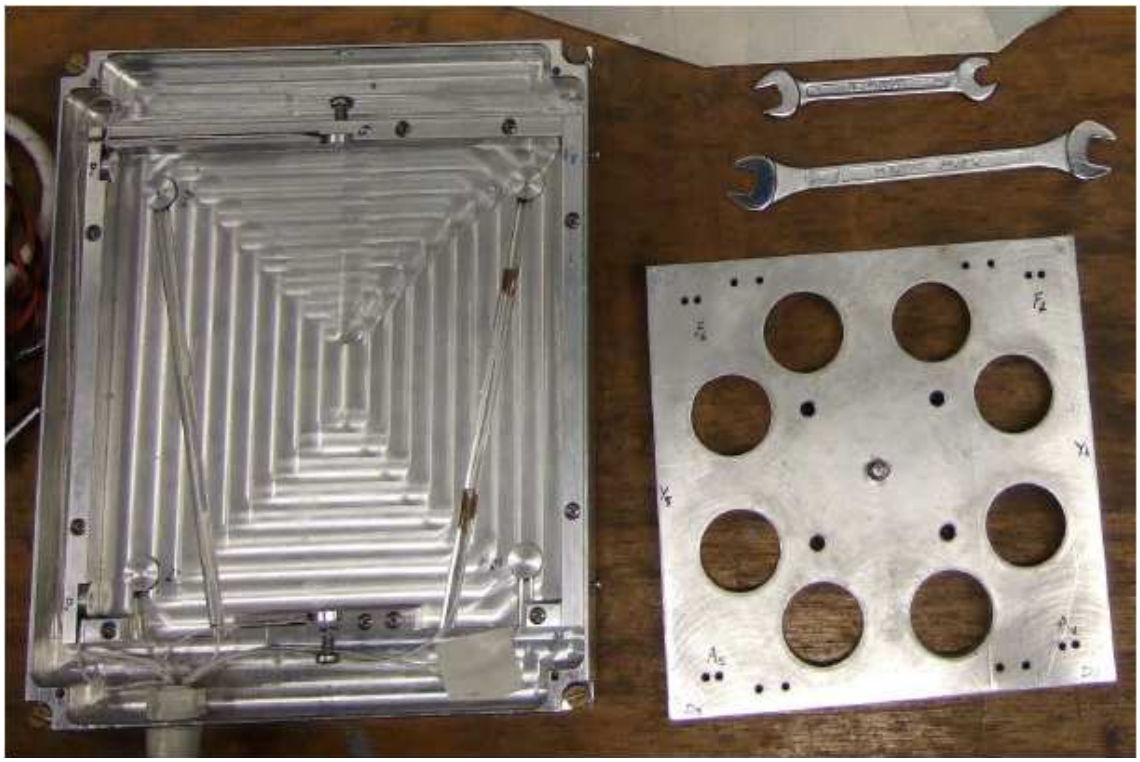

Fig. 2.4.01. Upper view of the dynamometric balance.

Each cell can be pre-charged with a screw. In the Fs, Fd, As and Ad cells the screw is situated under the cells in order to apply more or less pressure between the cell and the moving plate. In the Ds, Dd, Ys and Yd cells, the screws are situated in the opposite side of the moving plate. The pre-charge must be adequate to the measured forces and the model weight because with a hard pre-charge the cells will not measure big forces because it will arrive very soon to the full scale. On the other hand, with a light pre-charge it will not measure smaller variations.

Notice that during the calibration experiments it has been observed that the cells tend to lose the pre-charge because the screws tend to unscrew. Consequently during the wind tunnel campaign the forces measurements, in one experiment will measure smaller values than in the previous experiment, and the repeatability of the measurements may be low. It can also provoke an unbalancing of the moving plate and one cell will be more pre-charged than the other one. So the solution has been the use of *Teflon* in the screws trying to minimize this effect.

Fig. 2.4.02. View of the screws to pre-charge each cell.

Bear in mind in the calibration phase that the first step is to put all the cells at the same height in order to level the moving plate to minimize the unbalancing, but it will be explained better in the chapter 3.

2.5 ACQUISITION SYSTEM

The forces on the cells are measured with a *National Instruments* rack (Fig. 2.5.01) in which has been applied an acquisition range of 5 mV/V in all the cells but not in the Yd cell in which has been applied 20 mV/V because its “zero” point is higher than in the other ones.

Fig 2.5.01. *National instruments* rack

From the rack, the signals are treated in a *Labview* 7.1 program with the next characteristics.

- The 8 cells data acquisition in real time, in order to obtain the results for the same time interval and in the same experimental conditions.

- 30 seconds of acquisition time with 30000 samples and $\Delta t = 0.001$ s.

- Static analysis of voltage values in each cell. Arithmetic mean (of the voltage and the force), standard deviation (of the voltage and the force), range (of the voltage), number of samples and time increment are obtained.

- Conversion of the mean voltage value to Newton. The conversion constants used are the constants found by engineer Marco Nunez.

- Forces and moments results. In order to obtain them, the next relations between the cells measurements have been used.

- Lift = Fs + Fd + As + Ad
- Drag = Ds + Dd
- Lateral force = Yd – Ys
- Pitching moment = a (As + Ad – Fs – Fd)
- Yaw moment = b (Ds – Dd)
- Rolling moment = b (Fd + Ad – Fs – As)

being a = 7 cm the longitudinal distance between front and rear cells and b = 7,87 cm the transversal distance between right and left cells.

The *LabVIEW* program is structured in two parts. First, the block diagram in which the entire program is represented in block boxes diagram (as its name indicates) where the data acquisition and analysis are performed. On the other hand is the front panel where the results of each cell are visualized: voltage, force, arithmetic mean, range, etc. Also there is for each cell a diagram in which is visualized the voltage signal vs. time measured in the acquisition system of the National Instruments.

In order to reset all the forces and voltage forces, there is a button to set “zero” and obtain a null output in all the cells values.

This value can change because of the pre-charge or because of the load, so it should be reset before each experiment.

2.6 MOVING BELT SYSTEM

This moving belt system is used in order to simulate the ground effect of the vehicles in motion. This moving belt system is integrated with the dynamometric balance as shown in fig 2.6.01. The base of the moving belt system has holes to fit the dynamometric balance, and it was designed so that once the dynamometric balance is introduced in the platform of the table, the moving belt system will be at the same height as the table to simulate the ground effect.

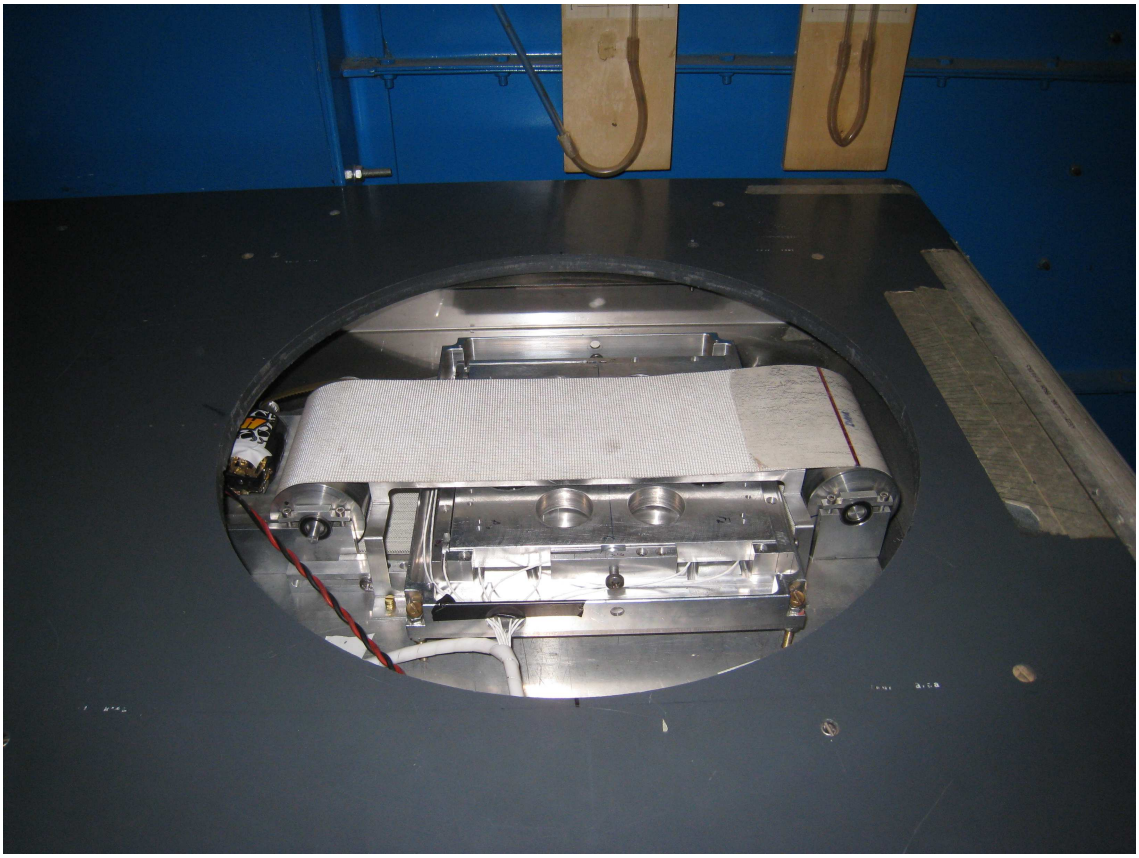

Fig. 2.6.01. Moving belt system

This moving belt system is composed by:

- Two aluminium alloy cylinders
- Base to integrate the dynamometric balance.
- Polyurethane belt. Measures 760 x 95 x 1,5 mm
- Four ball bearings SKF shielded 61800-2RS 1
- Four bearing-covers.
- Supports for front and rear cylinders.
- Synchropower belt to transmit the motor movement to the rear cylinder.
- Four screws M4x10
- Four screws M2x20
- Two screws M3x6
- Four screws M3x5
- Four screws M3x20

After the belt system assembly, the motor calibration was done using a continuous current power supply. To know the belt speed, a stroboscopic lamp was used.

Due to the low power of the motor, it was observed that with a belt high tension, the motor cannot move the belt, so the first step was to decrease the belt tension.

Once the belt was moving, it was tried to calibrate the motor in order to know the voltage and the intensity needed to have a determined belt speed.

Table 2.6.01 shows the first calibration test, in which a very low speed and high voltage and current (high power) were observed. The motor was overheated. So it was proceeded to decrease a little more the belt tension.

Voltage (V)	Current (A)	Cylinder revolutions (rpm)	Cylinder revolutions (rad/s)	Speed of belt (m/s)
2,5	10,7	368	38,53696	2,042459
3	11,7	710	74,3512	3,940614
3,5	12,8	665	69,6388	3,690856

Table 2.6.01. First motor calibration test

Once decreased the belt tension, it was proceeded to the second calibration test, obtaining table 2.6.02.

Voltage (V)	Current (A)	Cylinder revolutions (rpm)	Cylinder revolutions (rad/s)	Speed of belt (m/s)
2,5	11	560	58,6432	3,10809
3	12,1	590	61,7848	3,274594
3,5	13,4	850	89,012	4,717636
4	15,1	1181	123,6743	6,554739
4,5	16,2	1170	122,5224	6,493687

Table 2.6.02. Second motor calibration test.

Once again, there was low speeds and high power consumed, therefore the belt tension was decreased a little more.

Table 2.6.03 shows the third calibration test, in which the first three values of the intensity have not coherence, because the voltage should increase and the intensity too, but the behaviour is not the expected.

Voltage (V)	Current (A)	Cylinder revolutions (rpm)	Cylinder revolutions (rad/s)	Speed of belt (m/s)
3	12,7	1120	117,2864	6,216179
3,5	10,5	1690	176,9768	9,37977
4	10,2	2280	238,7616	12,65436
4,5	10,8	2625	274,89	14,56917
5	11,3	3030	317,3016	16,81698
5,5	12,3	3366	352,4875	18,68184
6	12,8	3725	390,082	20,67435

Table 2.6.03. Third motor calibration test.

In order to check if there was results repeatability, a fourth calibration test was carried out, obtaining the results shown in table 2.6.04.

Voltage (V)	Current (A)	Cylinder revolutions (rpm)	Cylinder revolutions (rad/s)	Speed of belt (m/s)
2	8,5	1360	142,4192	7,548218
2,5	9,1	2100	219,912	11,65534
3	9,9	2795	292,6924	15,5127
3,5	10,5	3331	348,8223	18,48758
4	10,5	4225	442,442	23,44943

Table 2.6.04. Fourth motor calibration test

Notice that any result is repeated in any of the experiments. For example, 3V correspond to 11,7A, 12,1A, 12,7A and 9,9A. Therefore, a speed value has been tried at the moment of wind tunnel experiment, but only a 10 m/s belt speed has been achieved with the values of 3,5 V and 16 A (very high value). Trying with a higher speed, the belt was derailed and blocked. It is why there is only one experiment performed with the belt system and there will be few conclusions.

CHAPTER 3.

CALIBRATION OF THE DYNAMOMETRIC BALANCE.

3.1 PROCEDURES

In the dynamometric balance, it is possible to pre-charge each cell with a screw which makes more or less pressure between the cell and the moving plate depending on the level of screwed. This is done in order to find the correct pre-charge, in which the cells work correctly.

The first step is to put at the same height (around 1 mm.) all cells in order to distribute the weight among them as much as possible. In this way it will not be any pitching or rolling moment and the experimental measures will give more realistic results.

In fact, in the first measurements performed previously to the final calibration results not all the cells were at the same height and the lift registered was not the expected. This is due to the fact that the load was not distributed in all the cells in the same level. Thus, some registered over load and others cells registered less load.

So the first step should be to check that the plate of the balance and the base of the moving plate are leveraged at the same height. This is done with the screws which are in each corner of dynamometric balance base. Also the moving plate of the balance and the

screws which did the pre-charge of each cell should be leverage at the same height with the level instrument help.

In order to do the calibration of all the cells, the calibration constants determined by the engineer Marco Nunez have been used, trying to pre-charge with the same voltage. [18]

During cell calibration it can be observed that once the cells are pre-charged, they loose this pre-charge quite fast. It was observed that in one calibration test, the distribution of the load, which affects the cells measurements, was different than in the previous experiment, being the testing time 30 s. That means that the screws tend to unscrew during the experiments, and then the pressure changes in each cell. Some cells become more loaded and others less.

The imbalance of the cells provokes an error in the moments measured because the moments are derived from the measurements of the cells. This problem should be solved increasing the friction between the screw and the whole using *Teflon* around the screws allocated under the dynamometric balance, used to pre-charge the cells Fs, Fd, As and Ad.

Once this problem is solved, the next procedure is the cell calibration. First the cells which are under the moving plate: Fs, Fd, As, Ad.

CELL	CONVERSION CONSTANT (N/V)
Fs	-10,37
Fd	-12,81
As	-10,68
Ad	-10,32
Ds	-5,232
Dd	-5,256
Ys	-5,672
Yd	-15,83

Table 3.1.01. Conversion constants found by engineer Marco Nunez [18]

The forces are proportional to the voltage measure, and this is why it is tried to pre-charge the cells at the same voltage, in order to measure the load the most distributed as possible.

Reference weights (Kg)	Fs (V)	Fd (V)	As (V)	Ad (V)
0	-0,00011524	5,8317E-05	0,0001024	3,7097E-05
0,5	-0,12186133	-0,10099867	-0,127534	-0,11665867
1	-0,25346733	-0,21637067	-0,246842	-0,22205067
1,5	-0,385666	-0,33034	-0,363507	-0,318166
2	-0,471965	-0,45569033	-0,472243	-0,453331
2,5	-0,592082	-0,55973533	-0,59867067	-0,564279
3	-0,69240467	-0,67537733	-0,71355533	-0,677438

Table 3.1.02. Voltage values in the calibration experiment

Table 3.1.02 allows getting the figure 3.1.01, where the behaviour of the value measured by each cell for increasing plate load can be observed.

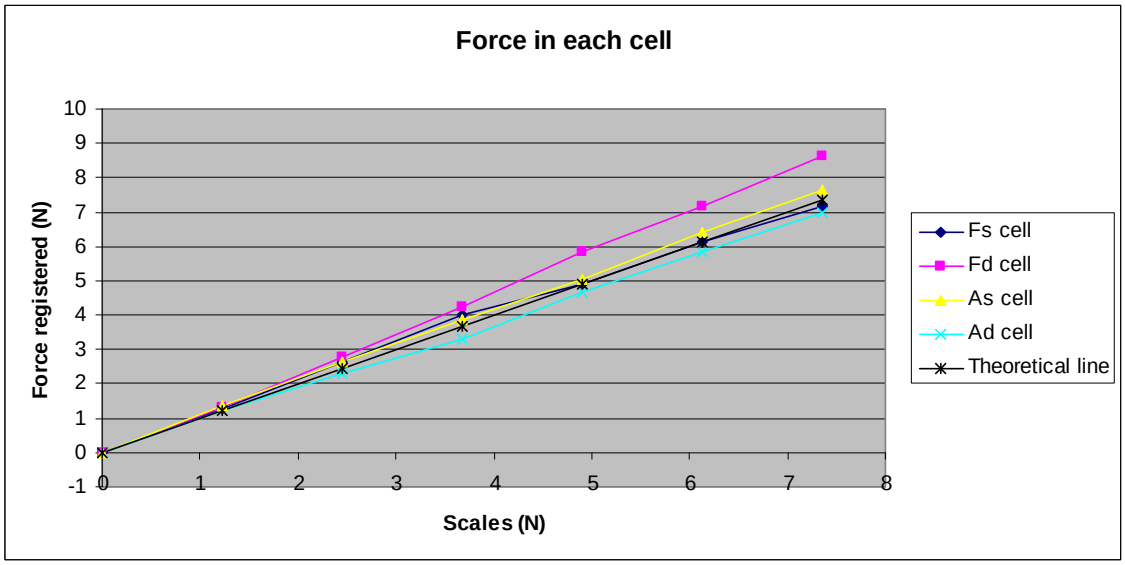

Fig. 3.1.01. Force in each cell

The aim is that all cells measure the same value in order to avoid errors in the moments measurements, because an error of the cell measure provokes an error in the moment calculated. This is due to the fact that, like it has been explained in the acquisition system in chapter 2, the moments are calculated as the product of a constant and the difference between the forces measured in the cells.

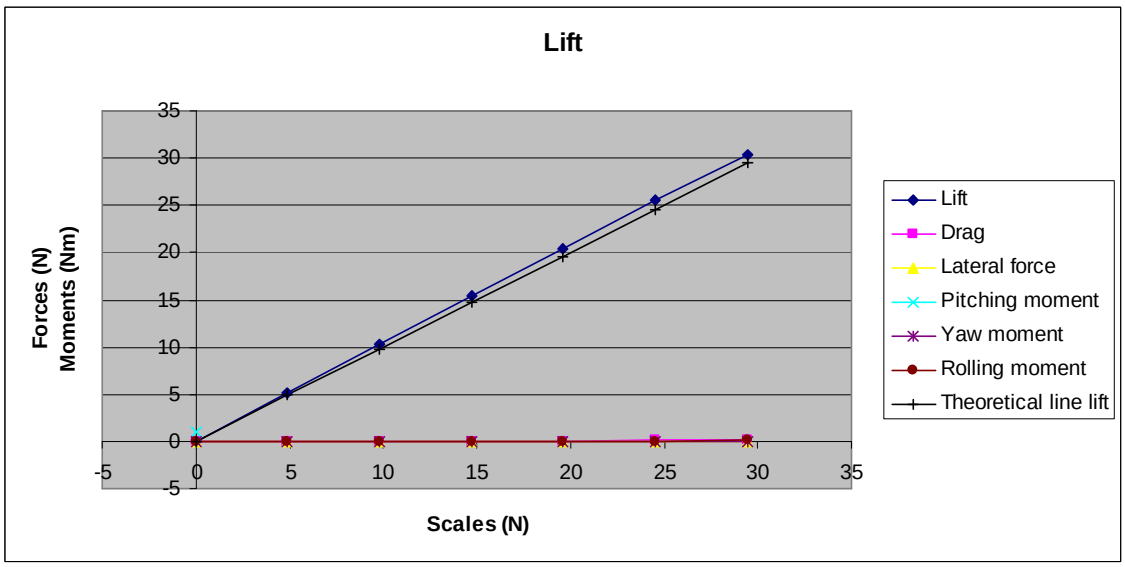

Fig. 3.1.02. Evolution of the lift registered

As shows fig 3.1.02, the lift cells measure little more than the theoretical line, but there are no problems with the moments. Even if the lift cells measure in over it is not a problem because like it has been explained, the cells tend to loose the pre-charge with time.

Once the calibration of lift cells is done, the next step is the calibration of drag and lateral force cells. First, an appropriated assembly for the measurements has to be designed. The solution purposed is the use of a pulley in order to change the vertical force into a horizontal force. This way the gravity force can be used with the same reference weights used in the lift cells calibration.

Fig. 3.1.01 shows the pulley used for the experimental measurements. As it can be observed, the position of the pulley is such that the thread is almost parallel to the moving plate. This way the drag cells Ds and Dd will measure the load of the reference weights used. However, problems with the friction will appear but this will be explained in the chapter of “solutions used to minimize the friction of moving plate”.

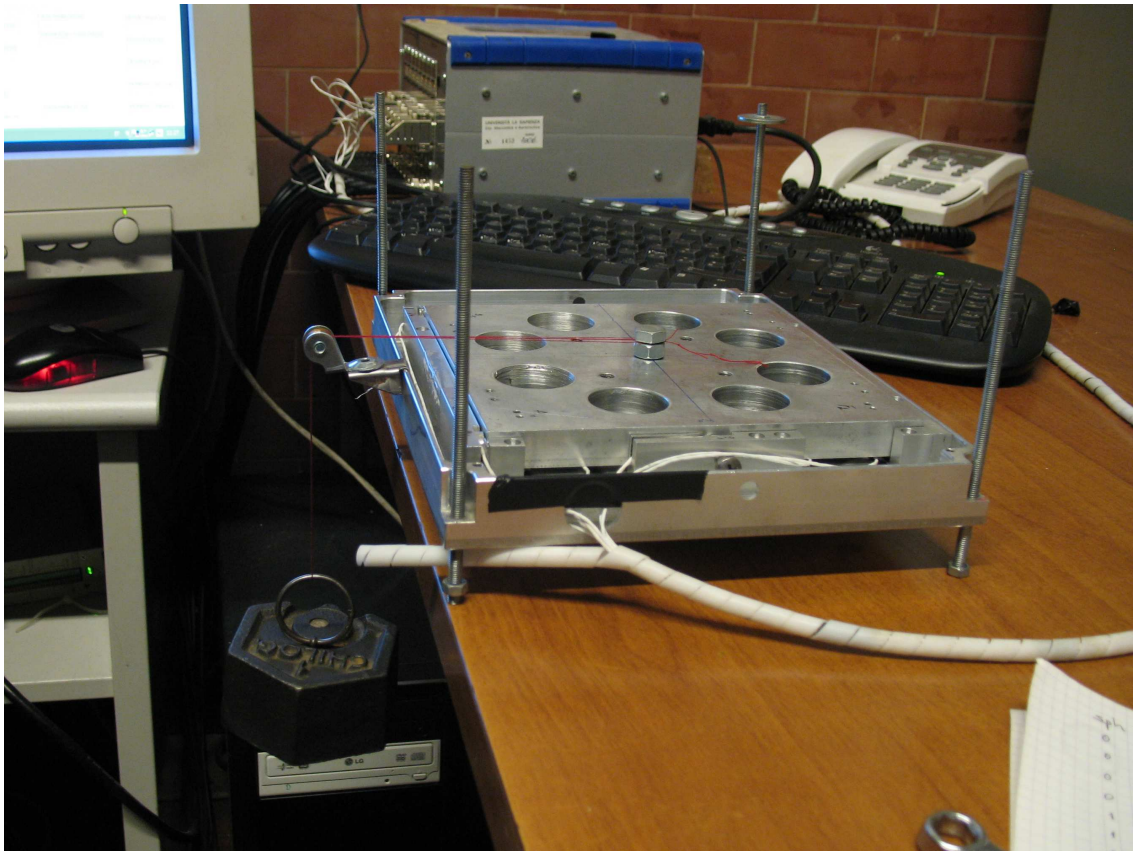

Fig. 3.1.03. Pulley used to measure the drag and the lateral force.

3.2 SOLUTIONS USED TO MINIMIZE THE FRICTION OF MOVING PLATE.

In several experiments performed the cells with the pre-charge were not working as it was expected. In one of these experiments, working in the drag cells calibration, it was noticed that these problems were due to the friction between the moving plate and the cells Fs, Fd, As and Ad. So it has been thought that one possible solution is to put some little spheres under the moving plate balance. Fig 3.2.01 shows better why the drag cells registered lower values than the theoretical because of the friction.

In this figure two of the four cells As, Ad, Fs or Fd and one of the two cells Ds or Dd are represented.

The load Q of the moving plate and the loads over it are distributed in these four cells, so each one measures Q/2 (grey). In the pulley there is a load which will be measured by the drag cells. This load is transmitted by the thread as the tension T (blue). Remember that friction is the normal multiplied by the friction coefficient and it will be in the direction opposed to the movement (red). Therefore, drag cells will measure the result of substracting the friction force μQ from the force F. This is why with the little spheres the drag cells will measure values closer to the theoretical.

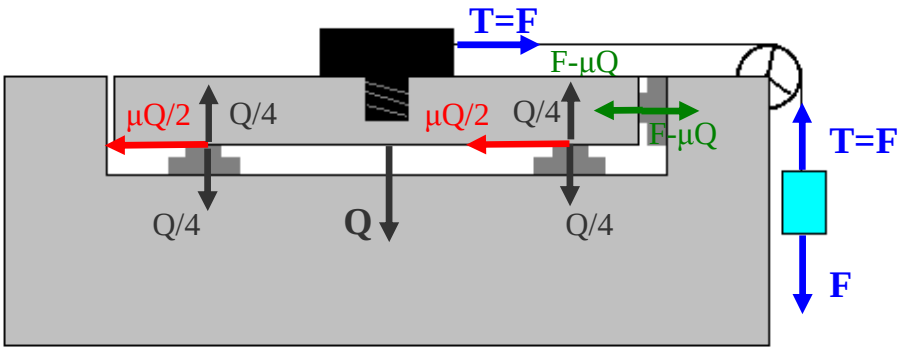

Fig. 3.2.01. Explanation of lower drag measurements without spheres

The ratio between the rotating friction force and the sliding friction force is 1:10. This is de main reason that leads to decide the use of spheres between the moving plate and the base of the balance. [18]

Fig. 3.2.02 shows in the red circles highlight, the spheres used in the experiment. These are stainless steel spheres calibrated of 3 mm of diameter.

Each sphere should support the same load in order to minimize the friction effect, because the friction is proportional to the load over each sphere. In this way, the theoretical positions of the spheres are represented in the figure 3.2.02, but due to the fact that the positions of both spheres are very close to the cell cable slots; the spheres are slightly moved to the centre of the balance.

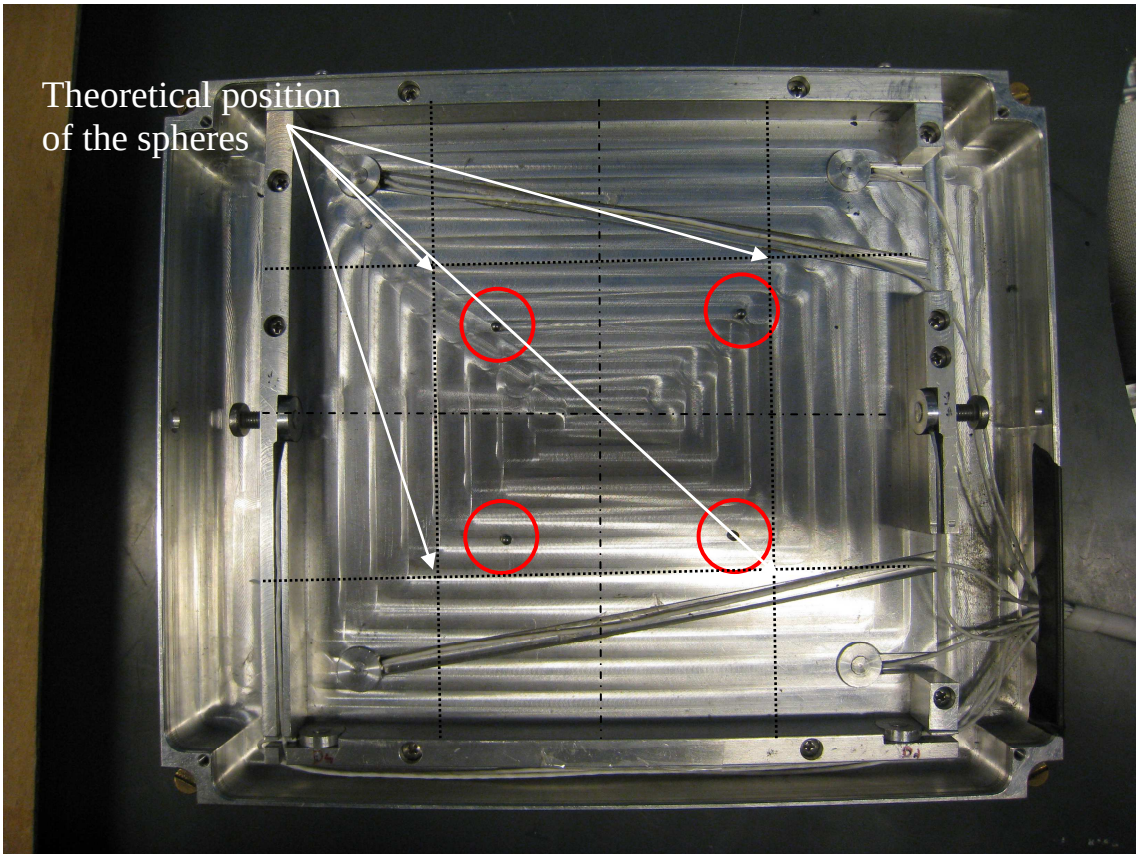

Fig. 3.2.02. Spheres used in the experiment of the drag cells calibration

But the problem is that using the spheres, not all the measurements can be done in the same experimental assembly, because with the spheres, the moving plate does not touch the lift cells so these cells do not register any value. This is not a big problem, due to the average steady nature of the problem, and the solution proposed is to perform two campaigns of measurements, first, to do the measurements with the lift cells, and one second campaign registering the cells of the perimeter using the spheres to avoid friction.

To summarize, for the calibration of the cells, a lot of experiments have been developed in order to conclude which is the more appropriated scenario to perform the measurements.

First, the measurements have been done without pre-charge and without spheres. This is a design in which the cells were not measuring the correct value of load corresponding to the reference weights used and it has been thought that this was due to the friction.

Fig 3.2.03 shows the comparison of the evolution of the measurements with the pre-charge and without the pre-charge.

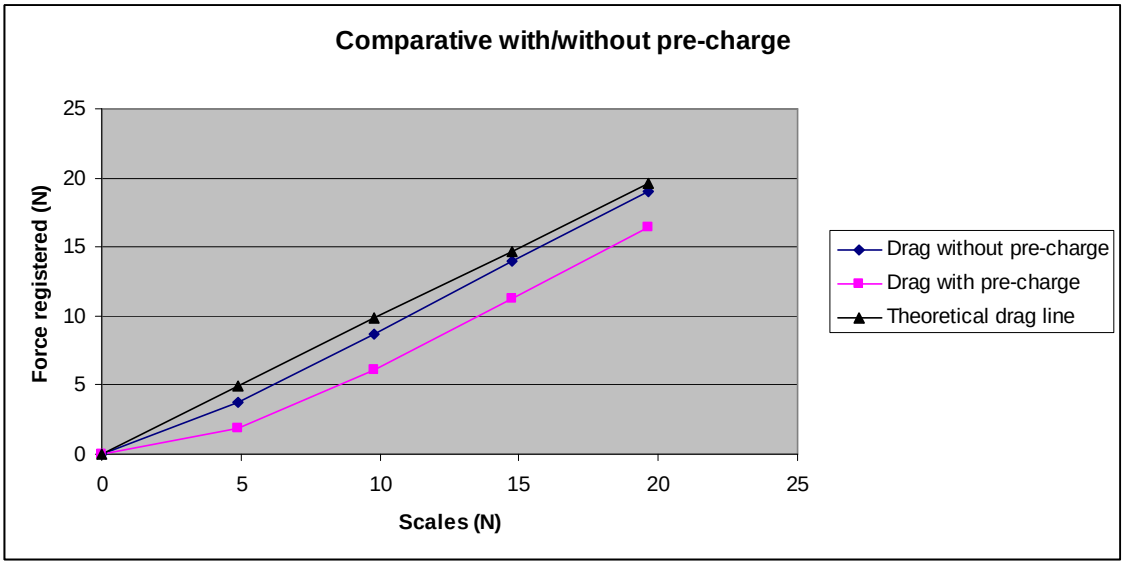

Fig. 3.2.03. Comparative with and without pre-charge

As shows fig. 3.2.03, the conclusion is that the pre-charge has a bad effect on the measurements performance, since the curve resulting from the measurements done with pre-charge differs from the theoretical results that were expected. Theoretical results are represented by the black line in which represents that if there is 9,8 N on the pulley, drag measured should be 9,8 N. This is why the campaign of measurements in wind tunnel will be done without pre-charge. And even avoiding the use of the pre-charge, the cells do not work so precisely as expected, and it has been thought that it could be due to the friction between the cells and the moving plate of the dynamometric balance.

EXPERIMENT	MEAN SQUARE DEVIATION
♦ **Drag with pre-charge**	9,125937473
■ **Drag without pre-charge**	0,670718689

Table 3.2.01. Mean square deviation of each experiment.

A possible solution to this problem is the use of some small spheres under the moving plate. So the next comparison is between the cases with and without spheres, checking also the previous analysis, with and without pre-charge too.

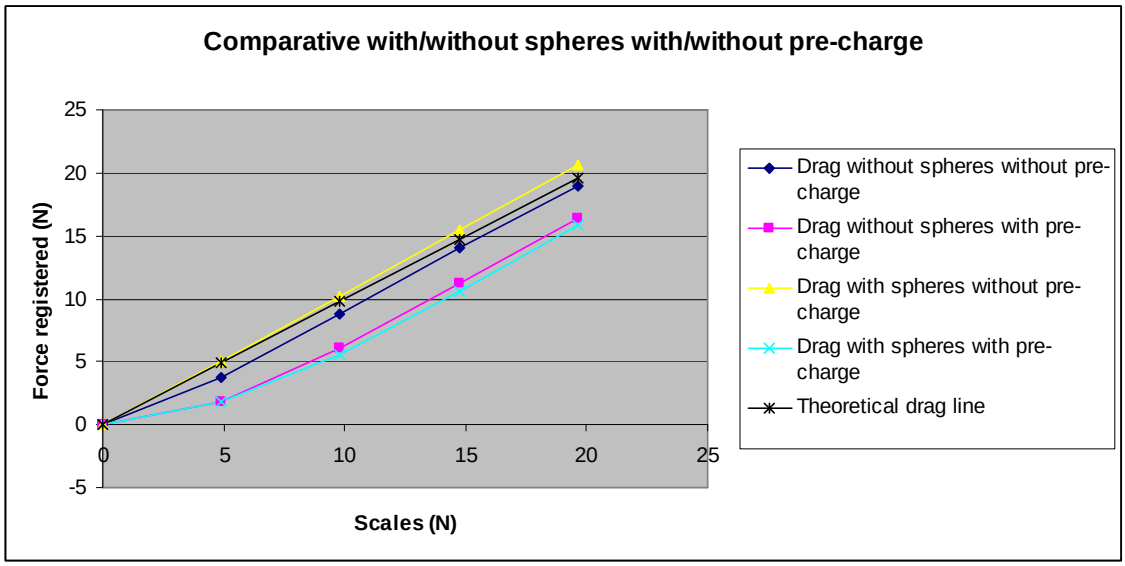

Fig. 3.2.04. Comparative with/without spheres and with/without pre-charge

As in the previous analysis, it can be observed in fig. 3.2.04 that in the case of experiments with pre-charge the cells do not registered the values expected. So, the conclusion is that in wind tunnel the experiment will be performed without pre-charge in order to get measurements as realistic as possible.

Then, in the case of the two experiments without pre-charge (blue and yellow curves) it can be seen that for the first 10 N, the yellow curve follows the theoretical curve better than the blue one, which means that, with low load, the experiment with spheres is more realistic than without spheres. Taking into account that in wind tunnel the experiment will be developed with very low forces, the conclusion is that the second campaign of measurements should be done without pre-charge and with spheres under the moving plate.

EXPERIMENT	MEAN SQUARE DEVIATION
♦ **Drag without spheres and without pre-charge**	0,670718689
▲ **Drag without spheres and with pre-charge**	9,125937473
■ **Drag with spheres and without pre-charge**	0,364444881
x **Drag with spheres and with pre-charge**	11,69062161

Table 3.2.02. Mean square deviation of each experiment.

Finally, the following last experiment has been done, putting over the moving plate a scale of 500 gr., value that is very close to the weight of the motorcycle model whose weight measure in the dynamometric balance is 480 gr. This way the experiment fits better the characteristics of the wind tunnel campaign and the results of the calibration will be more realistic.

Fig. 3.2.05 shows the results obtained with the experiment described above, where it can be seen that, again, the measurement scenario whose results fit better the theoretical drag line is the one with spheres and without pre-charge.

However, it can be observed that using the spheres, the load over the moving plate does not affect the measurements of the cells. With the spheres the behaviour of the cells is very regular. In all the experiments with the spheres the results obtained are very close and in the range of 0-10 N, the results are very close to the theoretical ones.

Due to these reasons, the final decision is to put the spheres under the moving plate.

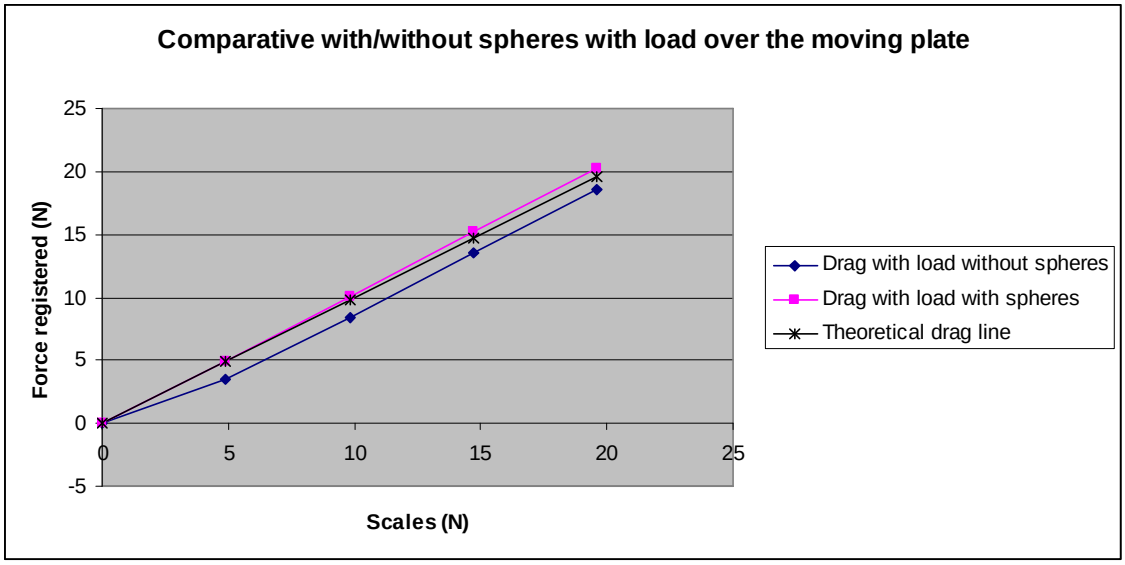

Fig. 3.2.05. Comparative with/without spheres and with load on moving plate

EXPERIMENT	MEAN SQUARE DEVIATION
♦ **Drag with load without spheres**	1,236208313
■ **Drag with load with spheres**	0,158983876

Table 3.2.03. Mean square deviation of each experiment.

To have a global vision of the procedures, the next figure shows the experiments in one graphic, fig. 3.2.06, where it can be noticed that:

1. - In the experiments with pre-charge the cells do not work as it is expected. Thus, in the wind tunnel campaign pre-charge on the cells will not be used. The curves corresponding to these results are the ones represented in pink and cyan.

2. - In the experiment without spheres the cells do not work as expected even if the results obtained are closer to the theoretical ones than in the previous experiment. The curves corresponding to these results are the ones represented in brown and purple.

3. - In the experiments with spheres and without pre-charge, with or without load, the cells give results that are very close to the theoretical drag line. Thus, the best solution is the scenario with spheres and without pre-charge. The curves corresponding to these results are the ones represented in yellow and blue.

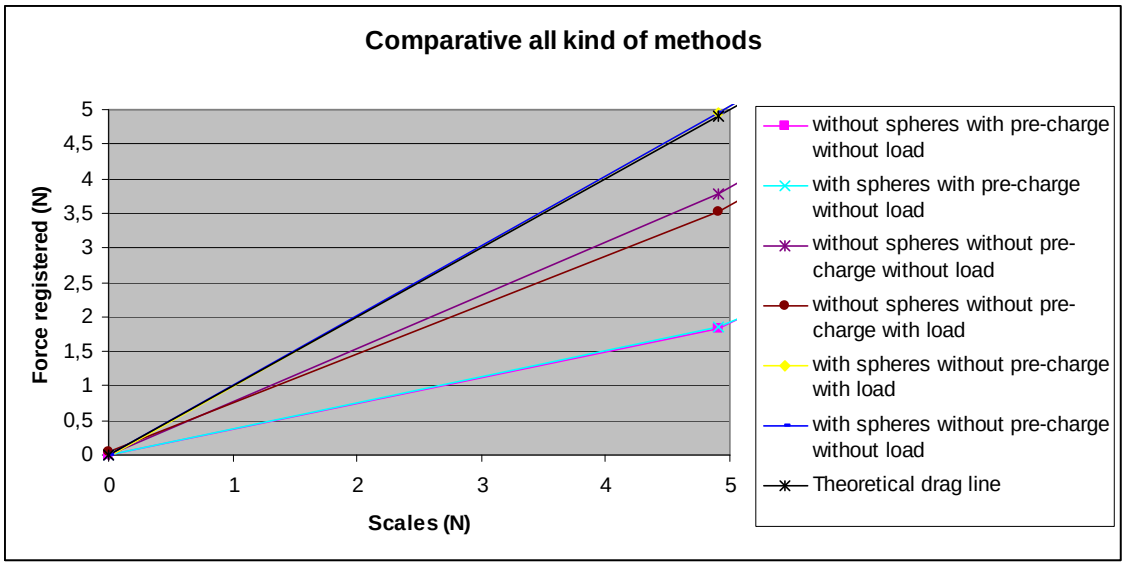

Fig. 3.2.06. Comparative all methods. With/without spheres, with/without pre-charge and with/without load on moving plate

Not only improves the measures on the drag cells. The measures on the lateral force are better. As it is said before, the lateral cell Ys is broken, and it has been measured only with the spheres, but in the fig. 3.2.07 it can be observed that the measures on the Yd cell with spheres are closer to the theoretical line than without the spheres.

In the case of the Ys cell, as it is said before, it has been calibrated after the wind tunnel experiment and only the values with spheres have been obtained. These values can be observed in the section 3.3.3.

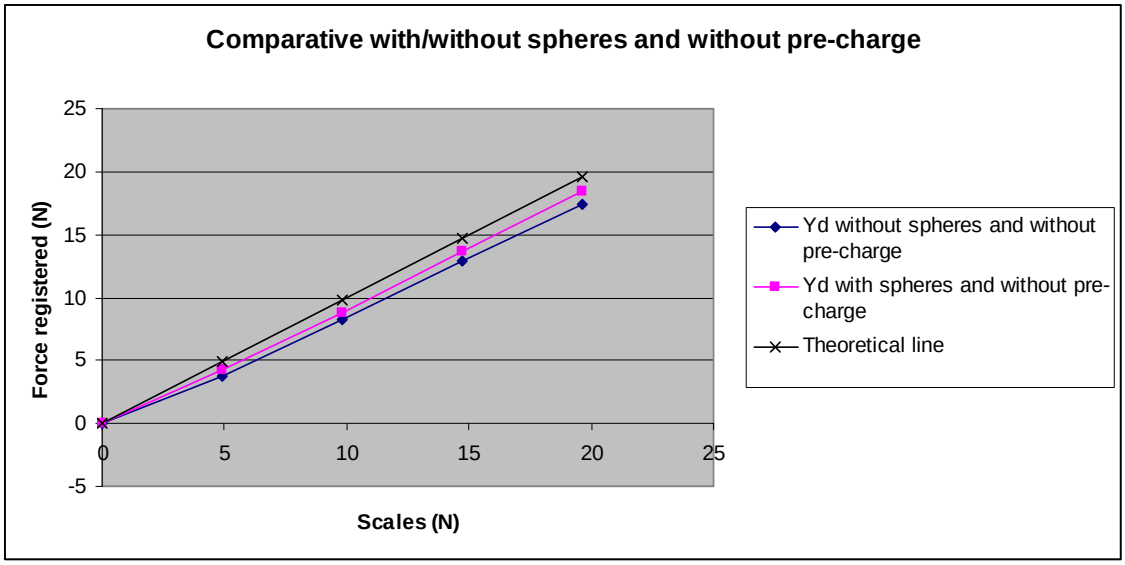

Fig. 3.2.07. Comparative with/without spheres and without pre-charge.

EXPERIMENT	MEAN SQUARE DEVIATION
♦ **Yd without spheres and without pre-charge**	2,333900121
■ **Yd with spheres and without pre-charge**	0,773196784

Table 3.2.04. Mean square deviation of each experiment.

But when the spheres are under the moving plate, the lift cells do not measure anything, because the moving plate does not touch these cells. This is why it is necessary to do two campaigns of measures.

3.3 FINAL CALIBRATION RESULTS.

3.3.1 Lift cells calibration: Fd, Fs, Ad, As

As it is said at the beginning of chapter, the first step is to put at the same height all the cells in order to distribute the weight as much as possible. In this way it will not be any pitching or rolling moment and the experimental measures will give more realistic results.

In the first measurements not all the cells were at the same height and the drag registered was not the expected because of the friction. Afterwards, they have been pre-charged at the same height, and although we still have problems with friction, the measures were closer to the theoretical results.

Figures 3.3.01 to 3.3.04 show the line calibration of each cell. The constants found by engineer Marco Nunez have been used in this calibration experiment. The different constants can be seen in the line calibration, where they are represented with the slope of the black lines.

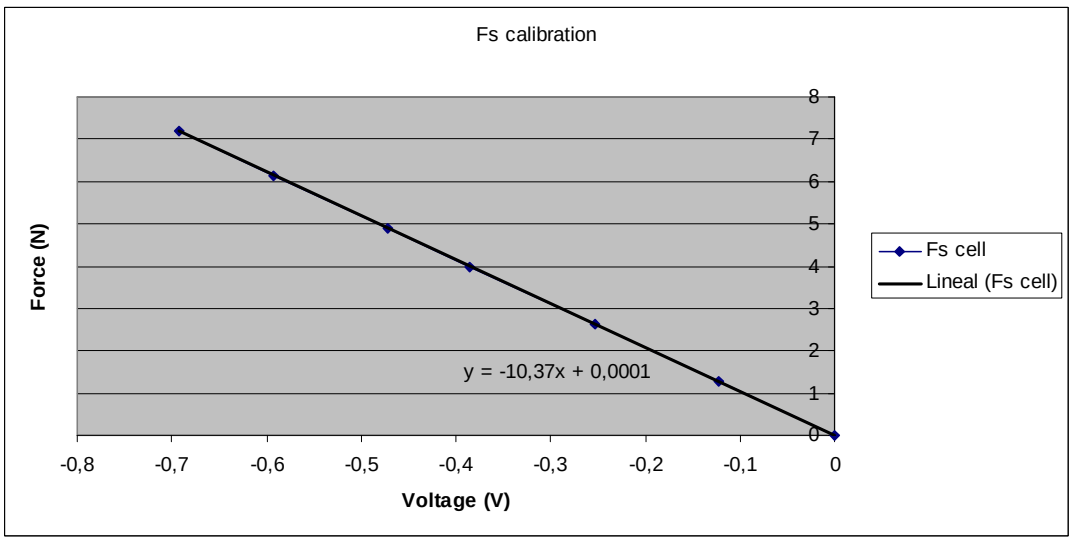

Fig. 3.3.01. Fs cell calibration.

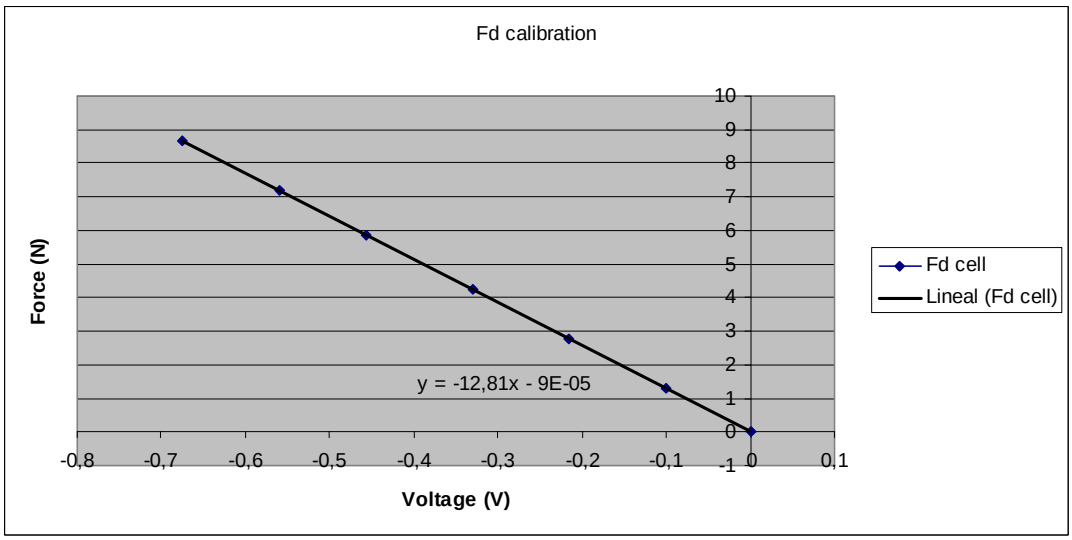

Fig. 3.3.02. Fd cell calibration.

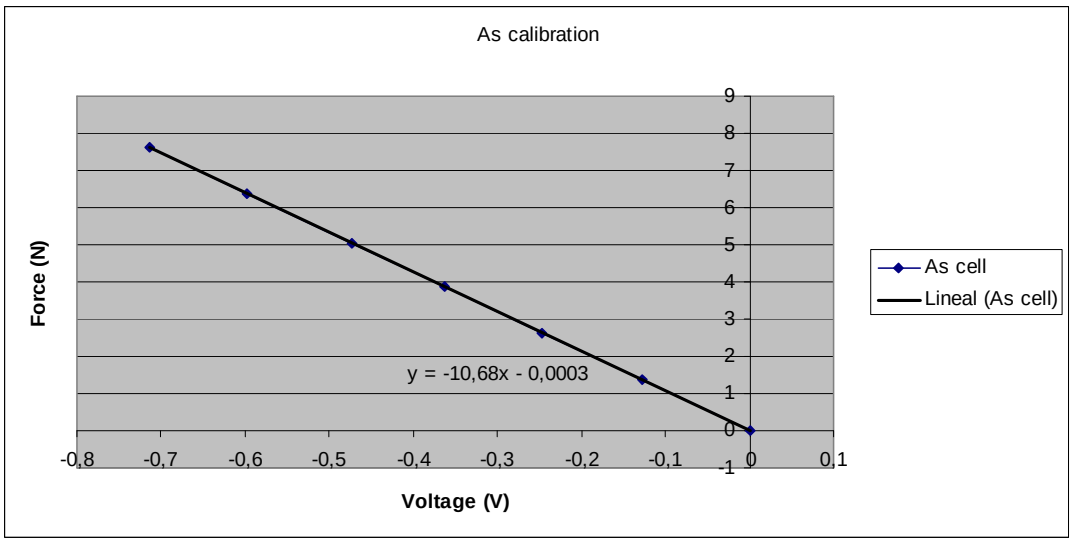

Fig. 3.3.03. As cell calibration.

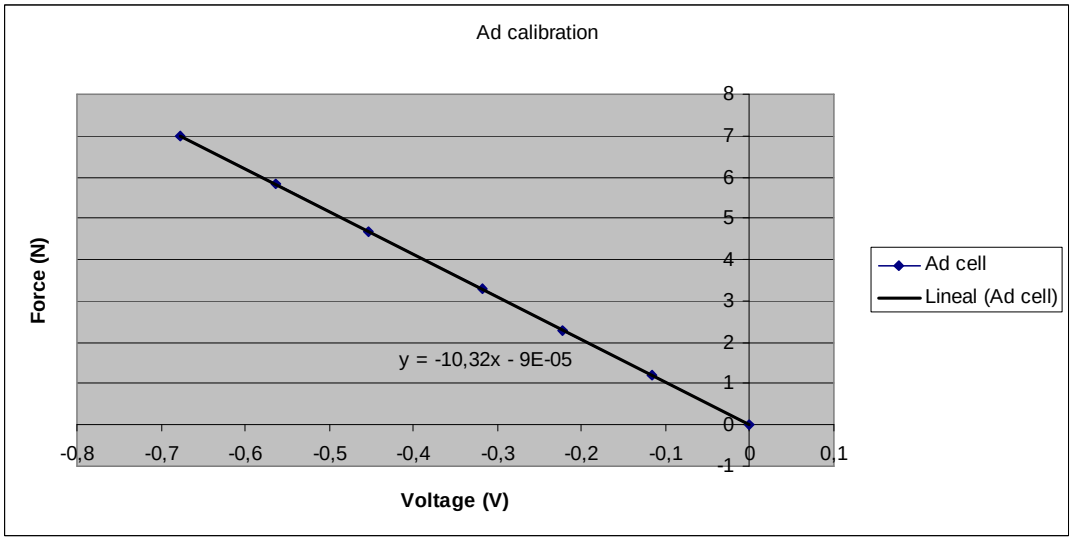

Fig. 3.3.04. Ad cell calibration.

Table 3.3.01 shows values of the voltage of each cell with the different reference weights used in the calibration experiments. It can be observed that it has been tried to pre-charge at the same voltage. As it has been said before, if the cells are not pre-charged at the same voltage, there may be problems with the calculation of the moments.

Load over moving plate (N)	**Load over moving plate (kg)**	**Fs (V)**	**Fd (V)**	**As (V)**	**Ad (V)**
0	**0**	-0,00011524	5,8317E-05	0,0001024	3,7097E-05
4,9	**0,5**	-0,12186133	-0,10099867	-0,127534	-0,11665867
9,8	**1**	-0,25346733	-0,21637067	-0,246842	-0,22205067
14,7	**1,5**	-0,385666	-0,33034	-0,363507	-0,318166
19,6	**2**	-0,471965	-0,45569033	-0,472243	-0,453331
24,5	**2,5**	-0,592082	-0,55973533	-0,59867067	-0,564279
29,4	**3**	-0,69240467	-0,67537733	-0,71355533	-0,677438

Table 3.3.01. Voltage of each cell in the calibration experiment

Table 3.3.02 shows the different values of forces registered in each cell. Here it is easier to see the objective of distributing the loads the better way as possible.

Load in each cell (N)	**Load in each cell (kg)**	**Fs (N)**	**Fd (N)**	**As (N)**	**Ad (N)**
0	**0**	0,00136956	-0,00064492	-0,00118699	-0,00059359
1,225	**0,5/4 = 0,125**	1,26377333	1,29370667	1,36158333	1,20389333
2,45	**1/4 = 0,25**	2,62834333	2,77117333	2,6359	2,29138667
3,675	**1,5/4 = 0,375**	3,99945	4,23163	3,88189667	3,28349667
4,9	**2/4 = 0,5**	4,89432	5,83800333	5,04357333	4,67859
6,125	**2,5/4 = 0,625**	6,14024667	7,17052333	6,39346	5,82360667
7,35	**3/4 = 0,75**	7,17979333	8,65135333	7,62072	6,99081333

Table 3.3.02. Force registered of each cell in the calibration experiment

Fig. 3.3.05 represents the evolution of the force registered by each cell with the reference weights used in the experiment and the theoretical line. All the lines should be similar to the theoretical curve, but the dynamometric balance is very accurate, and it is very difficult to obtain this behaviour.

It can be noticed that the Fd cell gives higher results than the theoretical line, but the other three are quite close to the expected results.

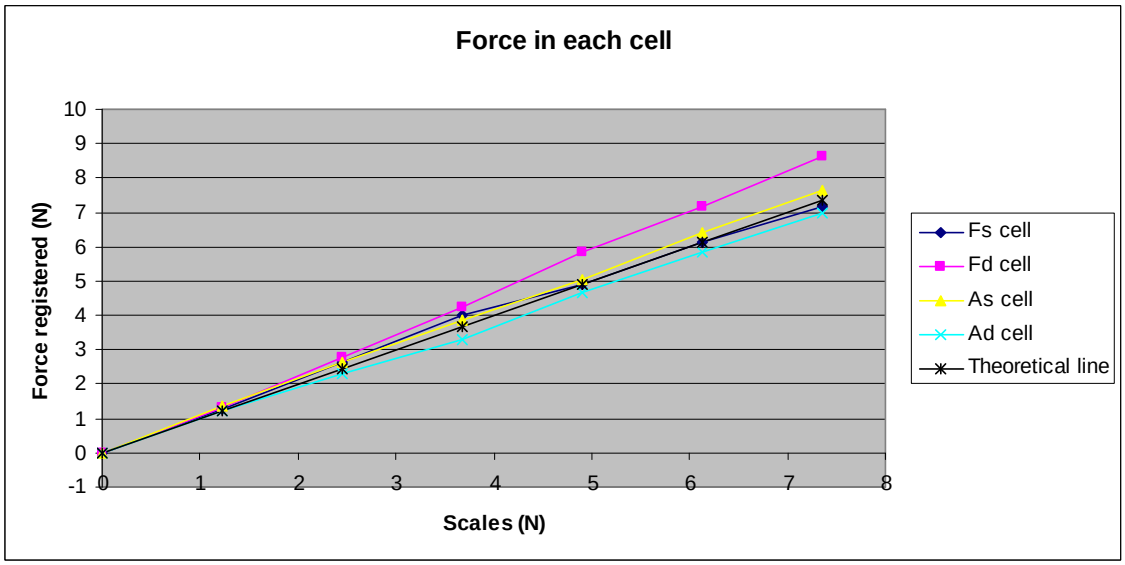

Fig. 3.3.05. Force in each cell

Fig. 3.3.06 shows that the lift line is very similar to the theoretical lift line. Also all other forces and moments are represented in order to see that are insignificants.

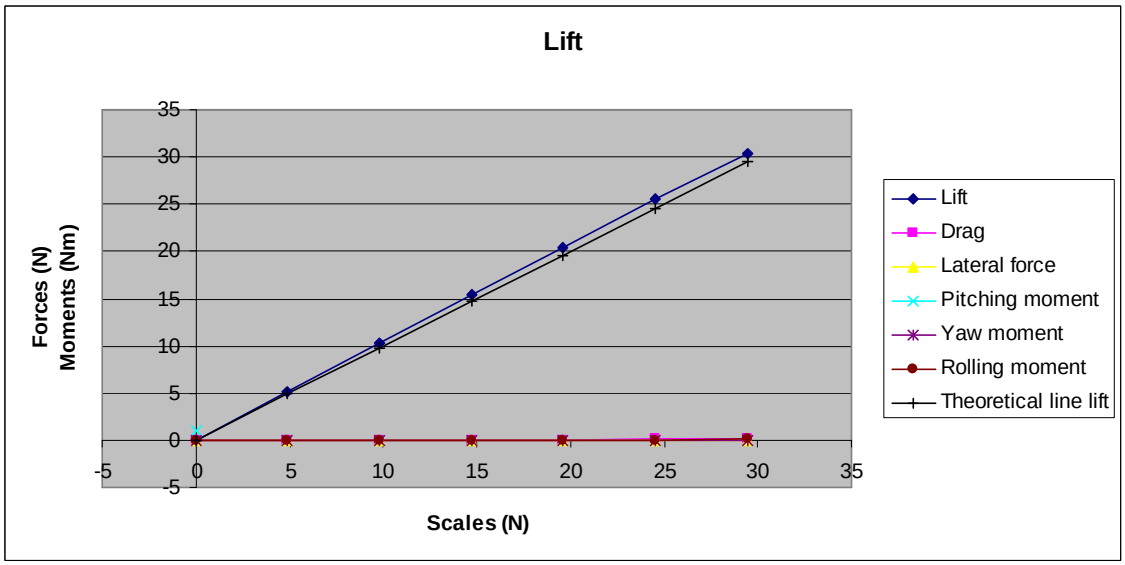

Fig. 3.3.06. Evolution of the lift registered

3.3.2 Drag cells calibration: Ds, Dd

In the chapter “Solutions to minimize friction of moving plate” all the experiments have been analyzed. The conclusion is that the best experiment is the one measured with spheres and without pre-charge. Consequently, this is the way chosen for the experiments in wind tunnel.

Now, the final calibration results of each cell in the case of using spheres and without pre-charge are shown.

It has been observed that the cell Ds register more force than the other drag cell Dd. This factor must be considered when the wind tunnel results are analyzed. This difference must be minimized because of the error introduced when measuring the yawing moment. This difference can not be minimized using the “pre-charge” mode because these cells do not work as they were expected.

Following tables and figures will show this difference and also will show the fact that data of Ds cell are over the average while data of Dd are below it. Anyway, the couple of cells measures very close to the theoretical drag line.

Reference weights (kg)	Ds (V)	Dd (V)
0	0,00373879	0,00050337
0,5	-0,57635033	-0,370149
1	-1,17321667	-0,75471667
1,5	-1,76970667	-1,13475333
2	-2,35616333	-1,51468333

Table3.3.03. Voltage in each drag cell

Table 3.3.04 shows the values of forces registered by each cell. Here can be noticed the difference before commented.

Reference weights (kg)	Reference weights (N)	Ds (N)	Dd (N)
0	**0**	-0,02132983	-0,0025682
0,25	**2,45**	3,01506	1,94563333
0,5	**4,9**	6,13756333	3,96673
0,75	**7,35**	9,25867667	5,96435333
1	**9,8**	12,3269667	7,96129

Table3.3.04. Force registered in each cell

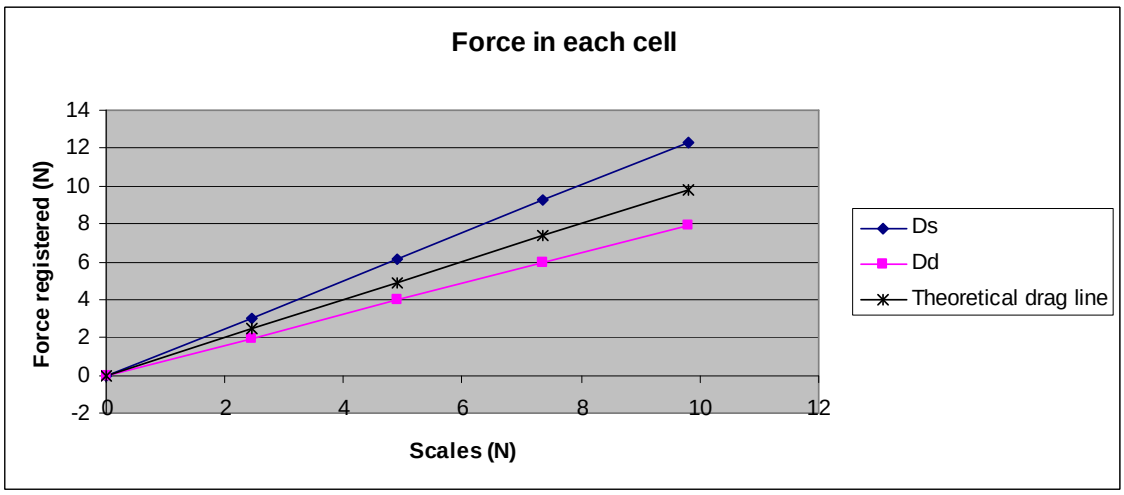

Fig. 3.3.07. Force registered in each cell

In the lines interpolated from the calibration experiments, the calibration constants are observed, since they correspond to the slope of the black line. They are very close to the theoretical constants found by engineer Marco Nunez. These constants have been used in the experiments of this thesis.

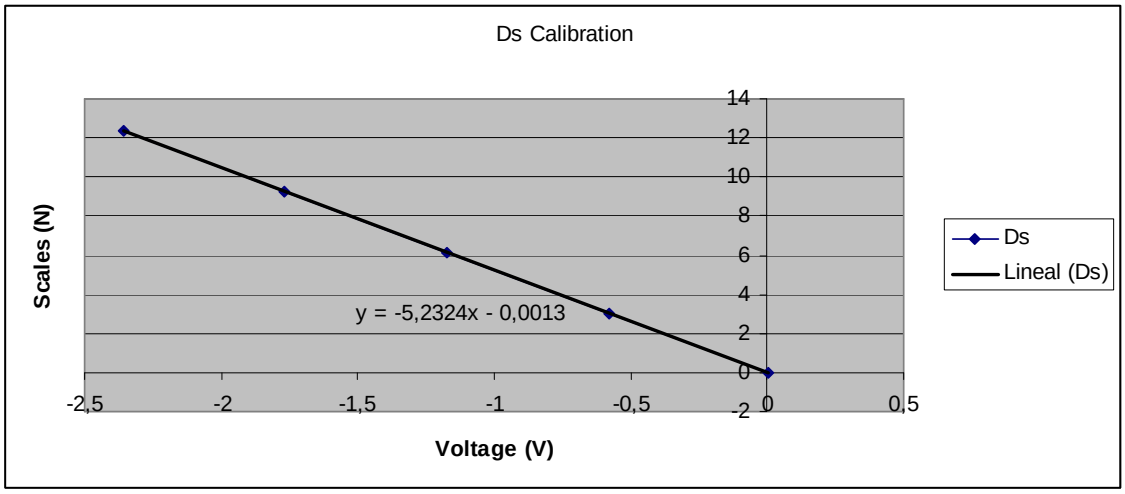

Fig. 3.3.08. Ds cell calibration

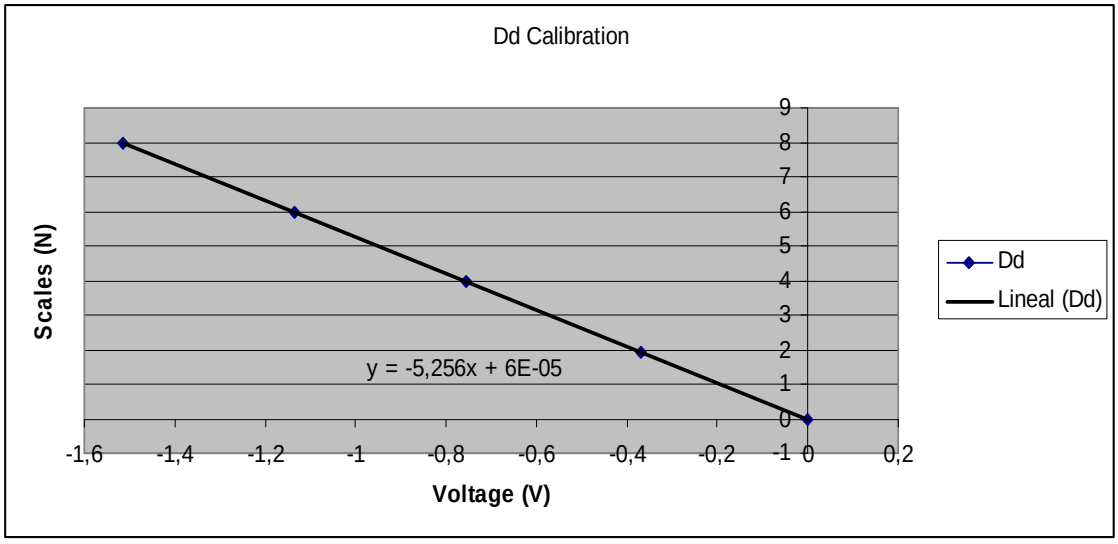

Fig. 3.3.09. Dd cell calibration

	Ds	Dd
Marco Nunez constants	-5,232	-5,256
Experimental calibration constants	-5,2324	-5,256

Table. 3.3.05. Conversion constants found by engineer Marco Nunez [18]

Table 3.3.06 and Fig. 3.3.10, show that the addition of the values of both cells is very close to the theoretical values of the reference weights used in the calibration experiment.

Force registered (N)	Reference weights (N)
-0,023898	0
4,96069667	4,905
10,1043	9,81
15,2230333	14,715
20,2882333	19,62

Table 3.3.06. Force registered and the theoretical results

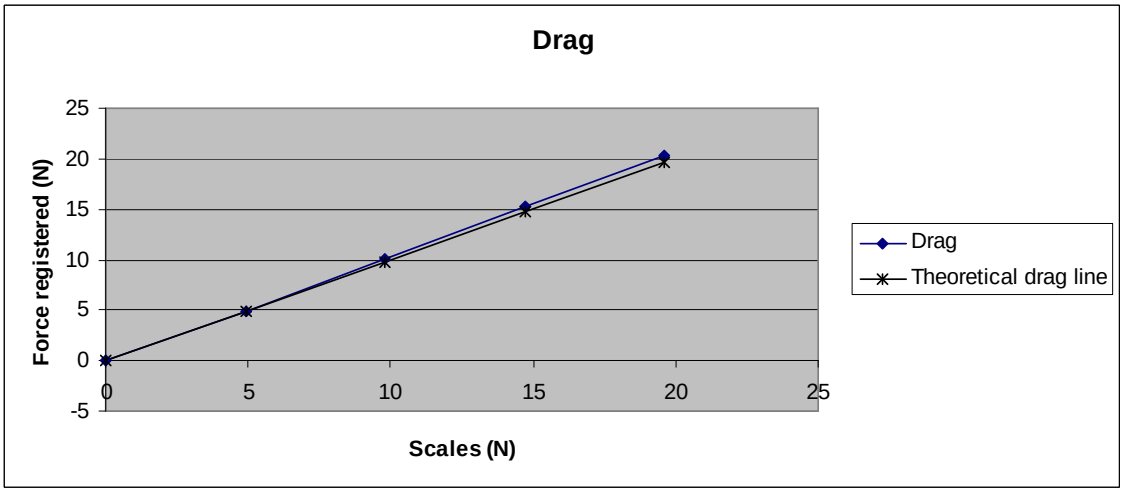

Fig. 3.3.10. Evolution of the drag registered

CONCLUSION: The results of the drag registered are reliable, but because of the difference between the measures of the cells Ds and Dd, an error calculation in the yawing moment must be considered when analyzing the results.

3.3.3 Lateral cells calibration: Ys, Yd

In the lateral cells calibration, Ys and Yd, the procedure have been the same used in the calibration of drag cells, with spheres and without pre-charge, and using the pulley and using scales up to 2 kg.

The cell Ys is broken, so the procedure has been to change it with the cell Fd in order to measure all the components of the perimeter cells (drag, lateral force and yawing moment) in the second campaign with the spheres. This is because in this campaign, the cells Fs, Fd, As and Ad do not measure anything because the moving plate is on the spheres and do not touch these cells.

Thus, the change of the cells Fd and Ys in the dynamometric balance and in the acquisition system is enough to measure all the lateral forces in the model.

The problem is that calibration of the Ys cell has been done after the wind tunnel campaign, and it has been observed in this experiment that the cell does not work as it was expected in the same conditions as the calibration of the other cells.

It is also important to notice that the calibration has not been done at the same time, since the cell Ys has been calibrated in a first experiment and the cell Yd has been calibrated in another different experiment.

Voltage (V)	Force registered (N)
0,00222545	-0,03510737
-0,26783633	4,24016667
-0,55569767	8,79725667
-0,86713033	13,7268333
-1,16416333	18,4281

Table 3.3.07. Voltage and force registered in Yd cell

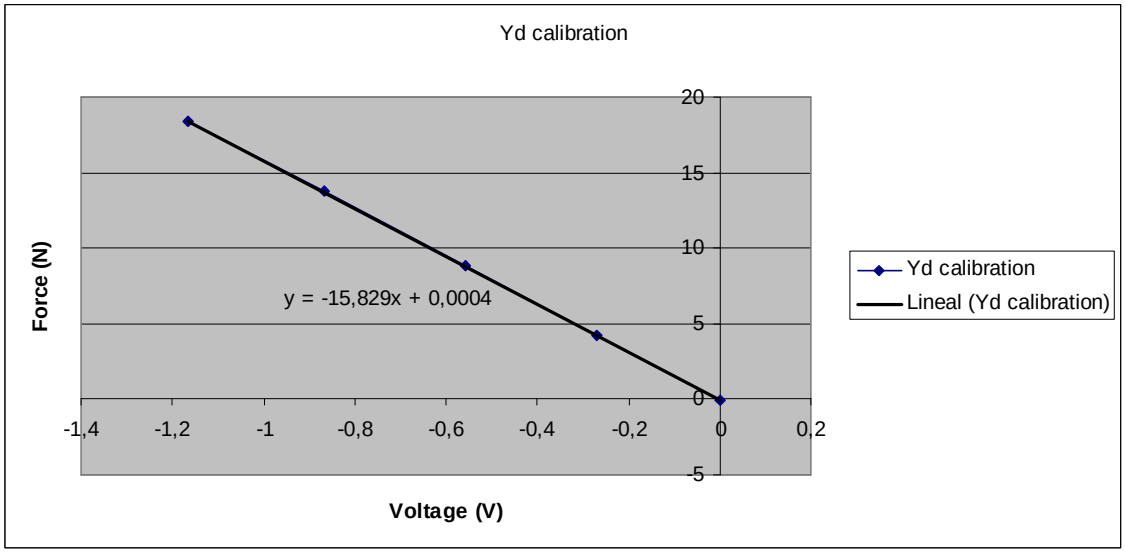

Fig. 3.3.11. Yd cell calibration

Fig 3.3.12 shows that the line calibration is close to the theoretical curve, but not as close as in the other experiments in which the line calibration was similar to the theoretical in the range of 0-5 N.

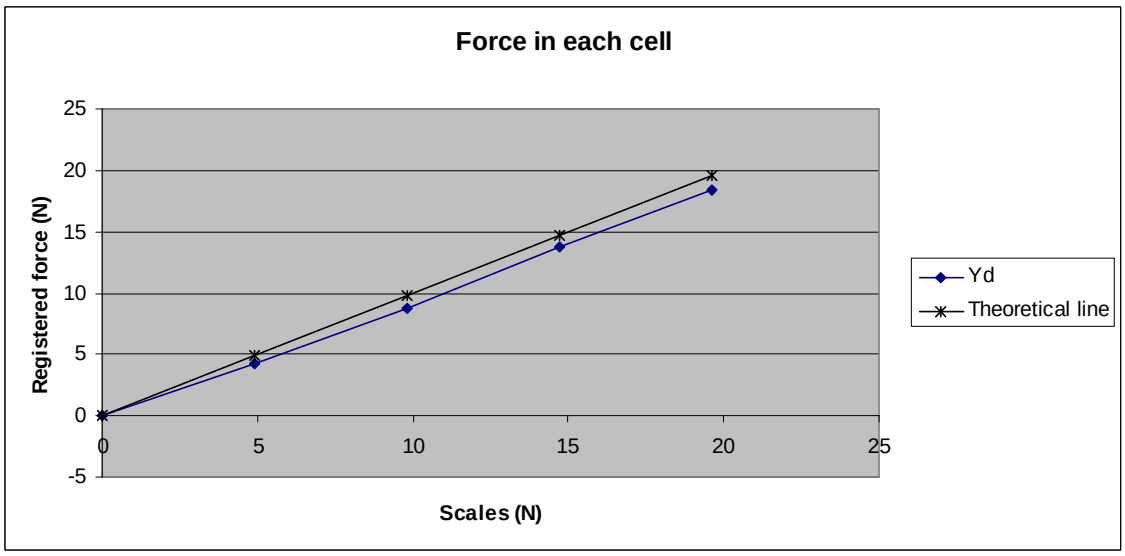

Fig 3.3.12. Evolution of the lateral force of Yd cell registered

As it is said before, the calibration of the Ys cell has been done after doing the wind tunnel campaign. It can be noticed in table 3.3.09 and fig. 3.3.12 that this cell does not measure as the expected. This result must be considered when lateral force results are analyzed. In fact, it has been thought to multiply by a constant using the calibration line represented in fig. 3.3.13 in order to know the corresponding theoretical value of the error values registered.

This way, it is possible to analyze if the wind tunnel results with positive angles are similar to the ones with negative angles, because the Ys and Yd measures do not introduce any error in any other measure. Thus, the comparison of the lateral aerodynamic coefficient in positive and negative degrees can be performed.

Voltage (V)	Force registered (N)
-0,00092823	0,00534445
-0,0951015	0,53948733
-0,20221933	1,14719667
-0,312628	1,77310333
-0,422119	2,39416333

Table 3.3.08. Voltage and force registered in Ys cell

Force registered (N)	Reference weights (N)
0,00534445	0
0,53948733	4,9
1,14719667	9,8
1,77310333	14,7
2,39416333	19,6

Table 3.3.09. Force registered vs. Reference weights

Fig. 3.3.13 shows the values of the lateral force registered during the calibration of the Ys cell. Here it can be observed that the Ys cell do not registered as the expected, may be because, as it has been said before, the cell Ys has been changed with the Fd cell.

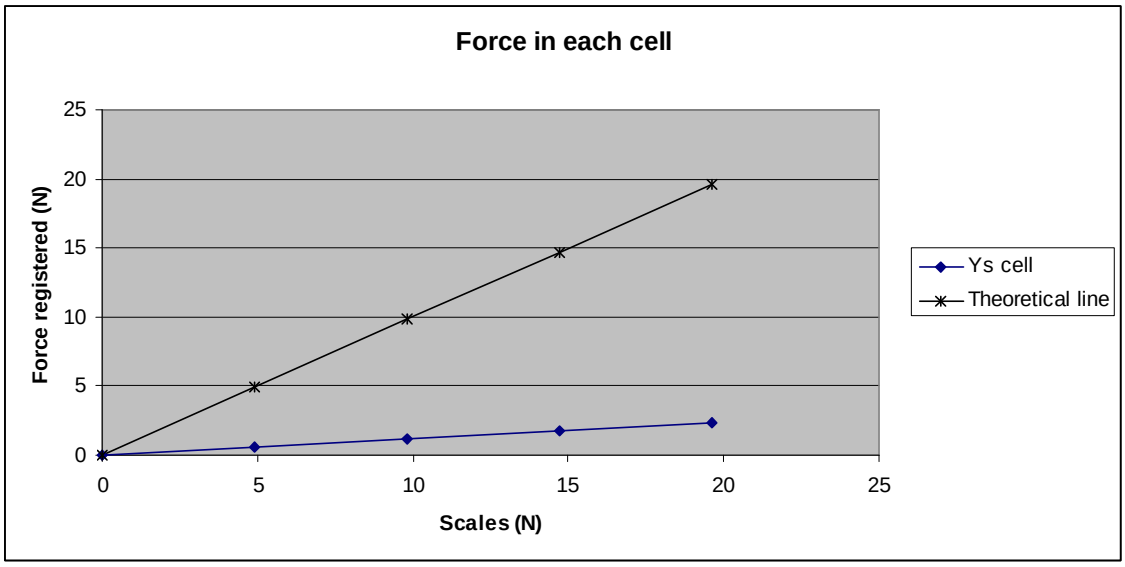

Fig 3.3.13. Evolution of the lateral force of Ys cell registered

The mean square deviation is 111,6648058, which indicates that the measurements are very different of the theoretical line.

CHAPTER 4

EXPERIMENTAL RESULTS

4.1 FORCE AND FORCE COEFFICIENT MEASURED

This chapter performs an analysis of the experimental results obtained from the measurement campaigns developed on the wind tunnel.

As it is explained in chapter 2, the experiments on the wind tunnel have been divided in two different campaigns. First, one campaign in which the experiments have been performed without the spheres under the moving plate, in which the lift force and the pitching and rolling moments have been measured, and the second one, putting the spheres under the moving plate, in which the drag and lateral forces and the yawing moment have been measured.

The measurements have been done using different yawing angles, between -30º to +30º every 10º, taking special attention to the zero angle measures.

Also it is important to have in mind that there were some problems with the belt system because of the motor's overheating. Thus, only one experiment was carried out with

the belt system with a speed of wind of 10 m/s. This is the reason why it is difficult to obtain any conclusion of the differences between the experiments with and without the belt system.

Notice that, in order to compare the experimental values on the model scale with the real values in the large scale, a dimensional analysis is needed in order to observe the relation between the variables that come into play in the measurements performed.

Therefore, a geometrical relation between the dimensions on the model and the large scale must be derived. Moreover, it must exist a dynamical similarity between both systems. When flow's incompressibility conditions are present, this similarity between the large scale and the motorcycle model used in the experiments is determined by the similarity between the large scale's Reynolds number and the model's Reynolds number. The Reynolds number is defined as:

$$Re = \frac{U \cdot L}{\upsilon}$$

where U is the speed of wind of the experiment, L the model's characteristic length and υ is the the cinematic viscosity of the fluid (1.43 E-05 m^2/s for air).

The motorcycle model used in the experiment is in a 1:12 scale. To get a similarity between the forces on the large and the small scales, the speed of wind on the experiments must be twelve times higher than on the small scale.

In the wind tunnel of the La Sapienza University of Rome this similarity cannot be satisfied because the maximum speed of wind of the wind tunnel is 45 m/s. To get this similarity, it is necessary to achieve a speed of wind of 1000 m/s. Moreover, at this high speed of wind, incompressibility conditions of the fluid would not be present (all this under the supposition that the Yamaha YZR M1 which is the motorcycle model of the experiments, can run up to 320 km/h in the large scale case [21]).

This is why the similarity between the large scale and the small scale motorcycles must be studied from the analysis of the normalised aerodynamic coefficients.

4.1.1 Lift

For the calculation of the lift coefficient, the following formula will be used:

$$C_L = \frac{-L}{\frac{1}{2}\rho U^2 S_{pl}}$$

where:

- ρ represents the density of the air (1.167 kg/m^3 at atmospheric pressure 987 bar and 20ºC temperature).
- S_{pl} represents the frontal area.
- U represents the wind speed of the experiment.
- L is the lift force.

Fig 4.1.01 shows the behaviour of the lift coefficient with the Reynolds number. The lift coefficient should be symmetrical to the zero angle but as it can be observed in this figure this behaviour is not observed in the experimental results. This lift coefficient should be symmetrical as all the other coefficients should be symmetrical with respect to the longitudinal axis. Some deviation can appear in the symmetry due to the existence of the exhaust pipe.

This symmetry would be represented in the figure by similar curves corresponding to the positive and negative angle of the same absolute value. That means, the -30º and the +30º curves must be similar, and it should occur the same in the cases of +/- 20º and +/- 10º (the following couples of lines should be similar: blue – green, pink – brown and yellow – purple).

As it can be observed, this symmetry condition does not exist in the experiment. This could be due to some assembly errors or due to the presence of the exhaust pipe, which provokes an asymmetry on the motorcycle with respect to the longitudinal axis.

Table 4.1.01 shows that 8 measurements have been performed from 0 to 900 rpm every 100 revolutions of the fan of the wind tunnel. This corresponds to the speeds of wind of this table

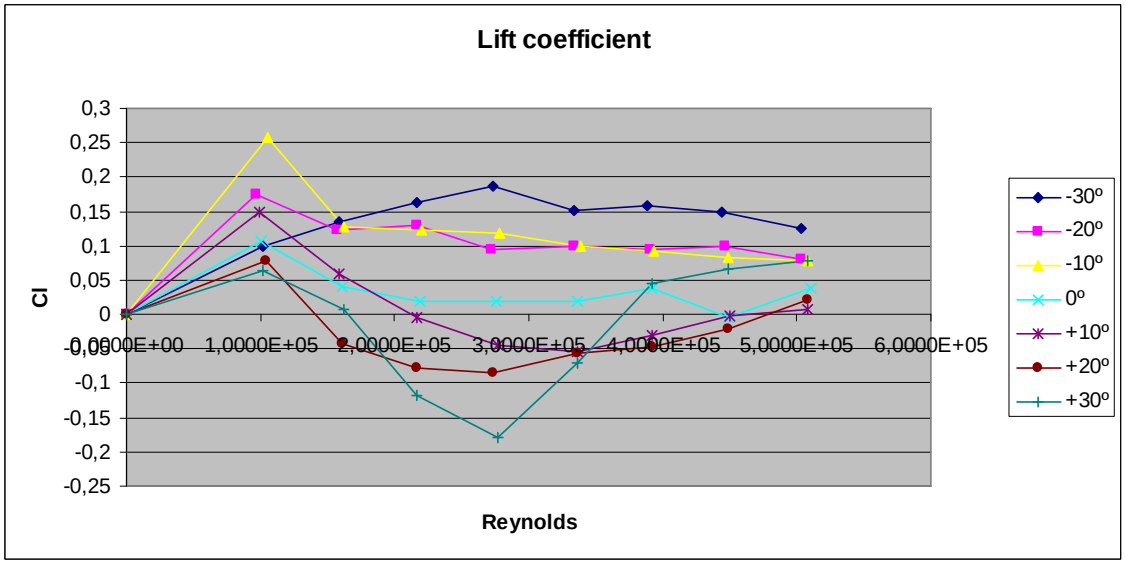

Fig. 4.1.01. Lift coefficient at different yawing angles vs. Reynolds number.

Table 4.1.01 shows the distribution of the load in each cell in the zero angle case. In this table it can be observed that the behaviour of the lift force is decreasing but in the penultimate measure this behaviour is disturbed, may be for the high wind speed which can provoke a movement of the model.

Fig. 4.1.02 shows the evolution of the measures of each cell increasing the speed of wind. It can be observed that the evolution is regular up to 25 m/s. Also it can be observed that the front cells, Fs and Fd, tend to unload while the rear cells, As and Ad, tend to overload. Moreover, the differences between these loads provokes the increasing of the pitching moment but the lift is slight constant increasing the Reynolds number, so the download in the front cells is compensated for the overload in the rear cells.

Speed of wind (m/s)	Reynolds	Lift (N)	Fs (N)	Fd (N)	As (N)	Ad (N)	Cl (neg)
0	0,0000E+00	0,00810551	-0,00290664	0,0136531	7,25E-04	-0,00336586	0
6,2	1,0039E+05	-0,031435	-0,0398371	-0,0322445	0,0289202	0,0117263	0,10618943
9,9	1,6030E+05	-0,0298239	-0,0930027	-0,0567738	0,0797968	0,0401557	0,03951348
13,5	2,1859E+05	-0,0280456	-0,166951	-0,101205	0,147462	0,0926482	0,01998243
17	2,7526E+05	-0,0422745	-0,249197	-0,206948	0,233818	0,180052	0,01899467
20,8	3,3679E+05	-0,0669823	-0,402358	-0,331814	0,32914	0,338049	0,0201041
24,2	3,9184E+05	-0,170339	-0,564775	-0,509231	0,388704	0,514964	0,03776892
27,7	4,4851E+05	0,0251977	-0,495427	-0,697848	0,349545	0,868928	-0,00426435
31,5	5,1004E+05	-0,293213	-0,351612	-1,53989	0,26473	1,33356	0,0383719

Table 4.1.01. Lift data at zero yaw angle.

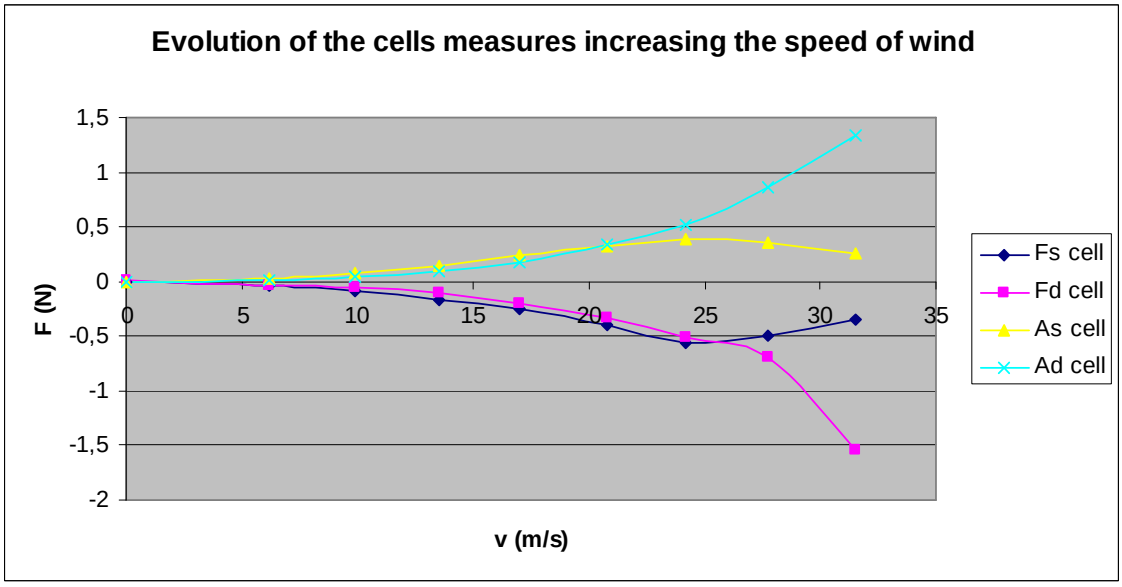

Fig. 4.1.02. Evolution of the cells measures increasing the speed of wind.

4.1.2 Drag

The drag coefficient is calculated with the following formula:

$$C_D = \frac{D}{\frac{1}{2}\rho U^2 S_{fr}}$$

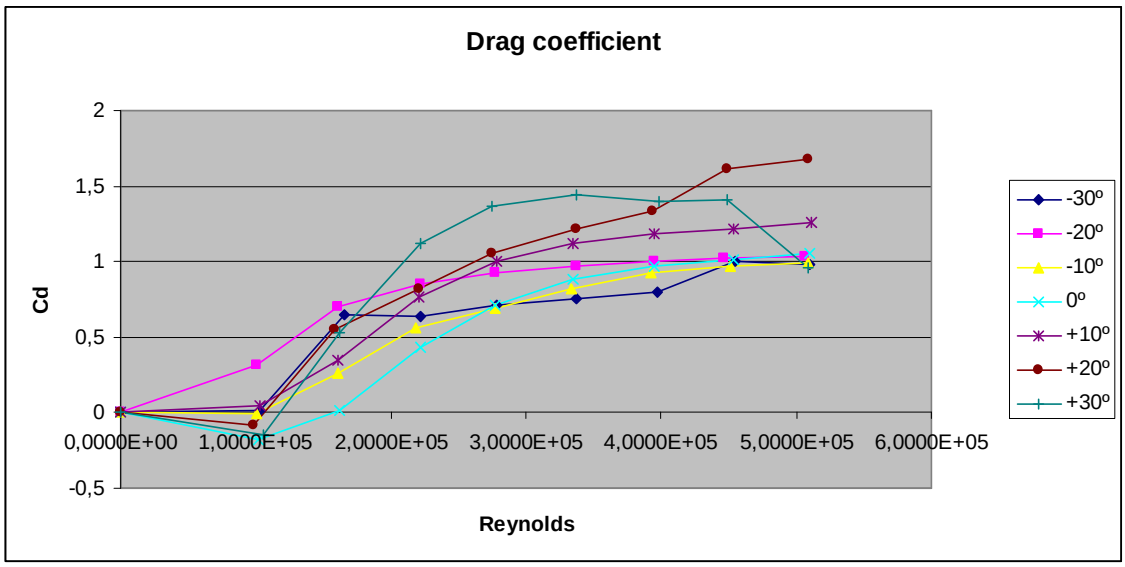

Fig. 4.1.03. Drag coefficient at different yawing angles vs. Reynolds number.

As in the case of the lift coefficient, the drag coefficient must be similar for yawing angles of the same absolute value. As in the other case, the blue and green lines should coincide (for a yawing angle of -/+30º respectively). The same for the pink and brown lines (-/+20º) and for the yellow and purple lines (-/+10º).

In this case this behaviour is not achieved exactly, as it can be observed in fig 4.1.03, where the drag coefficient for each yawing angle increasing the Reynolds number is shown. Nevertheless, this figure shows that for the zero angle, represented by the cyan line, the motorcycle model has the lower drag coefficient, as it was expected.

This figure also shows the increasing tendency of the drag coefficient with the Reynolds number. In fact, this evolution tends to a horizontal asymptote. This behaviour fits the expectations because the drag coefficient depends inversely on the square of the speed of wind and directly on the drag, and as shows fig. 4.1.04 the drag increases with the Reynolds number as a parabola, it means, depending also on the square of the speed of wind.

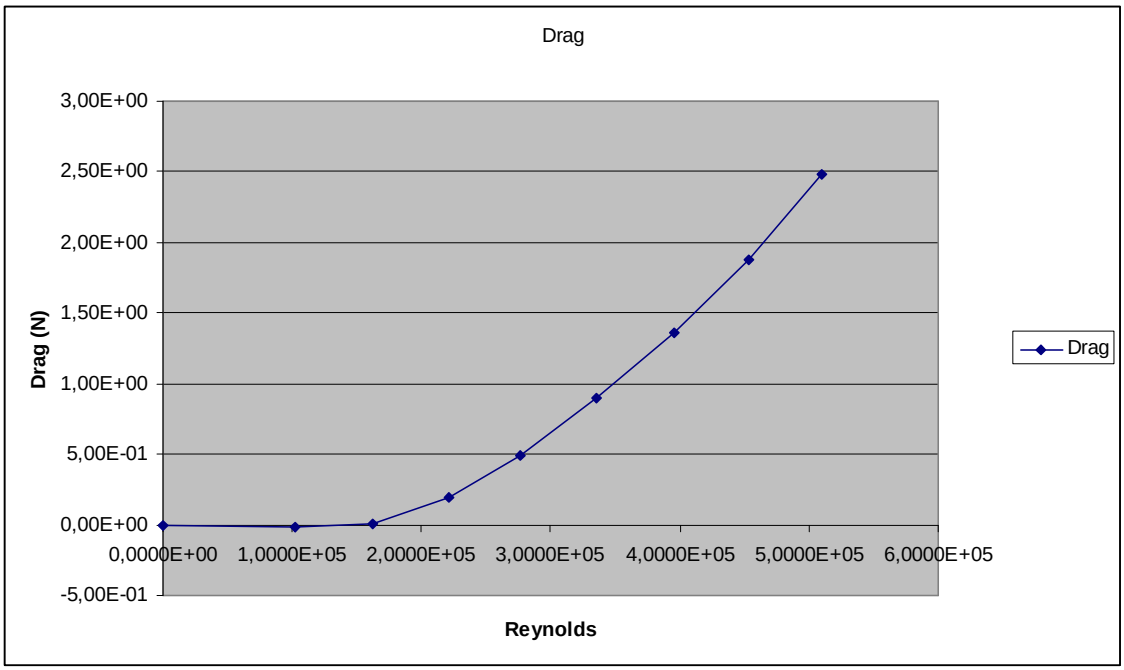

Fig. 4.1.04. Evolution of the drag with the Reynolds number.

Speed of wind (m/s)	Reynolds	Drag (N)	Ds (N)	Dd (N)	Cd
0	0,0000E+00	-1,02E-02	-2,35E-03	-0,00781539	0
6,3	1,0201E+05	-0,0170238	-5,57E-03	-1,15E-02	-0,1817169
10	1,6192E+05	0,00400922	-0,00608986	0,0100991	0,01698556
13,7	2,2183E+05	0,194034	0,0973873	0,0966469	0,43798236
17,1	2,7688E+05	4,92E-01	0,293876	0,19858	0,71350189
20,7	3,3517E+05	0,896029	0,530312	0,365717	0,88593384
24,4	3,9508E+05	1,36004	0,814479	0,54556	0,96781409
28	4,5337E+05	1,87589	1,11904	0,756848	1,01370414
31,5	5,1004E+05	2,4791	1,47026	1,00884	1,05850485

Table 4.1.02. Drag data at zero angle.

The drag coefficient obtained is quite high compared with the drag coefficients of table 1.3.01 in chapter 1 found in the literature, between 0.6 and 0.8.

In order to know if the fixation squares disturbs the evaluation of the drag coefficient, a comparison has been performed between the drag coefficients obtained at zero angle with the front area of the motorcycle taking into account the fixation squares, and the front area of the motorcycle neglecting the effect of the area of the fixation squares.

Front area without the fixation squares: 0.003838 m^2.

Front area with the fixation squares: 0.005079 m^2.

In this way, the drag coefficients measured are:

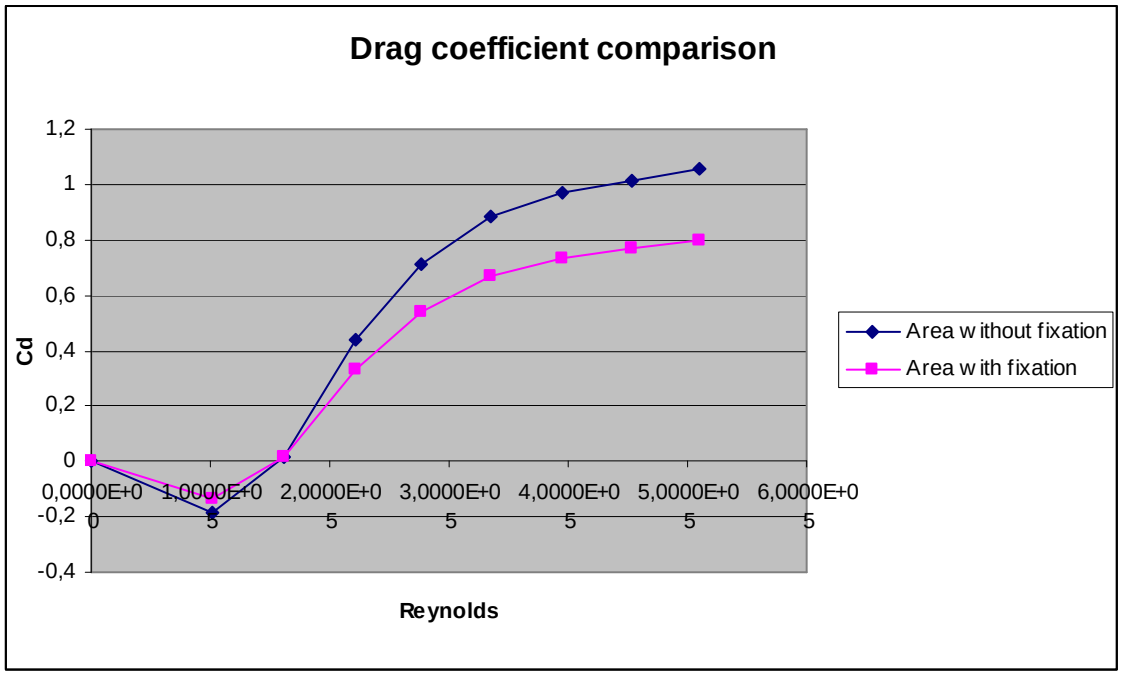

Fig. 4.1.05. Comparison of the drag coefficient with/without the fixation area.

Fig. 4.1.05 shows that the value of the drag coefficient taking into account the area of the fixation is 0.8, which is more similar to the drag coefficients found in the literature. In this analysis, all the area, including the fixation, has been supposed to be influenced by the wind of the experiment. Thus, the drag force corresponding to the motorcycle model area without the fixation will be lower and therefore the drag coefficient will be lower too.

For the different yawing angles the drag coefficient has been calculated by two different modes. First doing the calculus with the frontal area as a constant with a value of 0.003838 m^2 and second calculating the area in the wind direction (S_D) with the next formula:

$$S_D = S_{fr} \cdot \cos\beta + S_{lat} \cdot \sin\beta \qquad (4.1)$$

where S_{fr} is 0.003838 m^2 and S_{lat} is 0.033492 m^2 and β is the yawing angle of each experiment.

The results of the calculation of the drag coefficient with both methods, the frontal area and the area calculated with the formula (4.1), are shown in the tables 4.1.03 to 4.1.05 and in figs. 4.1.06 to 4.1.08. In this graphics, "constant area" refers to the first method with the frontal area as a constant, and "variable area" refers to the second method with the frontal area depending on the yawing angle of the experiment.

As it has explained before, the behaviour of the drag should be symmetrical, so in the next tables and figures the analysis will consist on calculus for yawing angles of the same absolute value. As in the other cases, it will be analyzed the behaviour of the drag coefficient increasing the Reynolds number.

In these figures it can be noticed that the drag coefficient values obtained with the second method of calculus of the area are lower. This is due to the fact that the coefficient depends inversely on the area and this area is bigger in the second method than in the first one.

Moreover, a very important conclusion is that a bigger drag coefficient in the case of positive yawing angles than in negative angles can be observed. This behaviour can be explained by the fact that, as shows fig. 3.3.07 and table 3.3.04 of chapter 3, in the calibration process it was observed that the Ds cell measured more than the Dd cell.

	C_D at -30º		**C_D at +30º**	
Reynolds	**Sfr**	**Sd**	**Sfr**	**Sd**
100389,041	0,02038552	0,00389858	-0,14133979	-0,02702877
160298,63	0,64628358	0,12359691	0,52599804	0,10058796
218589,041	0,63785529	0,12198506	1,12274935	0,21470625
275260,274	0,71200327	0,13616531	1,36859225	0,26171942
336789,041	0,75503624	0,14439505	1,44034833	0,27544152
391841,096	0,80228054	0,15343017	1,39930544	0,26759278
448512,329	1,00718458	0,19261654	1,40533733	0,26874628
510041,096	0,98305047	0,18800107	0,96434371	0,18441393

Table 4.1.03. Drag coefficient at +/- 30º with the both methods of calculus of the areas.

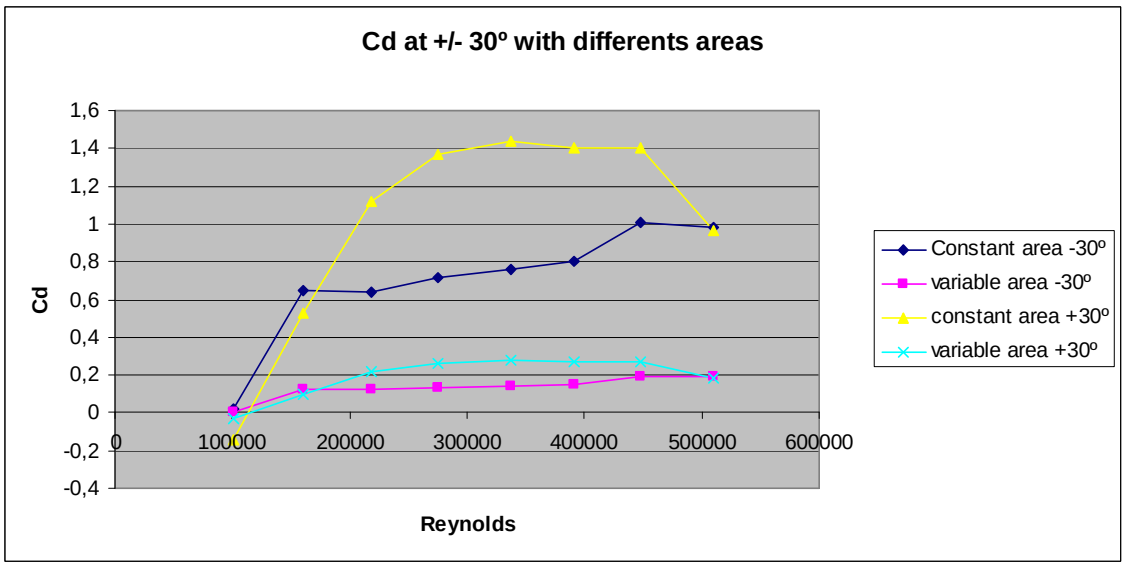

Fig. 4.1.06. Drag coefficient at +/- 30º with the both methods of calculus of the areas.

	C_D at -20º		C_D at +20º	
Reynolds	**Sfr**	**Sd**	**Sfr**	**Sd**
100389,041	0,31720895	0,08083191	-0,07718432	-0,01966829
160298,63	0,70628986	0,1799784	0,54741292	0,13949302
218589,041	0,85016666	0,21664141	0,8234159	0,20982472
275260,274	0,92551854	0,23584275	1,05465402	0,26874935
336789,041	0,96539384	0,24600387	1,21762788	0,31027873
391841,096	1,00431954	0,25592301	1,33502191	0,34019334
448512,329	1,02243813	0,26054003	1,60874542	0,40994419
510041,096	1,03590556	0,26397183	1,67646916	0,42720171

Table 4.1.04. Drag coefficient at +/- 20º with the both methods of calculus of the areas.

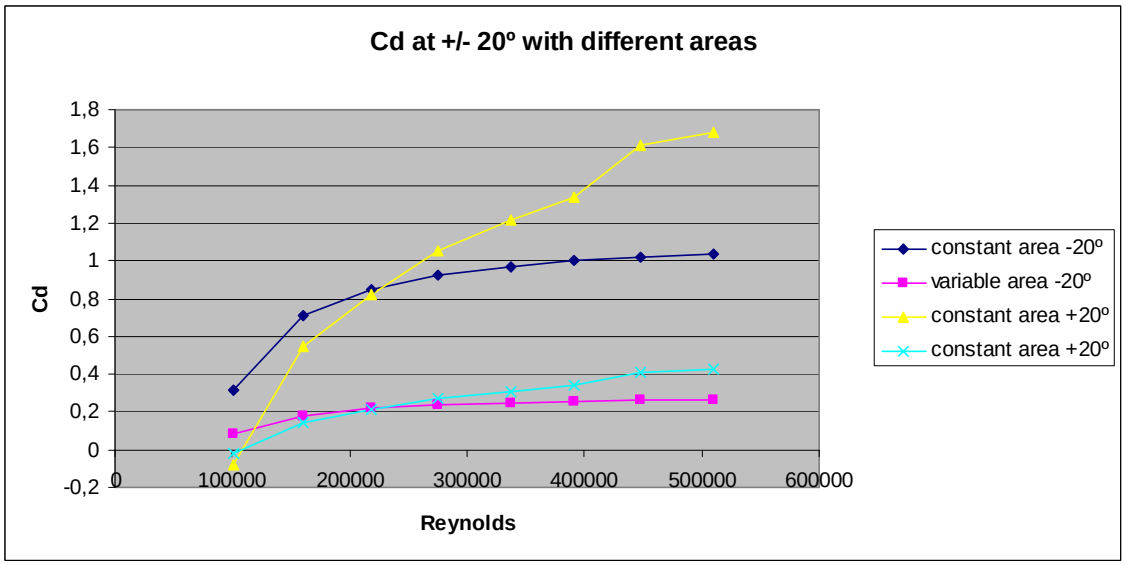

Fig. 4.1.07. Drag coefficient at +/- 20º with the both methods of calculus of the areas.

	C_D at -10º		C_D at +10º	
Reynolds	**Sfr**	**Sd**	**Sfr**	**Sd**
100389,041	-0,00148292	-0,00059314	0,05077422	0,0203086
160298,63	0,25960852	0,10383783	0,34438163	0,13774525
218589,041	0,55935059	0,22372821	0,76170357	0,30466505
275260,274	0,68615168	0,27444592	1,00145375	0,40055997
336789,041	0,82185372	0,32872382	1,12184662	0,44871453
391841,096	0,92304492	0,36919812	1,1821288	0,4728261
448512,329	0,96848937	0,38737492	1,21494918	0,48595355
510041,096	0,99469309	0,39785585	1,2569904	0,50276913

Table 4.1.05. Drag coefficient at +/- 10º with the both methods of calculus of the areas.

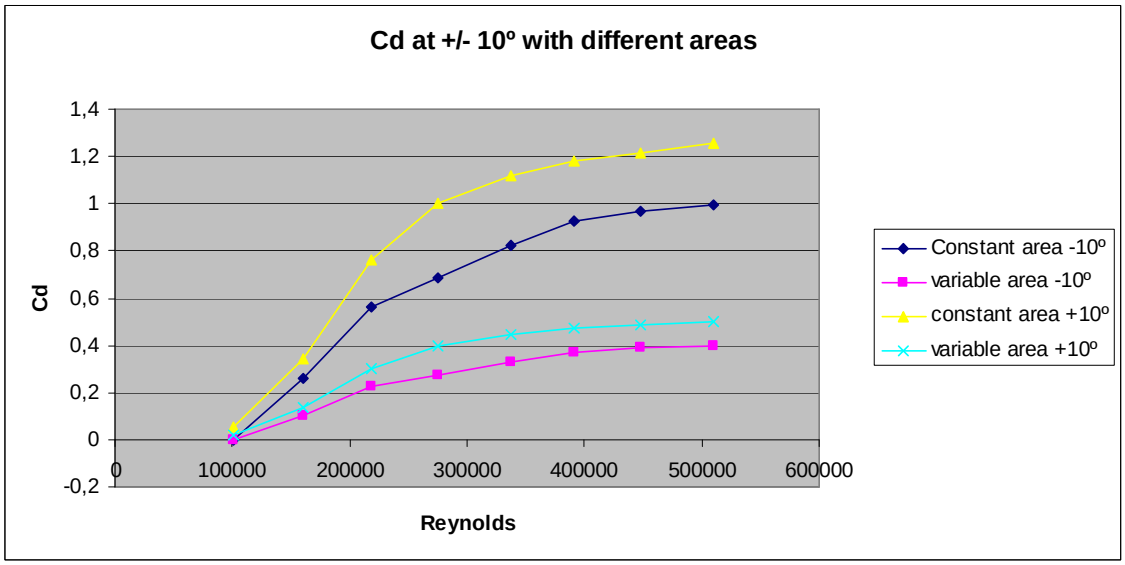

Fig. 4.1.08. Drag coefficient at +/- 10º with the both methods of calculus of the areas.

4.1.3 Lateral force

The lateral force coefficient will be calculated with the following formula:

$$C_Y = \frac{Y}{\frac{1}{2}\rho U^2 S_{lat}}$$

Fig 4.1.09 shows the behaviour of the lateral coefficient increasing the Reynolds number. The lateral coefficient should be symmetric to the zero axis, and in the figure it can be observed that this behaviour is not achieved so precisely. Nevertheless, it can be observed that the positive yawing angles lines are under the zero line, which slightly reflects this symmetry expected. As in the case of the drag coefficient, the difference between the

measures of the positive and negative yawing angles can be explained from the calibration experiments of chapter 3. Remembering the calibration experiments, in figs. 3.3.12 and 3.3.13 it can be observed that the cell Ys measures much less than it should measure. This explains why the lateral coefficients measured with positive angles are lower than negatives yawing angles as it can be observed in fig. 4.1.09.

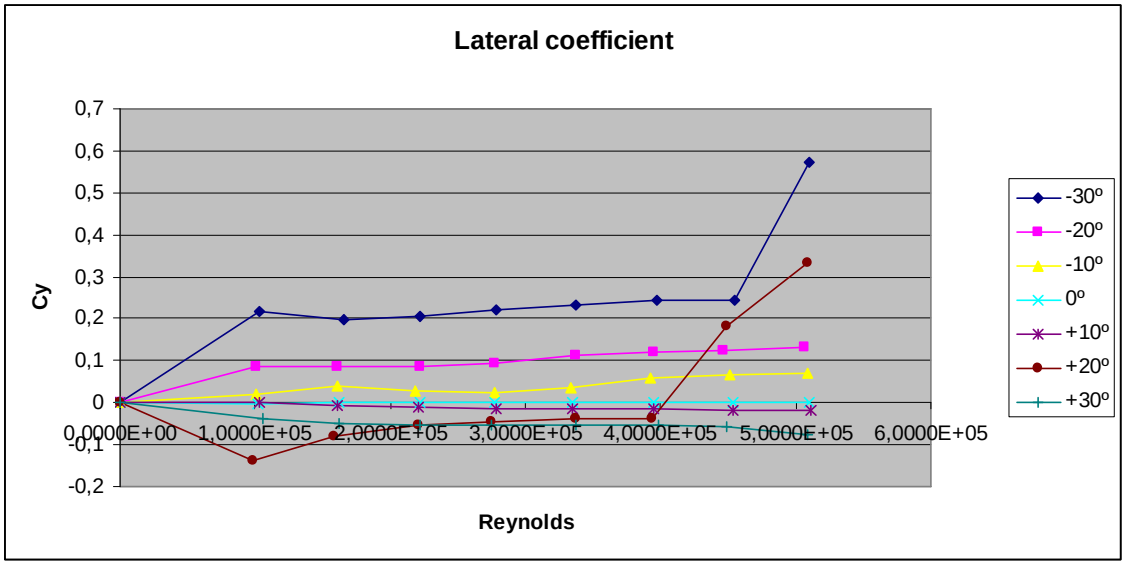

Fig. 4.1.09. Lateral coefficient at different yawing angles vs. Reynolds number.

Speed of wind (m/s)	Reynolds	Lateral force (N)	Ys (N)	Yd (N)	Cy
0	0,0000E+00	1,02E-03	-2,23E-03	-0,00121166	0
6,3	1,0201E+05	-0,00136832	-3,08E-03	-0,00445318	-0,00167375
10	1,6192E+05	1,21E-03	-5,43E-03	-4,22E-03	0,00058643
13,7	2,2183E+05	0,00338112	-8,45E-03	-0,00506691	0,00087459
17,1	2,7688E+05	3,78E-03	-0,0089351	-0,00515323	0,00062791
20,7	3,3517E+05	-0,00023025	-0,00842518	-0,00865542	-2,6088E-05
24,4	3,9508E+05	0,00259584	-0,00982871	-0,00723287	0,00021168
28	4,5337E+05	-0,000985	-0,00881829	-0,0098033	-6,0997E-05
31,5	5,1004E+05	-0,00215316	-0,0109301	-0,0130832	-0,00010535

Table 4.1.06. Lateral data at zero yaw angle.

As in the case of the drag coefficient, the lateral coefficient has been calculated by the same two different modes. In the first method the lateral area is supposed to be constant with value 0.033492 m^2 while in the second method the value of the lateral area is variable and it is calculated with the next formula:

$$S_Y = S_{fr} \cdot \sin\beta + S_{lat} \cdot \cos\beta \qquad (4.2)$$

where S_{fr} is 0.003838 m^2 and S_{lat} is 0.033492 m^2 and β the yawing angle of each experiment.

The data of the lateral coefficient calculated with the constant lateral area and with the area calculated with the formula (4.2) are shown in the figs. 4.1.10 to 4.1.12 and in tables 4.1.07 to 4.1.09.

As it has been explained before, the behaviour of the lateral coefficient should be symmetrical, then in the next tables and figures the analysis will be done for yawing angles of the same absolute value. As in the drag case, the behaviour of the lateral coefficient increasing the Reynolds number will be analyzed.

In this case the difference between the values of the areas is not as high as in the case of the drag coefficient, and this is the reason why the lateral coefficients calculated by both methods for each yawing angle are very similar. Moreover, in this case the area Sy calculated with the formula (4.2) for the lateral coefficient becomes lower, not as in the case of the area for the drag coefficient calculus. This is why the lateral coefficient calculated from the area varying with the yawing moment is bigger than supposing the area constant, it means the pink line in fig. 4.1.10 is over the blue line.

Also, a higher value of the lateral coefficient in the case of negative yawing angles than in positive angles can be observed. As it is explained before, this behaviour can be due to the differences in the measurements of the Ys cell and Yd cell explained in chapter 3.

	C_Y at -30		**C_Y at 30**	
Reynolds	**Slat**	**Sy**	**Slat**	**Sy**
100389,041	0,21843789	0,23657806	-0,03733454	-0,04043499
160298,63	0,19905811	0,21558888	-0,04955728	-0,05367276
218589,041	0,20593722	0,22303926	-0,0524558	-0,05681199
275260,274	0,22033488	0,23863258	-0,05229391	-0,05663666
336789,041	0,23452149	0,25399731	-0,05348513	-0,0579268
391841,096	0,24298637	0,26316517	-0,05320369	-0,05762198
448512,329	0,24457554	0,2648863	-0,05598091	-0,06062984
510041,096	0,57425039	0,62193898	-0,07591936	-0,08222408

Table 4.1.07. Lateral coefficient at +/- 30º with both methods of calculus of the areas.

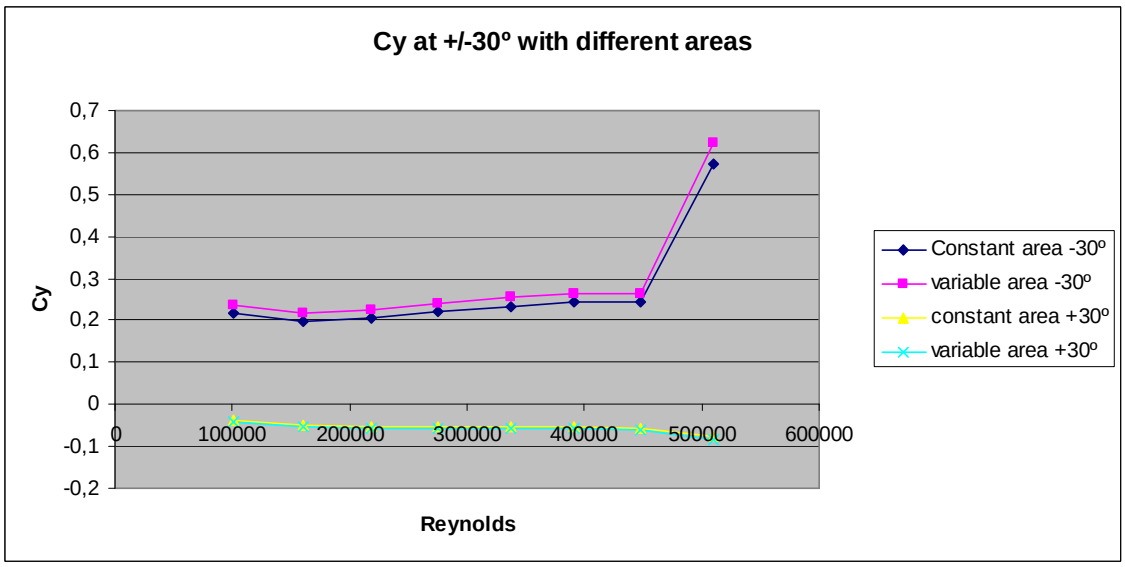

Fig. 4.1.10. Lateral coefficient at +/- 30º with both methods of calculus of the areas.

	C_Y at -20		C_Y at 20	
Reynolds	**Slat**	**Sy**	**Slat**	**Sy**
100389,041	0,08725819	0,08914027	-0,13647194	-0,13941552
160298,63	0,0847576	0,08658575	-0,08133034	-0,08308457
218589,041	0,08397966	0,08579103	-0,05363926	-0,05479621
275260,274	0,09496727	0,09701563	-0,04575301	-0,04673987
336789,041	0,11112025	0,11351702	-0,03960113	-0,04045529
391841,096	0,11886756	0,12143143	-0,0365928	-0,03738208
448512,329	0,12291774	0,12556897	0,18335623	0,18731106
510041,096	0,13250646	0,13536451	0,33313276	0,34031814

Table 4.1.08. Lateral coefficient at +/- 20º with both methods of calculus of the areas.

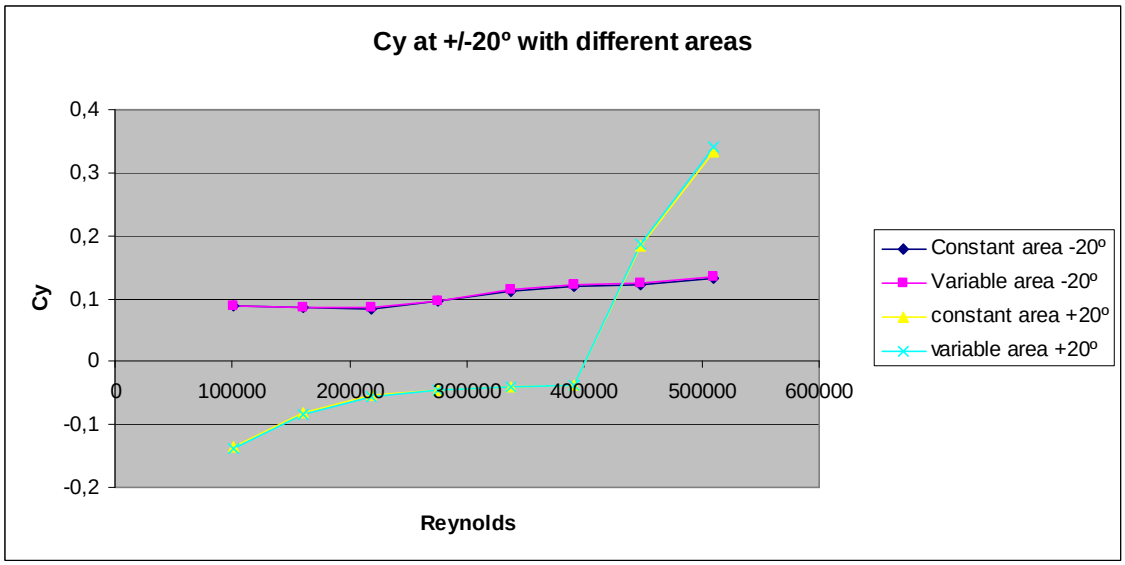

Fig. 4.1.11. Lateral coefficient at +/- 20º with both methods of calculus of the areas.

	C_Y at -10		C_Y at 10	
Reynolds	**Slat**	**Sy**	**Slat**	**Sy**
100389,041	0,01931101	0,01922054	0,00113173	0,00112643
160298,63	0,03846196	0,03828177	-0,00499582	-0,00497241
218589,041	0,02624669	0,02612373	-0,01006423	-0,01001709
275260,274	0,02430608	0,02419221	-0,01312821	-0,01306671
336789,041	0,03690456	0,03673167	-0,01521189	-0,01514063
391841,096	0,05747429	0,05720504	-0,01637653	-0,01629981
448512,329	0,06788595	0,06756791	-0,01725832	-0,01717747
510041,096	0,07156303	0,07122777	-0,01716693	-0,0170865

Table 4.1.09. Lateral coefficient at +/- 10º with both methods of calculus of the areas.

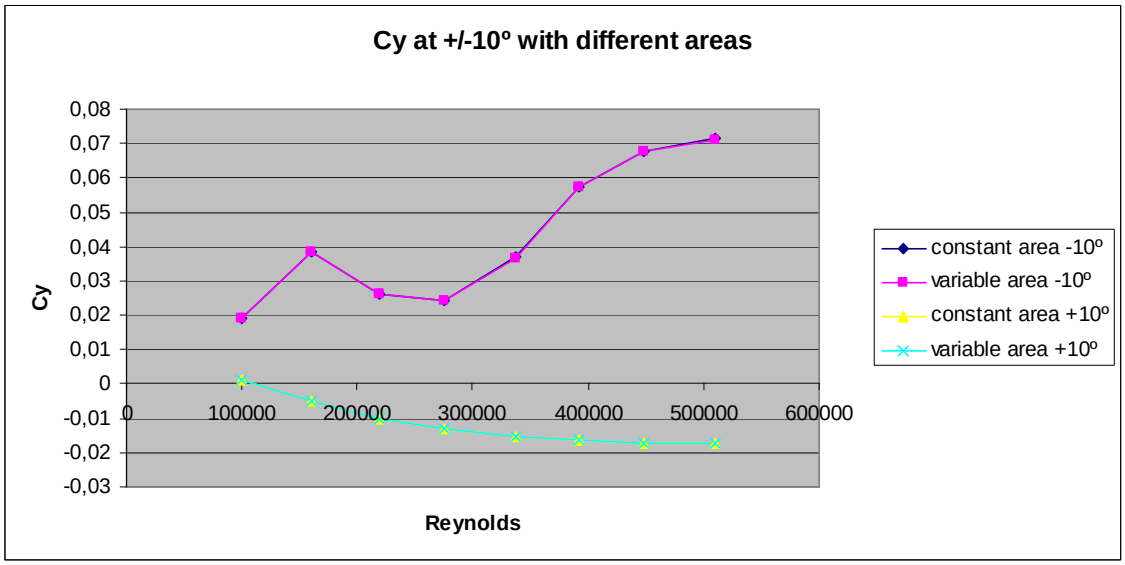

Fig. 4.1.12. Lateral coefficient at +/- 10º with both methods of calculus of the areas.

4.1.4 Pitching moment

The pitching moment is a very important characteristic of the motorcycles that should be analyzed because a big pitching moment can provoke unloading of the front wheel. The pitching moment coefficient will be calculated with the following formula:

$$C_{mPitching} = \frac{M_{pitching}}{\frac{1}{2}\rho U^2 S_{pl} l}$$

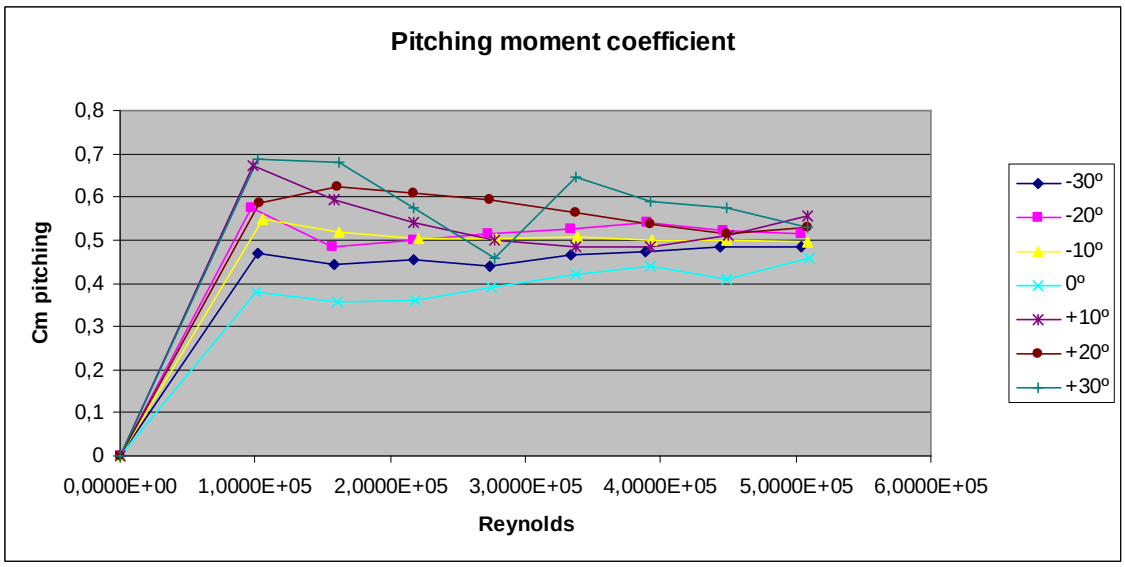

Fig. 4.1.13. Pitching moment coefficient at different yawing angles *vs*. Reynolds number.

As in the case of the lift coefficient, the pitching moment coefficient should be symmetric, that means, the coefficients of the positive and negative angles with the same absolute value should be similar. As in the other cases this does not happen so precisely in this experiment. As shows fig. 4.1.13 the tendency of the pitching moment coefficient with the Reynolds number is regular but not strictly symmetric. In the figure, it can be observed that the coefficient measured increases with the yawing angle and at the zero angle, the coefficient has the lowest value measured, achieving a value of 0.45.

Table 4.1.10 shows the pitching moment data at the zero angle case.

Speed of wind (m/s)	Reynolds	Pitching moment (mN)	Fs (N)	Fd (N)	As (N)	Ad (N)	Cm pitch
0	0,0000E+00	-9,37E-04	-0,00290664	0,0136531	7,25E-04	-0,00336586	0
6,2	1,0039E+05	0,00789096	-0,0398371	-0,0322445	0,0289202	0,0117263	0,38080234
9,9	1,6030E+05	0,018881	-0,0930027	-0,0567738	0,0797968	0,0401557	0,35736149
13,5	2,1859E+05	0,0355786	-0,166951	-0,101205	0,147462	0,0926482	0,3621383
17	2,7526E+05	6,09E-02	-0,249197	-0,206948	0,233818	0,180052	0,39091329
20,8	3,3679E+05	0,0980953	-0,402358	-0,331814	0,32914	0,338049	0,42060524
24,2	3,9184E+05	0,138437	-0,564775	-0,509231	0,388704	0,514964	0,43850504
27,7	4,4851E+05	0,168822	-0,495427	-0,697848	0,349545	0,868928	0,40815268
31,5	5,1004E+05	0,244285	-0,351612	-1,53989	0,26473	1,33356	0,45669771

Table 4.1.10. Pitching moment data at zero angle.

4.1.5 Yawing moment

The yawing moment coefficient is calculated from the formula:

$$C_{mYawing} = \frac{M_{yawing}}{\frac{1}{2}\rho U^2 S_{fr} b}$$

Fig. 4.1.14 shows the behaviour of the yawing moment coefficient increasing the Reynolds number. As in the case of the lateral coefficient, the yawing moment coefficients should be symmetric to the zero axis. In this figure, this behaviour can be observed, but as in other cases, it is not so strictly. Also, as in the case of the drag coefficient a lower coefficient values in the negative yawing angles can be explained due to the difference between the measures of the Ds and Dd cells. It can be observed in the figure that the yawing moment coefficient increases with the Reynolds number. This is because the area front to the wind direction increases with the yawing angle and this implies an increase of the moment arm too, increasing the final product, which is the yawing moment.

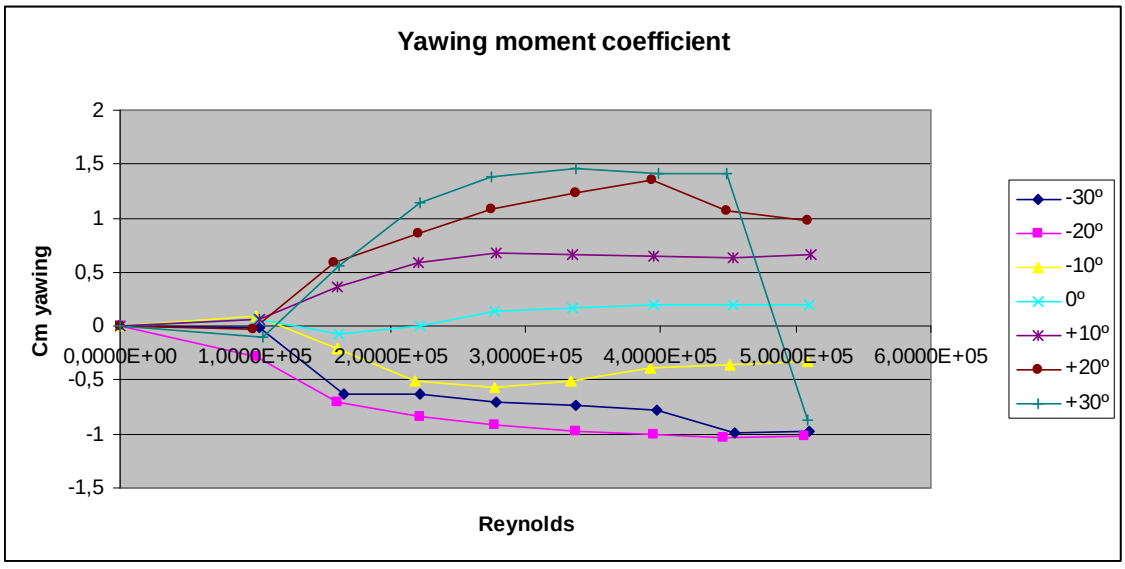

Fig. 4.1.14. Yawing moment coefficient at different yawing angles vs. Reynolds number.

Fig 4.1.14 shows that at zero angle the yawing moment is not null while it should be. This can indicate that the motorcycle model has moved from the zero angle to the direction

of the negatives yawing angles. It can also explain that the yawing moment coefficients measured at negative angles are higher than at positive angles.

Table 4.1.11 shows the yawing moment data at the zero angle case.

Speed of wind (m/s)	Reynolds	Yawing moment (mN)	Ds (N)	Dd (N)	Cm yaw
0	0,0000E+00	4,31E-04	-2,35E-03	-0,00781539	0
6,3	1,0201E+05	4,63E-04	-5,57E-03	-1,15E-02	0,06286273
10	1,6192E+05	-1,27E-03	-0,00608986	0,0100991	-0,06863008
13,7	2,2183E+05	5,83E-05	0,0973873	0,0966469	0,00167226
17,1	2,7688E+05	7,50E-03	0,293876	0,19858	0,13815961
20,7	3,3517E+05	1,30E-02	0,530312	0,365717	0,16284327
24,4	3,9508E+05	2,12E-02	0,814479	0,54556	0,1914865
28	4,5337E+05	0,0285224	1,11904	0,756848	0,19584622
31,5	5,1004E+05	3,63E-02	1,47026	1,00884	0,19713656

Table 4.1.11. Yawing moment data at zero angle.

4.1.6 Rolling moment

Rolling moment coefficient is calculated from the formula:

$$C_{mRolling} = \frac{M_{rolling}}{\frac{1}{2}\rho U^2 S_{lat} b}$$

As in the case of the yawing moment coefficient, the rolling moment coefficient should be symmetrical to the zero axis. Fig 4.1.15 shows this behaviour increasing the Reynolds number. This is the best example of the symmetry in all the experiments analyzed. It can be observed that the behaviour in the positive angles is very similar to the negative yawing angles. Also, it can be noticed that in the case of zero angle the rolling moment is very close to zero.

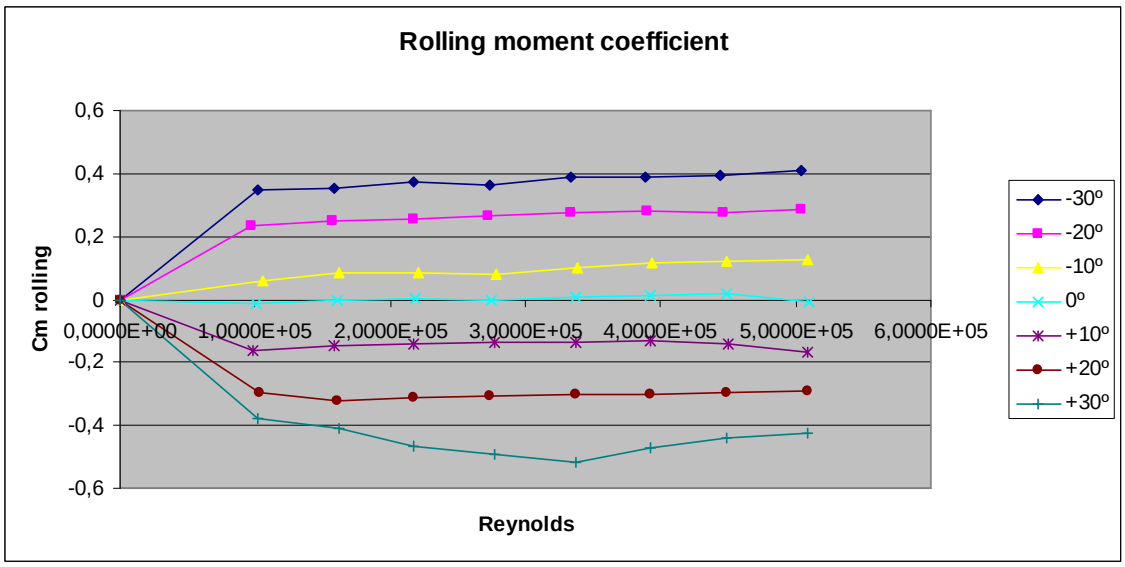

Fig. 4.1.15. Rolling moment coefficient at different yawing angles vs. Reynolds number.

Speed of wind (m/s)	Reynolds	Rolling moment (mN)	Fs (N)	Fd (N)	As (N)	Ad (N)	Cm roll
0	0,0000E+00	9,82E-04	-0,00290664	0,0136531	7,25E-04	-0,00336586	0
6,2	1,0039E+05	-0,0007561	-0,0398371	-0,0322445	0,0289202	0,0117263	-0,01213398
9,9	1,6030E+05	-0,00026871	-0,0930027	-0,0567738	0,0797968	0,0401557	-0,00169129
13,5	2,1859E+05	0,00086091	-0,166951	-0,101205	0,147462	0,0926482	0,00291407
17	2,7526E+05	-0,00090697	-0,249197	-0,206948	0,233818	0,180052	-0,00193598
20,8	3,3679E+05	0,00625697	-0,402358	-0,331814	0,32914	0,338049	0,00892168
24,2	3,9184E+05	0,014317	-0,564775	-0,509231	0,388704	0,514964	0,01508101
27,7	4,4851E+05	0,0249607	-0,495427	-0,697848	0,349545	0,868928	0,0200681
31,5	5,1004E+05	-0,00940666	-0,351612	-1,53989	0,26473	1,33356	-0,00584822

Table 4.1.12. Rolling moment data at zero angle.

4.2 FORCE AND FORCE COEFFICIENT MEASURED AT ZERO ANGLE WITH MOVING BELT

As it is explained in chapter 2, only one measure with the moving belt system has been obtained. This measurement has been performed at zero angle and achieving a belt speed of 10 m/s. At higher speeds the motor was overheated and the belt was derailed and blocked.

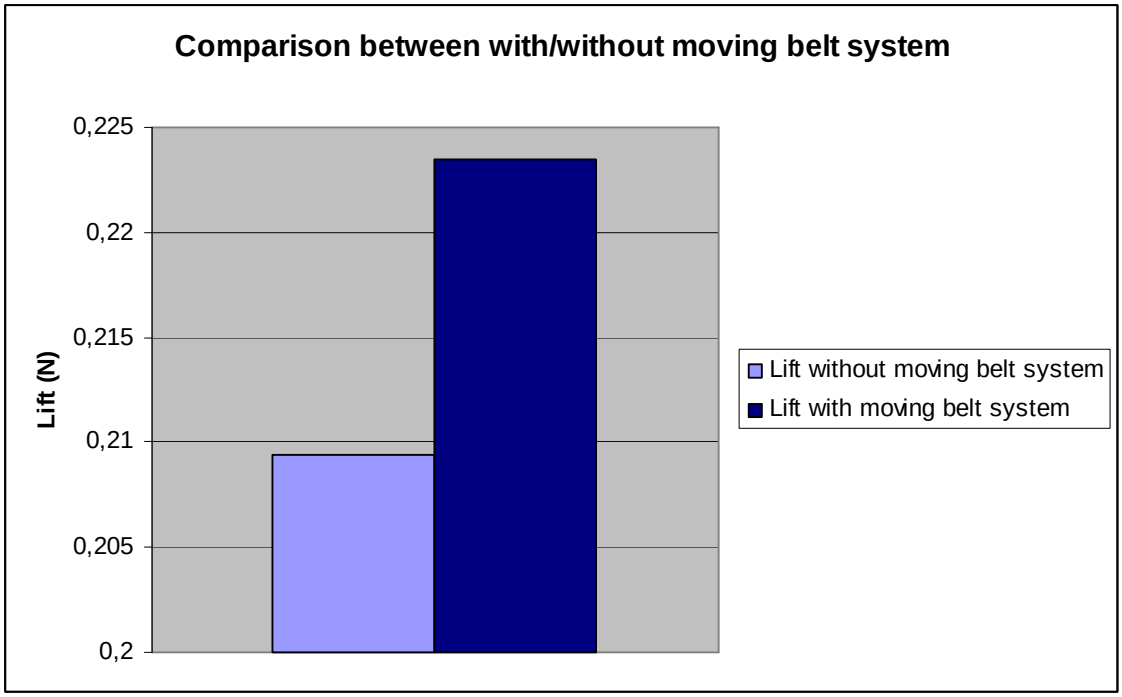

Fig. 4.2.01. Lift comparative with and without moving belt system.

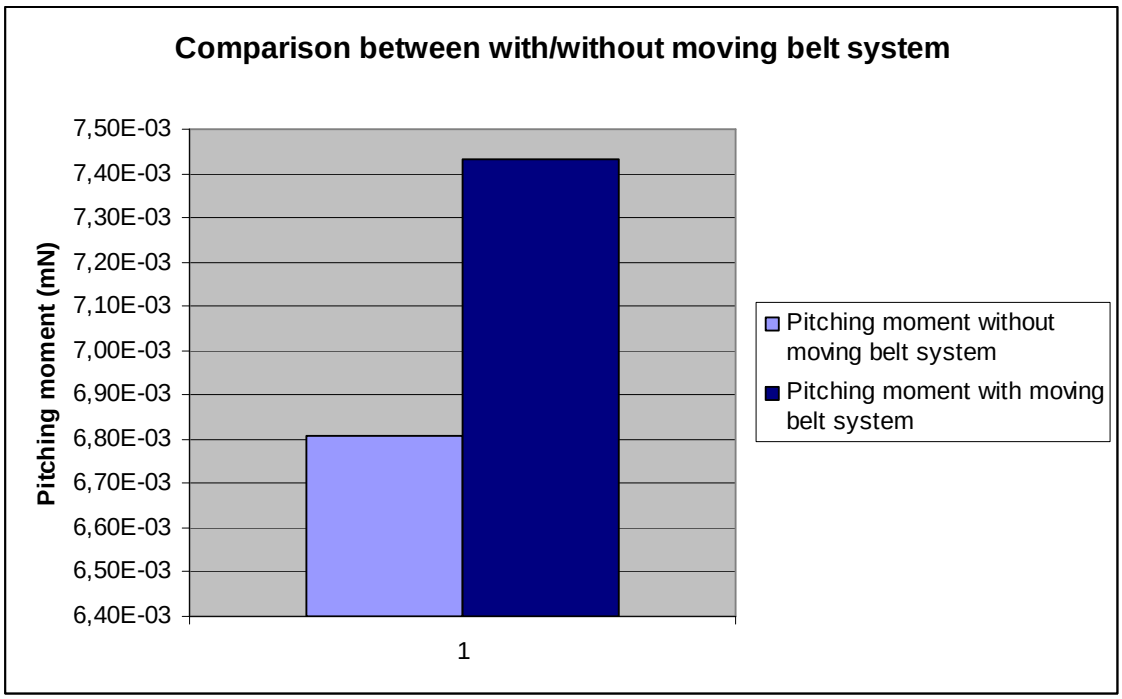

Fig. 4.2.02. Pitching moment comparative with and without moving belt system.

Figs. 4.2.01 and 4.2.02 show the comparison of the lift forces (in newtons) and the pitching moments measured in the wind tunnel with and without the moving belt system.

In fig. 4.2.01 it can be observed that the lift force increases with the moving belt system. Notice that in the Labview program, the lift is defined as positive in the direction of the gravity, that means, if the lift force increases, it will be more adherence.

This is why lift force should be higher and positive with the moving belt system, because this system provokes the elimination of the boundary layer and increases the adherence to the floor. This tendency is shown in fig. 4.2.01. But notice that in this experiment, the lift measured without the moving belt system is positive while the lift measured in the other experiment of the table 4.1.01 at the same speed of wind was negative, so the behaviour of this moving belt system is not ensured with this experiment.

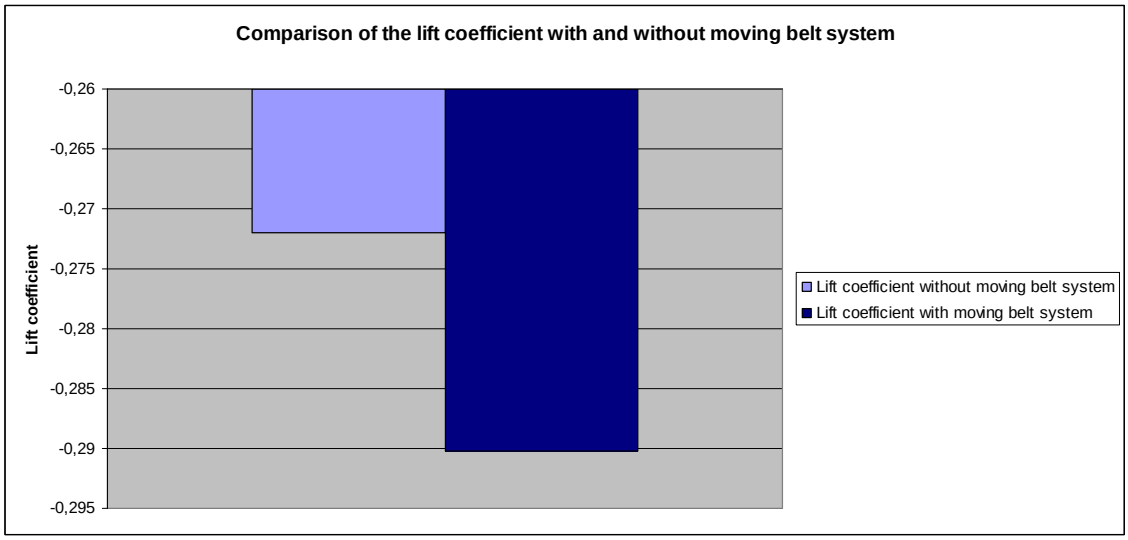

Fig. 4.2.03. Lift force coefficient comparative with and without moving belt system.

Figs. 4.2.03 and 4.2.04 show the coefficients of the lift force and the pitching moment.

In fig. 4.2.03 it can be observed that the lift force coefficient decreases with the usage of the moving belt system as it was expected.

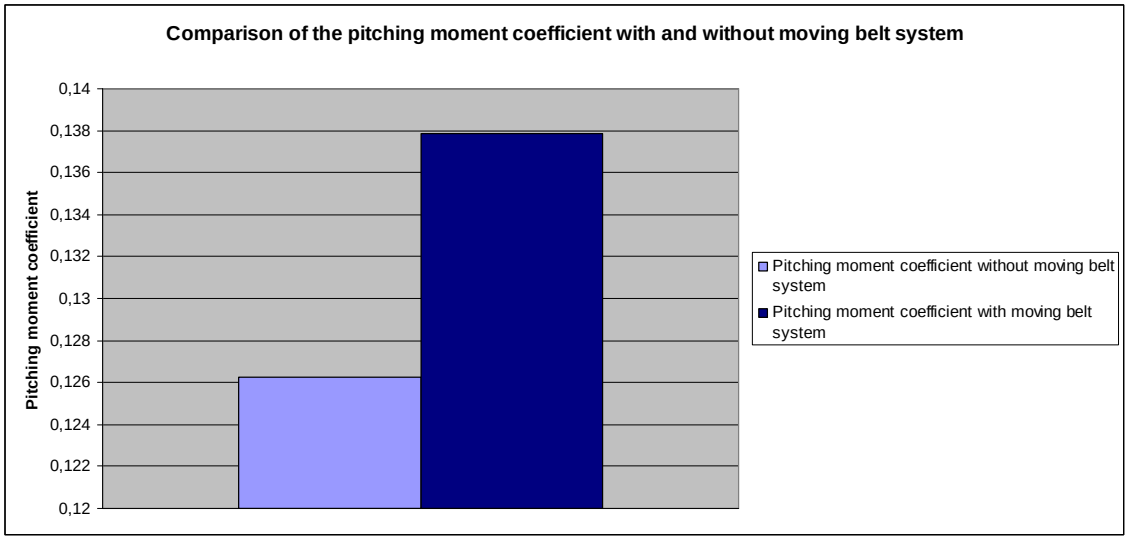

Fig. 4.2.04. Pitching moment coefficient comparative with and without moving belt system.

CONCLUSIONS

The final conclusions derived from this thesis are summarized in two blocks, one corresponding to the conclusions derived from the calibration process of the dynamometric balance and another one that collects the results obtained from the experiments developed in the wind tunnel.

The final conclusions derived from the calibration experiments are detailed in the following lines:

- The pre-charge on the drag and lateral cells provokes a bad effect on the measurements performance.
- To solve the problem of friction between the moving plate and the bottom of the balance, the decision adopted is the usage of four small spheres under the moving plate.
- The Ds cell measures more than the Dd cell. This provokes the absence of the expected symmetry of the yawing moment measured on the wind tunnel.
- The Ys cell of the dynamometric balance is broken. The solution has been to interchange it with the Fs cell in the experiments with the spheres. Thus, calibrating the Ys cell, it has been observed that measures much less than the theoretical value expected. This provokes, as in the drag cells case, the absence of the symmetry expected in the lateral coefficient.

From the wind tunnel experiments the conclusions extracted are the following:

- It has been proved that the fixation affects to the measurements of the drag coefficient because it increases the front area. The drag coefficient is expected to be lower, and its high value is due to the actual fixation used in the experiments. Therefore, a new specific fixation for motorcycle models should be designed to obtain more reliable results. In fact, this new fixation must avoid the movement of the motorcycle model during the experiments even with high speeds of wind, which was not true in the case of the actual fixation used in the experiments.
- The evolution of the results of the experiments on the wind tunnel is as expected theoretically.
  - Drag increases with the square of the speed of wind.
  - All the dimensionless coefficients increase with the yawing angle.
- The moving belt system does not work as expected. The motor was overheated and the belt was derailed when the speed increased. Thus the motor should have been dimensioned with a higher power. Only one experiment with the moving belt system was performed and its behaviour did not fit the theoretical results.

REFERENCE LIST

[1] *Advances in Wind Tunnel Aerodynamics for Motorsport Testing.* http://www.sae.org/technical/papers

[2] www.a2wt.com

[3] www.kasravi.com

[4] http://lswt.tamu.edu/facilities.htm

[5] www.pininfarina.it

[6] *Update on progress in adaptive wind tunnel wall technology.* O.Meyer*, W.Nitsche. Technical University of Berlin, Institute of Aero- and Astronautics, Marchstr. 12, 10587 Berlin, Germany www.sciencedirect.com

[7] *Contoured wall upgrade. The Honda wind tunnel.* http://www3.imperial.ac.uk/pls/portallive/docs/1/5039977.PDF

[8] http://www.mhi.co.jp/technology/review/pdf/e433/e433063.pdf

[9] http://www.sportrider.com/tech/146_0106_aero/index.html

[10] http://iar-ira.nrc-cnrc.gc.ca/aero/aero_6b_e.html

[11] *Motorcycle dynamics*. Second edition, Vittorio Cossalter. http://books.google.com/books?id=rJTQxITnkbgC&printsec=frontcover&dq=motorcycle+dynamics+vittore+cossalter&hl=es#PPP1,M1

[12] http://www.cortana.com/20061218_Boundary_Layer_of_Flat_Plate_jpg.jpg

[13] www.cycleconnections.com

[14] *Confronto tra le forze agenti su due modelli di vetture da corsa in galleria del vento.* Paolo Cantini, Corso di laurea in Ingegneria Aerospaziale, Università di Roma "La Sapienza", 2007

[15] *Studio sperimentale su un motoveicolo in galleria del vento.* Stefania Zicoschi. Corso di laurea in Ingegneria Meccanica, Università di Roma "La Sapienza", 2007

[16] *Motorcycle handling and chassis design*. Tony Foale.
http://books.google.com/books?id=84hF-qoR5I8C&printsec=frontcover&dq=motorcycle+handling+and+chasis+design+tony+foale&hl=es#PPT129,M1

[17] *Indagine sperimentale sulle forze aerodinamiche agenti su un modello di autovettura tipo Formula 1.* Vittorio Muzzioli, Corso di laurea in Ingegneria Aerospaziale, Università di Roma "La Sapienza", 2007

[18] *Analisi sperimentale dell'aerodinamica di differenti categorie di vetture da competizione*, Marco Nunez, Tesi di laurea in aerodinamica sperimentale, università di Roma "La Sapienza", 2004-05.

[19] *Montaje, ajuste y verificación de elementos de máquinas de isofix*. Reverte editorial. Joseph Schröck, Schrok J. Development,
http://books.google.com/books?id=_8vMspBD9fUC&pg=PA101&lpg=PA101&dq=coeficiente+rozamiento+rodadura+y+deslizamiento+comparacion&source=bl&ots=HOiSquv4yv&sig=YoBVGxLABB0_1bsmQBTC2_GR23M&hl=es&ei=FeQrSrqdM4mH_Qbnm8XqCg&sa=X&oi=book_result&ct=result&resnum=3#PPA101,M1

[20] http://outyourbackdoor.com/article.php?id=623

[21] http://www.motociclismo.es/Deporte/presentacion-yamaha-yzr-m1-fiat-yamaha-ficha-tecnica-valentino-rossi-kw-noticia.jsp%3Fid%3D6594

ACKNOWLEDGEMENTS

Thanks to my family and friends for their support and help during the development of this thesis.

Thanks to my tutors Giovanni Paolo Romano and Antonio Lecuona for his patience and to Domenico Pietrogiacomi for his help during the laboratory exercises. It was a pleasure to work with you.

Also thanks to the University La Sapienza for the welcome during this Erasmus Interchange.